Better, Faster, Stronger: Measuring and Transcending Your Physical Limits with Wearable Robots

Robert Matthew
Ruzena Bajcsy, Ed.
Masayoshi Tomizuka, Ed.
Robert Full, Ed.

Electrical Engineering and Computer Sciences
University of California at Berkeley

Technical Report No. UCB/EECS-2018-143
http://www2.eecs.berkeley.edu/Pubs/TechRpts/2018/EECS-2018-143.html

December 1, 2018

Copyright © 2018, by the author(s).
All rights reserved.

Permission to make digital or hard copies of all or part of this work for personal or classroom use is granted without fee provided that copies are not made or distributed for profit or commercial advantage and that copies bear this notice and the full citation on the first page. To copy otherwise, to republish, to post on servers or to redistribute to lists, requires prior specific permission.

Better, Faster, Stronger: Measuring and Transcending Your Physical Limits with Wearable Robots

by

Robert Peter Matthew

A dissertation submitted in partial satisfaction of the

requirements for the degree of

Doctor of Philosophy

in

Electrical Engineering and Computer Science

in the

Graduate Division

of the

University of California, Berkeley

Committee in charge:

Professor Ruzena Bajcsy, Chair
Professor Masayoshi Tomizuka
Professor Robert Full

Fall 2016

Better, Faster, Stronger: Measuring and Transcending Your Physical Limits with Wearable Robots

Copyright 2016
by
Robert Peter Matthew

Abstract

Better, Faster, Stronger: Measuring and Transcending Your Physical Limits with Wearable Robots

by

Robert Peter Matthew

Doctor of Philosophy in Electrical Engineering and Computer Science

University of California, Berkeley

Professor Ruzena Bajcsy, Chair

Measure what is measurable. Make what is not measurable so.
-Galileo Galilei

This thesis introduces a kinematic and dynamic framework for creating a representative model of an individual. Building on results from geometric robotics, a method for formulating a geometric *dynamic identification model* is derived. This method is validated on a robotic arm, and tested on healthy subjects to determine the utility as a clinical tool.

The proposed framework was used to *augment* the five-times sit-to-stand test. This is a clinical test designed to estimate an individual's stability by timing the total time to stand/sit five times. Using the proposed framework, a representative kinematic and dynamic model was obtained which outperformed conventional height/mass scaled models. This allows for rapid, quantitative measurements of an individual, with minimal retraining required for clinicians.

These tools are then used to develop a *prescriptive* model for developing assistive devices. The recovered models can be used to formulate an optimisation to determine the actuator types and parameters to provide augmentation.

This framework is then used to develop a novel system for human assistance. A prototype device is developed and tested. The prototype is lightweight, uses minimal energy, and can provide an augmentation of 82% for providing hammer curl assistance. The modelling framework is used to analyse the effect this assistance has on compensatory actions of the shoulder.

My parents, family, and teachers for supporting me.

Elizabeth Barley, Patrick Ciccone, Joel Loeza, Waiman Meinhold, and Eric Mica for keeping your heads through the chaos of undergrad and inspiring and executing some outstanding research. I wouldn't have been able to do the majority of this work without your help, support, and camaraderie.

Katherine Driggs-Campbell, Jessica Gamble, and Sarah Seko, for your kind words and keeping an eye on me over these years.

Kena Joy Hazlewood-Carter, Aimée Tabor, and Paige Teemy for teaching me how to be a better educator and facilitator of safe spaces.

The espresso machine in 337 Cory. I think I will miss you most of all.

Acknowledgments

This work was supported by the assistance and contributions of Elizabeth Barley, Patrick Ciccone, Gregorij Kurillo, Joel Loeza, Waiman Meinhold, Eric Mica, Sarah Seko, Victor Shia, and Gentaine Venture.

This project was funded through JSPS grant K125870209 and NSF grants 1354321, 1362172, and 1427260.

Contents

Contents iii

List of Figures v

List of Tables xi

1 Introduction 1
1.1 Motivation . . . 1
1.2 Contributions . . . 4

2 Mathematical Preliminaries 7
2.1 Rotations and Rigid-Body Motion . . . 7
2.2 Geometric Robotics- Introduction . . . 11
2.3 Geometric Robotics- Kinematics . . . 17
2.4 Geometric Robotics- Dynamics . . . 21

I Human Modelling 23

3 Kinematic Modelling 25
3.1 State of the Art . . . 25
3.2 Kinematic Recovery Framework . . . 31

4 Dynamic Modelling 39
4.1 State of the Art . . . 39
4.2 Dynamic Recovery Framework . . . 46

5 Robotic Validation 49
5.1 UR5 Robot . . . 49
5.2 Method . . . 49
5.3 Kinematic Recovery . . . 51
5.4 Dynamic Recovery . . . 55
5.5 Guidelines for Dynamic Modelling . . . 62

5.6 Conclusion 66

6 Clinical Applications **69**
6.1 Sit-to-Stand 69
6.2 Method 70
6.3 Kinematic Recovery 71
6.4 Dynamic Recovery 77
6.5 Conclusion 84

II Prescriptive Assistive Devices **87**

7 Prescriptive Robotics **89**
7.1 Motivation 89
7.2 Metrics 90
7.3 Prescriptive Robotics 97
7.4 Passive Shoulder Orthosis 98

8 Active Passive Exoskeleton **107**
8.1 APEX 107
8.2 Design 109
8.3 Initial Trials 109
8.4 Conclusion 118

9 Future Work **119**
9.1 Modelling Framework 119
9.2 Robotic Validation 120
9.3 Human Modelling 120
9.4 Prescriptive Robotics 121
9.5 APEX 121
9.6 High-level APEX control 122

Bibliography **125**

List of Figures

1.1 Existing commercial exoskeletons. From left to right: HAL-5 lower limb, Re-walk, eLegs, and Indego. 2

2.1 Two coordinate frames A and B with a common origin $\boldsymbol{p}$. Frame B is attached to the rigid body. The rotation about the point $\boldsymbol{p}$ is parametrised by the angle θ_1. The point $\boldsymbol{q}$ is attached rigidly to the rigid body. 8

2.2 Two coordinate frames A and B. Frame B is attached to the rigid body. $\boldsymbol{p}_{A,B}$ are the coordinates of the origin of the B frame as viewed in the A coordinate frame. The rotation about the point $\boldsymbol{p}$ is parametrised by the angle θ_1. The point $\boldsymbol{q}$ is attached rigidly to the rigid body. 9

2.3 The segments of a serial chain structure. The world and tool frames are shown as W and T respectively. The frames of intermediary joints are shown, with the origin of the frame at the centre of the joint. 17

3.1 Overview of the Kinematic recovery framework. Left: Flowchart of algorithm. Right: Corresponding cartoons of steps in the algorithm. I. Markers remapped to the $i-1$ frame, II. Markers moving along circular paths, III. Markers moving about a common centre $\boldsymbol{p}_{i-1,i}$ with local coordinates $(\boldsymbol{\phi}, \boldsymbol{r})$, IV. Inverse Kinematics to recover joint state $\boldsymbol{\theta}, \dot{\boldsymbol{\theta}}, \ddot{\boldsymbol{\theta}}, \dddot{\boldsymbol{\theta}}$. 37

4.1 Cartoons showing the Ayusawa method for a single pendulum system. Left: Dynamic system for a single pendulum. The joint location is denoted $\boldsymbol{p}_1$, with the angle of rotation parametrised by θ_1. The frame of the fixed link and moving link are labelled as frames one and two respectively. The dynamic parameters for each link are contained in the parameter vectors $\boldsymbol{\psi}_1$ and $\boldsymbol{\psi}_2$. Right: Cartoon of the point mass grid for the physically consistent recovery. A grid of points of unknown mass distribution $\boldsymbol{\rho}_1$ and $\boldsymbol{\rho}_2$ are used to represent the true dynamic parameters. 43

5.1 Cartoon of the UR5 robot. The four segments of the robot that were excited are shown in different colours. The joint centres are marked with dotted lines. The location of motion capture markers on the UR5 robot are shown as red crosses. 50

5.2 Plots showing the kinematic recovery process for the slow rotation of the shoulder joint. I. Separation into moving, and stationary markers (black circles and blue crosses respectively). II. Circle fitting. Individual marker traces (colour arcs), and corresponding circle centres (green crosses). III. Parameter identification. Local marker coordinates (annotations), and centre of rigid body (green circle) shown. IV. Kinematic recovery. Recovered angular position, velocity, and acceleration data. Units are in radians. Blue trajectory is recovered via the proposed fourth order UKF. The red trajectory is the result of differentiating and filtering the recovered position trajectory. [67]. 53
5.3 Plots showing the kinematic recovery process for the fast rotation of the elbow joint. I. Separation into moving, and stationary markers (black circles and blue crosses respectively). II. Circle fitting. Individual marker traces (colour arcs), and corresponding circle centres (green crosses). III. Parameter identification. Local marker coordinates (annotations), and centre of rigid body (green circle) shown. IV. Kinematic recovery. Recovered angular position, velocity, and acceleration data. Units are in radians. Blue trajectory is recovered via the proposed fourth order UKF. The red trajectory is the result of differentiating and filtering the recovered position trajectory. [67]. 54
5.4 Graphs comparing the measured and recovered wrenches for fast elbow motions. All fifteen repetitions were time aligned and the mean and standard deviations found. The mean is plotted as a line, with the standard deviation as a shaded region about this line. The measured wrench is shown in black, and the recovered wrench using the Kufieta model shown in red. The wrench recovered using the robot measurements of position and velocity are shown as green circles. The wrench recovered using motion capture is shown in blue. 59
5.5 Graphs comparing the errors in the measured and recovered wrenches for fast elbow motions. All fifteen repetitions were time aligned and the mean and standard deviations found. The mean is plotted as a line, with the standard deviation as a shaded region about this line. The measured wrench is shown in black, and the recovered wrench using the Kufieta model shown in red. The wrench recovered using the robot measurements of position and velocity are shown as green circles. The wrench recovered using motion capture is shown in blue. 60
5.6 Graph comparing the estimated angular acceleration for a single trial of a fast rotation about the elbow joint. The UKF estimate from the observed angular position and velocity is shown as a solid blue line. The estimate recovered by filtering, differentiating, and filtering the measured angular velocity is shown as a dotted red line. 62

6.1 Subject in the seated and standing phases. Subject is wearing a motion capture suit with active markers placed on limb segments. Force platform is visible underneath the subject. Adjustable stool is shown. Mattresses are placed around the subject in case of falls. 70

6.2 Results of the kinematic recovery process. Left: Recovered kinematic skeleton as seen in the sagittal plane. Blue true marker locations at a particular frame. Red filled circles model joint centres. Red empty circles estimated marker locations based on recovered kinematic model and states. Right: Recovered joint state trajectories. Ankle, knee, and hip joints are shown in blue, red, and yellow respectively. 72
6.3 Stages in the kinematic recovery process for the sit-to-stand actions for a representative subject. Rows: Top to bottom: recovery of the second, third, and fourth kinematic segments. Columns: Recovery stages. Left: Motion capture markers remapped to local coordinate frame. Markers with valid circle centres shown as green crosses. Centre: Segment kinematic parametrisation. Localised markers are shown along with recovered joint centre. Right: Recovered state trajectories. Units are rad, rad/s, and rad/s^2. 73
6.4 Cartoon of the active motion capture marker locations. Three markers are located on the top, left and right sides of the head. A single marker is located at the top of the left shoulder, with two markers on the upper and lower arms. Three markers are locates on the back of each hand. Four markers are placed on the clavicle, solar-plexus, and at the base of the ribcage. A marker are placed on either side of the hi pat the anterior superior iliac spine. Two markers are placed on the thigh and shank. A single marker is placed on the lateral malleous. Two markers are then placed on the foot near the proximal phalanges of the little and big toe. 74
6.5 Comparison of proposed kinematic recovery framework (blue), and commercial motion capture system (red). Five sit to stand actions are averaged, with the mean shown as the solid line, and the standard deviation shown as the shaded region. Left: Skeleton showing joint positions and limb segments. Arc shows the variation in joint angle for that phase of the sit-to-stand. Right: State Trajectories for joint angles 75
6.6 Labelling convention for the DIM recovery process. Coordinate frames are defined by the kinematic recovery process. The four limb segments are shown, each with the notation for their zeroth, first, and second mass moments of inertia. 78
6.7 Comparison of recovered dynamic models, Winter model, and observed contact forces on the *normal* standing action. Sample 860 is marked by a vertical black line. Black: Observed wrench; magenta: Winter model; red, green, and blue: models recovered from the *dynamic*, *normal*, and *stable* datasets. Left: Comparison of contact wrench components. Right: Comparison of corresponding Centre of Pressure. 80
6.8 Comparison of recovered dynamic recovery framework, and expected Winter dynamic parameters (red). The mean and standard deviations of the mean recovered model is shown in blue. The variation between the recovered model and the expected Winter models are shown in red. Left: Base parameters. Right: Modified base parameters to account for rotations of segments frames. 80

6.9 Recovered point mass grid for a representative subject. Heat map showing magnitude of masses at each point where blue to yellow shows increasing mass. Top left: Foot, top right: shank, bottom left: thigh, bottom right: torso. 81

7.1 An overview of the reachable workspace volume method. Left: Motion capture of the two link system returns two trajectories of the system elbow and wrist (green and red). Middle: The upper and lower bounds of these trajectories are then used to create a random sampling of the joint space. These joint space points are then projected into the output-space using the kinematic map (red). Right: The best fit non-convex hull is then generated for these points. This gives an estimate of the workspace (red). The true workspace is shown in blue. 91

7.2 Left: International Society of Biomechanics (ISB) recommendations on definitions of joint coordinates and rotational axes[140]. Skeletal model generated using Biodigital Human[56]. Right: Kinematic model used for the upper limbs. Y_{Gh} is parallel to Y_T, while YY_{Gh} runs parallel to the humerus. Location of the rotational centre of the X_{Gh} joint is given in Thorax (T) coordinates. Rotational pose of the humerus is based on a Y-X-Y rotational sequence about Y_{GH}-X_{GH}-YY_{GH}. Rotation about the Hu joint is about the Hu_Z axis. 93

7.3 Left: Reachable workspace for a healthy subject. Upper extremities are shown in wire-frame with the reachable workspace shown in blue. Plane projected views are shown on the left. Right: Reachable workspace for Patient 1 with mild FSHD (Brooke 1). 94

7.4 Left: Reachable workspace for Patient 3 with moderate FSHD (Brooke 3). Right: Reachable workspace for patient 4 with severe FSHD (Brooke 5). 95

7.5 An illustration of the simplified arm model used in simulation. The arm is modelled as an inertial load I at a distance l from the origin. 98

7.6 Optimisation for a healthy individual. Left: Saggital plane plot of range of motion. Blue: healthy, Red: subject pre-intervention, Green: subject post intervention. Spring stiffness and offset is shown underneath. Right: Torque response plot. Red dashed lines are the limits of the individual's ability. Curves indicate the torque response for each case. 100

7.7 Left: An individual with symmetric 50% strength. Right: An individual with symmetric 20% strength. 101

7.8 Left: An individual with 50% strength in flexion. Right: An individual with 50% strength in extension. 101

7.9 Left: Heatmap showing the change in workspace with spring parameters using the level-set method. The top right blue region shows infeasible points where the system equilibrium is outside of the individual's range of motion. Blue to red transition shows progressively larger workspaces. Right: Reachable set for a single simulation ($k_1 = 75 mNm/deg$ and $\theta_0 = 210 deg$). The static equilibrium point is located at the cross in the centre of the Figure. Blue to red colours show the increasing time taken to move from the equilibrium point to other points in the reachable set. The positions that the individual is able to reach and hold were computed and are indicated as vertical black lines. 103

8.1 Schematic of the pneumatic spring used in the APEX. Three valves allow for the pressurisation and venting of the extension and flexion (P_{flex}, P_{extend}) sides of the pneumatic cylinders. The system is driven by a pressurised supply line, and vents directly to the atmosphere. 108

8.2 The two components of the APEX-β prototype. Left: Backplate showing two pneumatic cylinders and Bowden cable. The Bowden cables connect rigidly to the rod end of the cylinders. The cable wraps around a pulley on the left side of the plate and passes through a cable guide on the right. Right: The two ends of the Bowden pass through a cable guide and wrap around a pulley. Both sides of the pulley are attached to upper-arm and forearm cuffs[11]. 110

8.3 APEX prototype β shown mounted on an individual. Backplate and elbow mounts are shown. The two pneumatic cylinders on the backplate are visible with associated pneumatic lines. The blue cable guide at the top of the back plate routes the linear action of the cylinder along the white Bowden cables to the elbow. 110

8.4 Experimental setup for the hammer curl experiments. Subject wearing motion capture suit with active motion capture markers (red lights). The backplate is mounted on the subject with Bowden cables connecting to the elbow mount. The 3.59 kg barbell is shown. 111

8.5 Summary of APEX results. Top: Raw rep count for the six subjects, for the three trials, across all six APEX modes. Each individual is represented by a a different colour line. First trial in a series is shown on the left, with the third on the right. Middle: Normalised reps. Each individual was normalised by their AC trial for the first, second, and third reps separately. The means and standard deviations are shown on box and whisker plot, with the extrema shown as the whiskers. Bottom: Cartoon of the APEX modes. Forearm shown in the sagittal plane holding a weight. Exoskeleton is shown as a disk on the elbow. The extension side of the cylinder is shown on top, with the flexion side underneath. A sealed chamber at 50 psi is shown in red, while a chamber sealed at atmospheric pressure initially is shown in green. A chamber that is open to the atmosphere is shown in light blue. 112

8.6 Phase portraits of angular acceleration (rad/s^2) against elbow angle (rad) for Elbow flexion/extension in a representative subject. All three trials are shown, with red, green, and blue representing first, second, and third trials. Dotted lines are used for reference. 113
8.7 Phase portraits of angular acceleration (rad/s^2) against elbow angle (rad) for GH elevation/depression (Y_1) in a representative subject. All three trials are shown, with red, green, and blue representing first, second, and third trials. Dotted lines are used for reference. 114
8.8 Phase portraits of angular acceleration (rad/s^2) against elbow angle (rad) for GH plane rotation (Z_1) in a representative subject. All three trials are shown, with red, green, and blue representing first, second, and third trials. Dotted lines are used for reference. 115
8.9 Phase portraits of angular acceleration (rad/s^2) against elbow angle (rad) for GH axial rotation (Z_2) in a representative subject. All three trials are shown, with red, green, and blue representing first, second, and third trials. Dotted lines are used for reference. 116
8.10 APEX-γ. Left: Side view showing the refined backplate, and shoulder harness. Right: Front view showing the elbow mechanism and arm brace. 118

9.1 Summary of results in this thesis[133]. 123

List of Tables

1.1 Comparison of current commercial exoskeletons and the proposed APEX exoskeleton. H&S refer to Hardware and Software respectively. 4

2.1 A summary of the geometric notation used in this thesis 13

2.2 Conversions between the spatial and body frames for $\mathfrak{so}$ and $\mathfrak{se}$ 15

5.1 Kinematic parameters and associated errors in marker positions, angles and angular velocities for the single axis experiments. Mean values shown with standard deviation in parenthesis. 51

5.2 Results of the dynamic model recovery process for three joints at two speeds. Mean values shown with standard deviation in parenthesis. Reference model from [67]. An observation of R is based on the robot's internal measurements of position and velocity, P refers to recovery via the proposed kinematic framework. 56

5.3 Errors and r^2 values for the residuals of the dynamic model recovery process for three joints at two speeds. Mean values shown with standard deviation in parenthesis. Reference model from [67]. An observation of R is based on the robot's internal measurements of position and velocity, P refers to recovery via the proposed kinematic framework. 57

5.4 Errors and r^2 values for the residuals of the dynamic model recovery process for three joints at two speeds. Mean values shown with standard deviation in parenthesis. Reference model from [67]. An observation of R is based on the robot's internal measurements of position and velocity, P refers to recovery via the proposed kinematic framework. 58

5.5 Results of the dynamic model recovery process for three joints at two speeds using different methods for recovering the kinematic state. Mean values shown with standard deviation in parenthesis. Reference model from [67]. 63

5.6 Results of the dynamic model recovery process for three joints at two speeds using different methods for recovering the kinematic state. Mean values shown with standard deviation in parenthesis. Reference model from [67]. 64

6.1 Errors in recovered kinematic parameters and marker re-projection for healthy sit-to-stand actions. The percentage difference between the means of each method and *landmark* method are shown. The standard deviation of each method is shown in parenthesis. 71
6.2 Errors in recovered kinematic parameters and marker re-projection for the three different sit-to-stand strategies for healthy subjects. Mean values shown with standard deviation in parenthesis. 72
6.3 Comparison of recovered wrench, COP, and Torques using the different models on different recovery strategies. 82

7.1 Comparison of computed reachable volume and Brooke Score 93
7.2 Comparison between the direct optimisation and the level-set method for different time horizons. Recovered upper and lower bounds for workspace are shown, along with the associated computation time. 104

Chapter 1

Introduction

Exoskeletons offer a means to assist individuals in their daily life, and as a method of allowing for rehabilitation in the home. The use of these devices is limited by their cost, and the lack of metrics to show efficacy. This has led to slow adoption of these devices due to scepticism of efficacy by clinicians and insurance providers who are reluctant to cover these costly, unproven methods.

This thesis builds a framework for creating a representative model of an individual that can be used for assessment of function and tracking of recovery. These modelling techniques are used to create a *prescription* for a user, specifying the optimal mechanism/actuator framework for assistance. This prescription is then used to guide the creation of a novel low-power assistive exoskeleton- the APEX. By understanding the abilities of the individual, the aim of this work is to individualise intervention selection, decrease clinician/patient burdens, and improve patient outcomes.

1.1 Motivation

There are approximately 6.8 million stroke and 259,000 spinal cord injury survivors in America today[97][119]. The resulting effects on an individual's independence can be severe, with increased rates of depression in both patients and their carers[135]. To improve quality of life and reduce the burdens to patients and their support network, methods to assess, track, and improve function are needed.

One of the complications seen in the assessment of individuals with neuromuscular function is the assessment of true improvement in motor function as opposed to functional recovery due to the use of compensation strategies. The use of robotics is an attractive method for providing intensive, repetitive movement therapy to patients, factors that have been shown to maximise post injury improvement[71]. While some robotic therapeutic methods retrain based on the movement of the hand alone, exoskeletons have the ability to guide the individual limb segments allowing for the recovery of joint synergies[15][58]. It has been noted that while subjects appear to have improved motor function when provided with robot-assisted therapy, the *Activity of Daily Living* (ADL) scales typically used in assessment do not adequately reflect the recovery of an individual[70]. The lack of these assessment tools hampers development of robot-assisted therapeutics, their adoption by clinicians, and coverage by insurance providers[121].

While there has been work in the development of specialised tools for use in clinics and specialist care facilities, one of the goals of exoskeleton therapy is to provide patients with a device that can assist in daily living activities, while providing rehabilitative guidance. There are a number of commercial devices aimed at allowing patients to regain independence (Figure 1.1). These devices represent the current state-of-the-art aimed at use in the home.

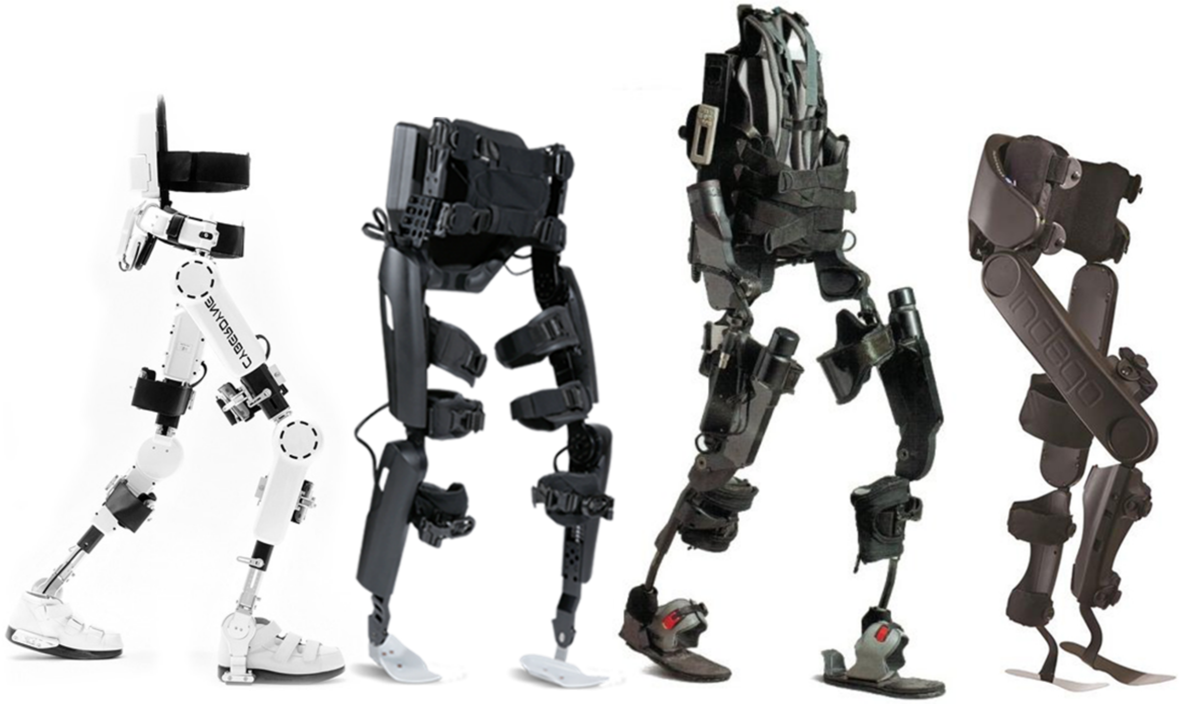

Figure 1.1: Existing commercial exoskeletons. From left to right: HAL-5 lower limb, Rewalk, eLegs, and Indego.

While the field of assistive exoskeletons is new, there appears to be a convergence in design, with the majority of focus on devices for the lower limbs. By allowing patients to ambulate, it offers individuals access to areas that may have otherwise been inaccessible through wheelchairs. This focus on the lower limbs neglects the important problems faced by individuals who suffer from upper limb conditions. Upper limb disabilities dramatically reduce an individual's ability to live autonomously, requiring a carer for activities of daily living. This leads to a financial burden of approximately \$30k p/a, and a reduction of independence[130].

1.1.1 Clinical Need

People are different. These differences arise from a multitude of factors such as age, prior injuries, race, activity level, sex, and genetic variation. The effect of these differences are often ignored by clinical measures, with population measures such as *Body Mass Index* being used to quantify an individual's health. This oversimplification leads to standardised clinical pathways where patients may spend significant resources on interventions that show no benefit. The underlying cause of this perceived lack of change needs to be understood. Is the intervention ineffective, or is the quantification of performance inappropriate for tracking the changes in the patient's function?

1.1.2 Medical Metrics

The existing metrics used in clinics today are still limited by the translation of tools from the biomechanics community to the broader population. The quantitative measures that are used are crude, consisting of timed function tests such as five-times sit-to stand[134], point score measures (such as the Berg Balance[12], Brooke[18], and Box and Block[23] scales). While simple and fast to perform (with most tests taking under 5 minutes), these methods lack the granularity for determining small scale changes in function at the joint level. Measures such as the Fugl-Meyer[39][43] and Wolf Motor Function tests[137] have been shown to provide a finer resolution measure, but can be time consuming to perform with typical testing time requiring approximately 30 minutes per test.

1.1.3 State-of-the-art

In contrast to the tools currently being used in clinics, there have been significant advances in affordable sensors that has led to a new generation of assessment tools. One of the most prevalent approaches is the use of depth cameras such as the Kinect to track the limbs of a patient. These methods have been used to estimate postural control and sway in quiet standing[25][143], and the space an individual can reach[69]. The development of affordable balance boards such as the Wii balance board has allowed for affordable measures of standing and balance[24][145].

While these methods have shown promise, the major challenges behind the use of these methods is the need for retraining clinicians to use and understand the results of these tools. This is complicated by the lack of financial incentives from insurance providers to use these technologies. Furthermore, these affordable systems are less accurate than the high end devices frequently used in biomechanics laboratories. The provided skeletons can return joint centres with significant variation in joint position compared to high end motion capture, and between samples[132].

1.1.4 Assistive Devices

Table 1.1 compares currently available active exoskeletons, along with the APEX (Active/Passive EXoskeleton), a novel assistive device presented in this thesis. From this table, it is clear that operational life, and device cost are major obstacles in wide-scale adoption of these technologies.

The choice of the implemented controller is important, with some forms of robotic assistance negatively impacting an individual's rehabilitative progress[79]. Impedance control[51][52][142] allows for the shaping of the effective mass, inertias, visco-elasticities, and stiffnesses of the human-robot system. These methods can be used to provide assistance, while still allowing the individual to have complete control of their actions. This can result in an assistance-as-needed framework where the user is encouraged to utilise their own strengths whenever possible[34].

The drawback of impedance control is the requirement for high fidelity actuators and sensors. Knowledge of the dynamic parameters of the composed human-robot system is required to ensure the safety and efficacy of these methods. This is typically estimated through height mass scaling[27], a modelling choice that does not adequately capture the variations within populations[31], especially those who may be recovering from disabilities.

Table 1.1: Comparison of current commercial exoskeletons and the proposed APEX exoskeleton. H&S refer to Hardware and Software respectively.

Criteria	HAL-5[110]	Re-Walk[118]	eLegs[46]	Indego[95]	APEX
Weight (lbs)	51	51	45	27	7.5
Operation Time	<3 hours	8 hours	6 hours	4 hours	1 day
Price (buy)	-	\$69.5k	\$130k	\$80k	\$2k
Price (rent)	\$5k + \$1.7k p/m	-	-	-	\$500
Customisation	S	S	S	S	H&S

1.2 Contributions

This thesis makes a number of contributions in the fields of dynamical modelling, biomechanics, and robotics. This section outlines the main contributions of this thesis, their location in this text, and the corresponding publications by the author.

1.2.1 A Geometric Dynamic Recovery Method

A unified form for geometric modelling is covered in Chapter 2. Due to differences in notation, a number of key results have been omitted from a number of texts, in particular the dynamic recursion equations by Park[102]. These results have been translated, and the notation clarified to present a clearer picture of the mathematics used in this work.

Building on these mathematical fundamentals a new method for performing kinematic recovery is introduced in Chapter 3. This method allows for the generation of an individualised human model with few apriori assumptions made on the subject's abilities. The number of limb segments, allocation of markers to these segments, location of the joints, and length of the limbs are recovered automatically through a recursive algorithm. The joint angles and their derivatives are found directly from the motion data. This recovers a dynamically consistent state estimate directly from the observed motion capture points. This dynamic consistency allows for recovery in the presence of markers disappearing or appearing to move faster than possible. Furthermore, the joint angles and their derivatives are filtered in a manner that ensures that the laws of motion hold.

The existing geometric modelling literature is then extended in Chapter 4 with the development of a *Dynamic Identification Model* (DIM). A symbolic relationship is formed between the contact forces and the kinematics of the system based on the dynamic modelling work used in the Denavit-Hartenberg literature[65]. As a geometric approach is used, the compound twists recovered from the kinematic modelling process can be directly translated in to a dynamic model without simplification. Modifications are made to ensure that the recovered parameters are physically realistic, i.e. the masses of segments are non-negative and the inertial matrices are real, symmetric matrices. A minimal, physically consistent model is formed using the work by Ayusawa[8] as an inspiration. The resulting geometric DIM provides a linear relationship of the form $\boldsymbol{Y}\boldsymbol{\phi} = \boldsymbol{\Gamma}$ where the dynamic parameters of the system are elements in the $\boldsymbol{\phi}$ vector. The formulation developed in this thesis provides a well conditioned regressor $\boldsymbol{Y}$, while allowing for physical consistency of the corresponding dynamic parameters $\boldsymbol{\phi}$.

The use of these methods as an experimental tool are examined in Chapter 5 through the study of a robotic system. The recovered kinematic and dynamic models are compared to the current published models, with the recovered joint state compared to the measurements taken directly from the robot encoders. The accuracy and precision of the recovered model and state is investigated by varying the robotic actions. A dynamic model is then derived from the recovered kinematic models. These models are validated symbolically by comparing the form of the DIM against the Denavit-Hartenberg approach. The precision and accuracy of the dynamic model is then examined through the error analysis of the recovered dynamic parameters and torques. The effect of common experimental and sensor errors are then simulated, providing guidelines on the application of these modelling techniques.

1.2.2 Methods for Individualised Human Modelling

Chapter 6 shows the application of these modelling methods on the *five-times sit-to-stand* protocol, a commonly used clinical test to assess a patient's stability. The only alterations to the clinical test were the additions of sensing equipment, with the protocol remaining the same with the aim of minimising the clinical retraining burden and the simultaneous tracking of the existing metrics. The proposed framework was used to generate a representative human model using under thirty seconds of standing data. In contrast to other methods, no machine learning is used and no apriori assumptions were made on the subject's model based on their age, sex, height, mass, race etc. This resulted in a non-prejudicial, structured model recovery process.

One of the issues that can arise when using conventional modelling approaches is the over/under-fitting of the model parameters depending on the number of system unknowns and observations. In contrast, the presented framework offers a sequential recovery process, recovering sets of parameters with physical meaning. This results in a well posed recovery process, with the resulting model being a distillation of the system observables allowing for automatic simplification of the system.

1.2.3 Prescriptive Assistive Devices

These modelling methods are then used in generate a subject-specific assistive device. A framework is introduced in Chapter 7 to determine the optimal assistance parameters from a representative human model[82][85]. Two methods of implementing this framework are discussed, with applications to a simulated shoulder joint. This highlights the utility of these methods to reduce the amount of manual tuning required, and provides a *prescriptive* method for system design and analysis.

The results of these studies are used in the development of a new method to assist an individual. The achievable workspace for an individual can be altered by varying both the active and passive responses at each joint. The abilities of a user can be altered through the variation of these joint responses. Chapter 8 introduces the development of an upper limb assistive exoskeleton that utilises these ideas[84]. The joint dynamics of a user's elbow is altered using a pneumatic system. Passive assistance of the limb is therefore afforded by changing the dynamic response of the joint. As the assistive device does not require any energy to maintain this dynamic state the total cost to provide assistance is substantially lower than for active methods.

The combined effect of this coupled human-robot system is assessed using the biomechanic methods introduced in this work[83]. The effect of different controllers on the motions of the shoulder and elbow are examined allowing for investigation into compensatory actions. The analysis of the coupled system allows for the efficacy of the intervention to be assessed and guides the development of future devices.

Chapter 2

Mathematical Preliminaries

This chapter outlines the background mathematics that will be used in this thesis. It acts as a primer for the underlying knowledge behind this work. This chapter can be skipped without loss of continuity, with sections being referred to in the later chapters.

2.1 Rotations and Rigid-Body Motion

In this thesis we will be relying on results from rigid-body mechanics. This treats systems as a number of rigid segments connected by joints. This formulation allows for a number of results from mathematics, physics, and robotics to be applied to complex artificial and biological systems. This section is based on the treatment of rigid-body systems by Murray[94].

2.1.1 Coordinate Frames

A coordinate frame is a system for uniquely determining the position of a point in a space. Given a coordinate frame, any point can be assigned coordinates in that frame. Consider the simple system shown in Figure 2.1. When $\theta_1 = 0$ the two coordinate frames will overlap. This means that the coordinates of point $\boldsymbol{q}$ will be the same in both frames.

When $\theta_1 \neq 0$, the two coordinate frames do not overlap. This means that the corresponding coordinates of point $\boldsymbol{q}$ will be different. The coordinates of the point $\boldsymbol{q}$ in coordinate frames A and B are denoted $\boldsymbol{q}_A$ and $\boldsymbol{q}_B$ respectively. Coordinates $\boldsymbol{q}_A$ and $\boldsymbol{q}_B$ are related by a *rigid-body transformation*. A rigid-body transformation preserves the distance and angle between vectors. The simplest form is a rotation about a point as shown in Figure 2.1.

2.1.2 Rotations

Consider the coordinates $\boldsymbol{q}_A$ and $\boldsymbol{q}_B$ of the same point $\boldsymbol{q}$ as viewed in the coordinate frames A and B respectively. In this simple 2D example, the coordinates of point $\boldsymbol{q}$ can be written

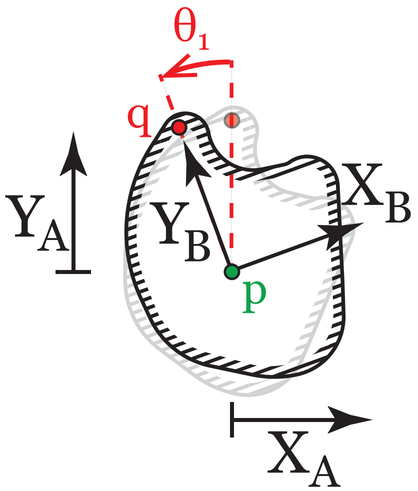

Figure 2.1: Two coordinate frames A and B with a common origin $\boldsymbol{p}$. Frame B is attached to the rigid body. The rotation about the point $\boldsymbol{p}$ is parametrised by the angle θ_1. The point $\boldsymbol{q}$ is attached rigidly to the rigid body.

in terms of their x and y component:

$$\boldsymbol{q}_A = \begin{bmatrix} x_A \\ y_A \end{bmatrix} \qquad \boldsymbol{q}_B = \begin{bmatrix} x_B \\ y_B \end{bmatrix} \tag{2.1}$$

Given a y_B coordinate, it is possible to write the following relationship to the A frame:

$$\begin{bmatrix} x_A \\ y_A \end{bmatrix} = \begin{bmatrix} -sin(\theta_1) \\ cos(\theta_1) \end{bmatrix} y_B \tag{2.2}$$

The x_B coordinate can be written similarly as:

$$\begin{bmatrix} x_A \\ y_A \end{bmatrix} = \begin{bmatrix} cos(\theta_1) \\ sin(\theta_1) \end{bmatrix} x_B \tag{2.3}$$

These two expressions can be combined to give a transformation of points from the B frame to the A frame:

$$\boldsymbol{q}_A = \begin{bmatrix} x_A \\ y_A \end{bmatrix} = \begin{bmatrix} cos(\theta_1) \\ sin(\theta_1) \end{bmatrix} x_B + \begin{bmatrix} -sin(\theta_1) \\ cos(\theta_1) \end{bmatrix} y_B = \begin{bmatrix} cos(\theta_1) & -sin(\theta_1) \\ sin(\theta_1) & cos(\theta_1) \end{bmatrix} \begin{bmatrix} x_B \\ y_B \end{bmatrix} = \boldsymbol{R}_{A,B}\boldsymbol{q}_B \tag{2.4}$$

The matrix $\boldsymbol{R}_{A,B} \in \mathbb{R}^{2\times 2}$ is the *rotation* matrix and gives a mapping of points from the B frame to the A frame.

The mapping from the A frame to the B frame can be constructed in a similar manner:

$$\boldsymbol{q}_B = \begin{bmatrix} x_B \\ y_B \end{bmatrix} = \begin{bmatrix} cos(\theta_1) \\ -sin(\theta_1) \end{bmatrix} x_A + \begin{bmatrix} sin(\theta_1) \\ cos(\theta_1) \end{bmatrix} y_A = \begin{bmatrix} cos(\theta_1) & sin(\theta_1) \\ -sin(\theta_1) & cos(\theta_1) \end{bmatrix} \begin{bmatrix} x_A \\ y_A \end{bmatrix} = \boldsymbol{R}_{B,A}\boldsymbol{q}_A \tag{2.5}$$

This process can be extended into three dimensions forming the remapping matrix $\boldsymbol{R} \in \mathbb{R}^{3\times 3}$.

2.1.2.1 Properties of Rotation Matrices

From the construction of rotation matrices, the columns $\boldsymbol{c}_i \in \mathbb{R}^{n\times 1}$ for $i \in [1, n]$ of the rotation matrix $\boldsymbol{R}^{n\times n}$ are mutually orthonormal. This results in the matrix $\boldsymbol{R}$ being orthogonal whereby the following property holds:

$$\boldsymbol{R}^T\boldsymbol{R} = \boldsymbol{R}\boldsymbol{R}^T = \boldsymbol{I} \tag{2.6}$$

This highlights a key property of all rotation matrices, the inverse of a rotation matrix is its transpose.

From the above, the determinant of $\boldsymbol{R}$ will be ± 1. If a right handed coordinate frame is adopted, then $\boldsymbol{c}_1 = \boldsymbol{c}_2 \times \boldsymbol{c}_3$. Therefore:

$$det(\boldsymbol{R}) = \boldsymbol{c}_1^T\left(\boldsymbol{c}_2 \times \boldsymbol{c}_3\right) = \boldsymbol{c}_1^T\boldsymbol{c}_1 = +1 \tag{2.7}$$

2.1.3 Rotations and Translations

This can be extended to the case where the origins of the two coordinate frames are not aligned. Consider the system shown in Figure 2.2. Frame B can now be represented by a combination of a translation $\boldsymbol{p}_{A,B}$ and a rotation $\boldsymbol{R}_{A,B}$. Using the results for pure rotations, the B frame coordinates of point $\boldsymbol{q}$ can be written in the A frame via the expression:

$$\boldsymbol{q}_A = \boldsymbol{p}_{A,B} + \boldsymbol{R}_{A,B}\boldsymbol{q}_B \tag{2.8}$$

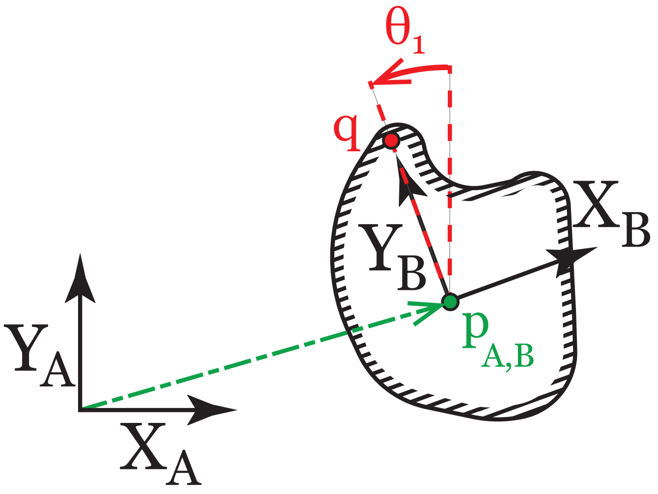

Figure 2.2: Two coordinate frames A and B. Frame B is attached to the rigid body. $\boldsymbol{p}_{A,B}$ are the coordinates of the origin of the B frame as viewed in the A coordinate frame. The rotation about the point $\boldsymbol{p}$ is parametrised by the angle θ_1. The point $\boldsymbol{q}$ is attached rigidly to the rigid body.

2.1.4 Homogeneous Coordinates

This expression for the rigid-body transformation for the point $\boldsymbol{q}$ can be rewritten in matrix form $\boldsymbol{g}_{A,B}$ as:

$$\begin{bmatrix} \boldsymbol{q}_A \\ 1 \end{bmatrix} = \begin{bmatrix} \boldsymbol{R}_{A,B} & \boldsymbol{p}_{A,B} \\ \mathbf{0} & 1 \end{bmatrix} \begin{bmatrix} \boldsymbol{q}_B \\ 1 \end{bmatrix} = \boldsymbol{g}_{A,B} \begin{bmatrix} \boldsymbol{q}_B \\ 1 \end{bmatrix} \tag{2.9}$$

This gives rise to the homogeneous representation for rigid-body motion where points and vectors are written as:

$$\text{Points: } \begin{bmatrix} \boldsymbol{q} \\ 1 \end{bmatrix} \in \mathbb{R}^{4\times 1} \qquad \text{Vectors: } \begin{bmatrix} \boldsymbol{v} \\ 0 \end{bmatrix} \in \mathbb{R}^{4\times 1}$$

2.2 Geometric Robotics- Introduction

The geometric approach to describing rigid-body motion is based on the structure of homogeneous matrices. All rigid body motions can be decomposed into a rotation and a translation component. By studying the form of these constituent elements, it is possible to create an alternative formulation for describing the motion of a rigid-body system. This is the *geometric* formulation for rigid-body motion.

This thesis will adopt a more elaborated form of the *west coast* geometric robotics notation used by Murray[94]. This is in contrast to the *east coast* notation used by Park[102]. The elaboration is necessary due to common confusion between choices of frames of reference, and the differences between the two notation styles. This section will outline key results, but will avoid the full proofs shown in [94][102][112].

2.2.1 Rotations

It was shown in Section 2.1.2 that rotation matrices have special conditions on their determinant and inverse. These conditions define the *special orthogonal* group of matrices:

$$SO(n) = \left\{ \boldsymbol{R} \in \mathbb{R}^{n\times n} : \boldsymbol{R}\boldsymbol{R}^T = \mathbb{I}_n, det(\boldsymbol{R}) = +1 \right\} \tag{2.10}$$

SO is a mathematical group, and satisfies the properties of:

Closure $\boldsymbol{R}_1, \boldsymbol{R}_2 \in SO \implies (\boldsymbol{R}_1\boldsymbol{R}_2) \in SO$

Identity $\exists \mathbb{I} \in SO\, s.t.\, \mathbb{I}\boldsymbol{R} = \boldsymbol{R}\mathbb{I} = \boldsymbol{R}$

Inverse For each $\boldsymbol{R} \in SO\, \exists!\, \boldsymbol{R}^{-1} \in SO\, s.t.\, \boldsymbol{R}^{-1}\boldsymbol{R} = \boldsymbol{R}\boldsymbol{R}^{-1} = \mathbb{I}$

Associativity $\boldsymbol{R}_1, \boldsymbol{R}_2, \boldsymbol{R}_3 \in SO \implies (\boldsymbol{R}_1\boldsymbol{R}_2)\boldsymbol{R}_3 = \boldsymbol{R}_1(\boldsymbol{R}_2\boldsymbol{R}_3)$

$SO(n)$ is more specifically a *Lie group* and has the associated *Lie algebra* $\mathfrak{so}(n)$ where $\mathfrak{so}(n)$ is a $n \times n$ skew-symmetric matrix. For rotations in 3D, $\mathfrak{so}(3)$ can be parametrised by a unit vector $\boldsymbol{\omega} \in \mathbb{R}^{3\times 1}$, a magnitude $\theta \in \mathbb{R}$, and the hat operator $\hat{\cdot}$.

$$\hat{\boldsymbol{\omega}}\theta = \widehat{\begin{bmatrix} \omega_1 \\ \omega_2 \\ \omega_3 \end{bmatrix}}\theta = \begin{bmatrix} 0 & -\omega_3 & \omega_2 \\ \omega_3 & 0 & -\omega_1 \\ -\omega_2 & \omega_1 & 0 \end{bmatrix}\theta \in \mathfrak{so}(3) \tag{2.11}$$

Given this parametrisation of a skew-symmetric matrix, the associated rotation matrix is given by the matrix exponent:

$$e^{\hat{\boldsymbol{\omega}}\theta} \in SO(3) \tag{2.12}$$

The choice of this parametrisation becomes clear when the matrix exponent is performed. Using the identity $\hat{\boldsymbol{\omega}}^3 = -\hat{\boldsymbol{\omega}}$, the matrix exponential becomes:

$$\begin{aligned} e^{\hat{\boldsymbol{\omega}}\theta} &= \mathbb{I} + \frac{\theta}{1!}\hat{\omega} + \frac{\theta^2}{2!}\hat{\omega}^2 + \frac{\theta^3}{3!}\hat{\omega}^3 \cdots \\ &= \mathbb{I} + \left(\frac{\theta}{1!} - \frac{\theta^3}{3!} + \dots\right)\hat{\omega} + \left(\frac{\theta^2}{2!} - \frac{\theta^4}{4!} + \dots\right)\hat{\omega}^2 \\ &= \mathbb{I} + \hat{\omega} sin(\theta) + \hat{\omega}^2\left(1 - cos(\theta)\right) \end{aligned} \tag{2.13}$$

This is the *Rodrigues' formula* for rotations about the axis $\boldsymbol{\omega}$ by angle θ.

The hat operator introduced in Equation 2.11 is the matrix form of the cross product. For $\boldsymbol{u}, \boldsymbol{v} \in \mathbb{R}^{3\times1}$:

$$\boldsymbol{u} \times \boldsymbol{v} = \begin{bmatrix} u_1 \\ u_2 \\ u_3 \end{bmatrix} \times \begin{bmatrix} v_1 \\ v_2 \\ v_3 \end{bmatrix} = \begin{bmatrix} u_2v_3 - u_3v_2 \\ u_3v_1 - u_1v_3 \\ u_1v_2 - u_2v_1 \end{bmatrix} = \begin{bmatrix} 0 & -u_3 & u_2 \\ u_3 & 0 & -u_1 \\ -u_2 & u_1 & 0 \end{bmatrix} \begin{bmatrix} v_1 \\ v_2 \\ v_3 \end{bmatrix} = \hat{\boldsymbol{u}}\boldsymbol{v} \tag{2.14}$$

A useful property of the relation between the axis of rotation $\boldsymbol{\omega}$, the corresponding matrix in $\mathfrak{so}$, and the rotation in SO is a matrix form for the remapping of an axis by a rotation $\boldsymbol{R}$.

$$\boldsymbol{R}\hat{\boldsymbol{\omega}}\boldsymbol{R}^T = \widehat{(\boldsymbol{R}\boldsymbol{\omega})} = (\boldsymbol{R}\boldsymbol{\omega})^\wedge \tag{2.15}$$

Equation 2.15 is Lemma 2.1 from Murray[94] and remaps elements of $\mathfrak{so}$ by a rotation $\boldsymbol{R}$.

2.2.2 Rigid-Body Motion

Given this relation between the Lie Group of Rotations, and the corresponding Lie Algebra, it is possible to generate a similar relationship on the homogeneous matrices representing rigid-body motion introduced in Section 2.1.4. Homogeneous matrices are expressed mathematically as the Special Euclidean group SE.

$$SE(n) = \{(\boldsymbol{p}, \boldsymbol{R}) : \boldsymbol{p} \in \mathbb{R}^n, \boldsymbol{R} \in SO(n)\} = \mathbb{R}^n \times SO(n) \tag{2.16}$$

In the three dimensional case this is simply a standard 3D rotation $\boldsymbol{R} \in SO(3)$ and a translation vector $\boldsymbol{p} \in \mathbb{R}^3$.

As a group, this space of homogeneous transforms $SE(3)$ satisfies the properties of a group:

Closure $\boldsymbol{g}_1, \boldsymbol{g}_2 \in SO \implies (\boldsymbol{g}_1\boldsymbol{g}_2) \in SO$

Identity $\exists \mathbb{I} \in SE\, s.t.\, \mathbb{I}\boldsymbol{g} = \boldsymbol{g}\mathbb{I} = \boldsymbol{g} \in SE$

Inverse For each $\boldsymbol{g} \in SE\, \exists!\, \boldsymbol{g}^{-1} \in SE\, s.t.\, \boldsymbol{g}^{-1}\boldsymbol{g} = \boldsymbol{g}\boldsymbol{g}^{-1} = \mathbb{I}$

Associativity $\boldsymbol{g}_1, \boldsymbol{g}_2, \boldsymbol{g}_3 \in SO \implies (\boldsymbol{g}_1\boldsymbol{g}_2)\boldsymbol{g}_3 = \boldsymbol{g}_1(\boldsymbol{g}_2\boldsymbol{g}_3)$

The inverse of a rigid-body transform $\boldsymbol{g}^{-1}$ is given by:

$$\boldsymbol{g} = \begin{bmatrix} \boldsymbol{R} & \boldsymbol{p} \\ \boldsymbol{0} & 1 \end{bmatrix} \qquad \boldsymbol{g}^{-1} = \begin{bmatrix} \boldsymbol{R}^T & -\boldsymbol{R}^T\boldsymbol{p} \\ \boldsymbol{0} & 1 \end{bmatrix} \tag{2.17}$$

The Special Euclidean Group has the Lie Algebra $\mathfrak{se}$ of the form:

$$\mathfrak{se}(n) = \left\{ (\boldsymbol{v}, \hat{\boldsymbol{\omega}}) : \boldsymbol{v} \in \mathbb{R}^{n\times 1}, \hat{\boldsymbol{\omega}} \in \mathfrak{so}(n) \right\} \tag{2.18}$$

where elements of $\mathfrak{se}(3)$ can be parametrised by the twist vector $\boldsymbol{\xi} \in \mathbb{R}^{6\times 1}$ and the wedge operator $\hat{\cdot}$:

$$\hat{\boldsymbol{\xi}} = \widehat{\begin{bmatrix} \boldsymbol{v} \\ \boldsymbol{\omega} \end{bmatrix}} = \begin{bmatrix} \hat{\boldsymbol{\omega}} & \boldsymbol{v} \\ \boldsymbol{0} & 0 \end{bmatrix} \tag{2.19}$$

Elements of Lie Group and Lie Algebra are related via the matrix exponential:

$$\boldsymbol{g} = e^{\hat{\boldsymbol{\xi}}\theta} \tag{2.20}$$

The exponential mapping acts as a link between the Lie Algebra and Lie Group for both rotations and rigid-body motion.

2.2.3 Lie Groups and Algebras

Sections 2.2.1 and 2.2.2 introduced a number of Lie groups and Lie Algebras. This section will introduce the notation and common operations we will be using in this thesis, and the matrix form of common operations. Table 2.1 summarises the relationships between the parametrisation of the Lie Algebra, the form of elements in the Lie Algebra, and the Lie Group itself.

Table 2.1: A summary of the geometric notation used in this thesis

Element	Rotations	Rigid-body Motion
Parametrisation	$\boldsymbol{\omega} = \begin{bmatrix} \omega_1 \\ \omega_2 \\ \omega_3 \end{bmatrix} \in \mathbb{R}^3$	$\boldsymbol{\xi} = \begin{bmatrix} \boldsymbol{v} \\ \boldsymbol{\omega} \end{bmatrix} \in \mathbb{R}^6$
$\updownarrow$	$\hat{\boldsymbol{\omega}} = \begin{bmatrix} 0 & -\omega_3 & \omega_2 \\ \omega_3 & 0 & -\omega_1 \\ -\omega_2 & \omega_1 & 0 \end{bmatrix}$	$\hat{\boldsymbol{\xi}} = \begin{bmatrix} \hat{\boldsymbol{\omega}} & \boldsymbol{v} \\ \boldsymbol{0} & 0 \end{bmatrix}$
Lie Algebra	$\hat{\boldsymbol{\omega}} \in \mathfrak{so}(3)$	$\hat{\boldsymbol{\xi}} \in \mathfrak{se}(3)$
$\updownarrow$	$\boldsymbol{R} = e^{\hat{\boldsymbol{\omega}}}$	$\boldsymbol{g} = e^{\hat{\boldsymbol{\xi}}}$
Lie Group	$\boldsymbol{R} \in SO(3)$	$\boldsymbol{g} \in SE(3)$

While it is possible to use the representations in Table 2.1 to describe rigid-body motions, it is useful to convert this mathematical form into one that is more suited to the parametrisation of rigid-body systems. If we return to the simple rotation shown in Figure 2.1, the velocity of the point $\boldsymbol{q}$ can be expressed as the cross-product between the angular velocity $\boldsymbol{\omega}$ and the vector from the origin to the point at that instance in time $\boldsymbol{q}_A(t)$:

$$\dot{\boldsymbol{q}}_A(t) = \boldsymbol{\omega}_A \times \boldsymbol{q}_A(t) \tag{2.21}$$

The solution to this differential equation can be written as:

$$\boldsymbol{q}_A(t) = e^{\hat{\boldsymbol{\omega}}_A t}\boldsymbol{q}_A(0) \tag{2.22}$$

where $\boldsymbol{q}_A(0)$ are the coordinates of point $\boldsymbol{q}$ as viewed in the A frame at $t = 0$. This is known as the *initial configuration* of the point $\boldsymbol{q}$.

If the vector representing the axis of rotation $\boldsymbol{\omega}$ is a unit vector, the time for rotation t can instead be represented by the amount of rotation, the angle θ. This gives the relation:

$$\boldsymbol{q}_A(\theta) = e^{\hat{\boldsymbol{\omega}}_A \theta}\boldsymbol{q}_A(0) \tag{2.23}$$

which is identical to the parametrisation shown in Equation 2.13. This gives an expression for movement of a point from its initial configuration to its new configuration given a rotation of θ radians about the axis of rotation $\boldsymbol{\omega}_A$ given in the A frame.

From the definition of SO in Equation 2.10, we have the relation: $\boldsymbol{R}^{-1}(t)\boldsymbol{R}(t) = \mathbb{I}$. By differentiation, this expression gives the relation showing that $\boldsymbol{R}_{B,A}\dot{\boldsymbol{R}}_{A,B}$ is skew-symmetric:

$$\begin{aligned}
\boldsymbol{R}_{B,A}\boldsymbol{R}_{A,B} &= \mathbb{I} \\
\dot{\boldsymbol{R}}_{B,A}\boldsymbol{R}_{A,B} + \boldsymbol{R}_{B,A}\dot{\boldsymbol{R}}_{A,B} &= 0 \\
\boldsymbol{R}_{B,A}\dot{\boldsymbol{R}}_{A,B} &= -\dot{\boldsymbol{R}}_{B,A}\boldsymbol{R}_{A,B} \\
\boldsymbol{R}_{B,A}\dot{\boldsymbol{R}}_{A,B} &= -\left(\boldsymbol{R}_{B,A}\dot{\boldsymbol{R}}_{A,B}\right)^T
\end{aligned} \tag{2.24}$$

The term $\boldsymbol{R}_{B,A}\dot{\boldsymbol{R}}_{A,B}$ takes points from frame B, finds the associated velocities, then returns them back in frame B. This is known as the *body angular velocity* $\boldsymbol{\omega}^b_{A,B}$:

$$\hat{\boldsymbol{\omega}}^b_{A,B} = \boldsymbol{R}_{B,A}\dot{\boldsymbol{R}}_{A,B} \tag{2.25}$$

This process can be repeated using $\boldsymbol{R}(t)\boldsymbol{R}^{-1}(t) = \mathbb{I}$ to obtain an expression for the *spatial angular velocity* which takes points from the A frame, converts them into the B frame, then returns the associated velocities in the A frame:

$$\hat{\boldsymbol{\omega}}^s_{A,B} = \dot{\boldsymbol{R}}_{A,B}\boldsymbol{R}_{B,A} \tag{2.26}$$

This then gives two expressions for the velocity of a point $\boldsymbol{q}$ depending on the frame of the viewer:

$$\begin{aligned}
\dot{\boldsymbol{q}}_A(t) &= \hat{\boldsymbol{\omega}}^A_{A,B}(t)\boldsymbol{q}_A(t) \\
\dot{\boldsymbol{q}}_B(t) &= \hat{\boldsymbol{\omega}}^B_{A,B}(t)\boldsymbol{q}_B(t)
\end{aligned} \tag{2.27}$$

The coordinates of the point as given in the B frame is constant giving the relation $\boldsymbol{q}_B(t) = \boldsymbol{q}_B(0)$. This gives the expressions:

$$\begin{gathered}\dot{\boldsymbol{q}}_A(\theta) = \dot{\boldsymbol{R}}_{A,B}(\theta)\boldsymbol{R}_{B,A}(\theta)\boldsymbol{q}_A(\theta) = \dot{\boldsymbol{R}}_{A,B}(\theta)\boldsymbol{q}_B(0) \\ \dot{\boldsymbol{q}}_B = \hat{\boldsymbol{\omega}}^B_{A,B}\boldsymbol{q}_B(0)\end{gathered} \tag{2.28}$$

The velocity relations for pure rotations can be extended to full rigid-body motion. Equation 2.23 can be extended, giving an expression for the homogeneous matrix $\boldsymbol{g}_{A,B}(\theta)$ from an initial configuration $\boldsymbol{g}_{A,B}(0)$:

$$\boldsymbol{g}_{A,B}(\theta) = e^{\hat{\boldsymbol{\xi}}_A\theta}\boldsymbol{g}_{A,B}(0) \tag{2.29}$$

Equations 2.25 and 2.26 can be extended to define the body and spatial twists:

$$\hat{\boldsymbol{V}}^s_{A,B} = \dot{\boldsymbol{g}}_{A,B}(\theta)\boldsymbol{g}^{-1}_{A,B}(\theta) \tag{2.30}$$

$$\hat{\boldsymbol{V}}^b_{A,B} = \boldsymbol{g}^{-1}_{A,B}(\theta)\dot{\boldsymbol{g}}_{A,B}(\theta) \tag{2.31}$$

2.2.4 The Adjoint Map

Section 2.2.3 introduced two frames for viewing the velocities of a point: the static *spatial* frame, and the moving *body* frame. These conversions are summarised in Table 2.2.

These conversions are highly useful to find expressions for $\boldsymbol{\omega}$ and $\boldsymbol{\xi}$ due to a change in coordinate frame. They are referred to as the *Adjoints* for $\mathfrak{so}$ and $\mathfrak{se}$. Given a corresponding element in SO or SE, the Adjoint is defined by:

$$\begin{gathered}Ad_{\boldsymbol{R}_{A,B}}\left(\hat{\boldsymbol{\omega}}^B_{A,B}\right) = \boldsymbol{R}_{A,B}\hat{\boldsymbol{\omega}}^B_{A,B}\boldsymbol{R}^{-1}_{A,B} = \hat{\boldsymbol{\omega}}^A_{A,B} \\ Ad_{\boldsymbol{g}_{A,B}}\left(\hat{\boldsymbol{\xi}}^B_{A,B}\right) = \boldsymbol{g}_{A,B}\hat{\boldsymbol{\xi}}^B_{A,B}\boldsymbol{g}^{-1}_{A,B} = \hat{\boldsymbol{\xi}}^A_{A,B}\end{gathered} \tag{2.32}$$

Using Equations 2.15, the Adjoint can be written as the matrix $\boldsymbol{Ad}$ on the parametrised form of the Lie Algebra:

$$\begin{gathered}\boldsymbol{\omega}^A_{A,B} = \boldsymbol{Ad}_{\boldsymbol{R}_{A,B}}\boldsymbol{\omega}^B_{A,B} = \left[\boldsymbol{R}_{A,B}\right]\boldsymbol{\omega}^B_{A,B} \\ \boldsymbol{\xi}^A_{A,B} = \boldsymbol{Ad}_{\boldsymbol{g}_{A,B}}\boldsymbol{\xi}^B_{A,B} = \begin{bmatrix}\boldsymbol{R}_{A,B} & \hat{\boldsymbol{p}}_{A,B}\boldsymbol{R}_{A,B} \\ \boldsymbol{0} & \boldsymbol{R}_{A,B}\end{bmatrix}\boldsymbol{\xi}^B_{A,B}\end{gathered} \tag{2.33}$$

Table 2.2: Conversions between the spatial and body frames for $\mathfrak{so}$ and $\mathfrak{se}$

Frame	Rotations	Rigid-body Motion
Spatial	$\hat{\boldsymbol{\omega}}^A_{A,B} = \dot{\boldsymbol{R}}_{A,B}\boldsymbol{R}_{B,A}$	$\hat{\boldsymbol{\xi}}^A_{A,B} = \dot{\boldsymbol{g}}_{A,B}\boldsymbol{g}_{B,A}$
$\updownarrow$	$\hat{\boldsymbol{\omega}}^A_{A,B} = \boldsymbol{R}_{A,B}\hat{\boldsymbol{\omega}}^B_{A,B}\boldsymbol{R}_{B,A}$ $\hat{\boldsymbol{\omega}}^B_{A,B} = \boldsymbol{R}_{B,A}\hat{\boldsymbol{\omega}}^A_{A,B}\boldsymbol{R}_{A,B}$	$\hat{\boldsymbol{\xi}}^A_{A,B} = \boldsymbol{g}_{A,B}\hat{\boldsymbol{\xi}}^B_{A,B}\boldsymbol{g}_{B,A}$ $\hat{\boldsymbol{\xi}}^B_{A,B} = \boldsymbol{g}_{B,A}\hat{\boldsymbol{\xi}}^A_{A,B}\boldsymbol{g}_{A,B}$
Body	$\hat{\boldsymbol{\omega}}^B_{A,B} = \boldsymbol{R}_{B,A}\dot{\boldsymbol{R}}_{A,B}$	$\hat{\boldsymbol{\xi}}^B_{A,B} = \boldsymbol{g}_{B,A}\dot{\boldsymbol{g}}_{A,B}$

Using Equations 2.6 and 2.17 (which give the inverse of elements of SO and SE), the inverse of the $\boldsymbol{Ad}$ operator can be written:

$$\begin{aligned}\boldsymbol{\omega}^{B}_{A,B} &= \boldsymbol{Ad}_{\boldsymbol{R}^{T}_{A,B}}\boldsymbol{\omega}^{A}_{A,B} = \left[\boldsymbol{R}^{T}_{A,B}\right]\boldsymbol{\omega}^{A}_{A,B} \\ \boldsymbol{\xi}^{B}_{A,B} &= \boldsymbol{Ad}_{\boldsymbol{g}^{-1}_{A,B}}\boldsymbol{\xi}^{A}_{A,B} = \begin{bmatrix}\boldsymbol{R}^{T}_{A,B} & -\boldsymbol{R}^{T}_{A,B}\hat{\boldsymbol{p}}_{A,B} \\ \mathbf{0} & \boldsymbol{R}^{T}_{A,B}\end{bmatrix}\boldsymbol{\xi}^{A}_{A,B}\end{aligned} \tag{2.34}$$

A second adjoint can be defined on the Special Euclidean space. Following Park's notation[102], a second *adjoint* can be defined on the Lie Algebra $\mathfrak{se}$ instead of the Lie Group as in Equation 2.34 via the Lie Bracket:

$$ad_{\hat{\boldsymbol{\xi}}_1}(\hat{\boldsymbol{\xi}}_2) = \begin{bmatrix}\hat{\boldsymbol{\omega}}_1\hat{\boldsymbol{\omega}}_2\hat{\boldsymbol{\omega}}_1^{-1} & \hat{\boldsymbol{\omega}}_1\boldsymbol{v}_2 - \hat{\boldsymbol{\omega}}_2\boldsymbol{v}_1 \\ \mathbf{0} & 0\end{bmatrix} \tag{2.35}$$

This can be rewritten to form the matrix form of the adjoint which acts on the parametrised form of the Lie Algebra:

$$\boldsymbol{ad}_{\hat{\boldsymbol{\xi}}_1}\hat{\boldsymbol{\xi}}_2 = \begin{bmatrix}\hat{\boldsymbol{\omega}}_1 & \hat{\boldsymbol{v}}_1 \\ \mathbf{0} & \hat{\boldsymbol{\omega}}_1\end{bmatrix}\hat{\boldsymbol{\xi}}_2 \tag{2.36}$$

The Adjoint maps allow for the remapping of twists based on a transformation. This results in a highly versatile method for determining the velocities of a rigid-body object over time in both the spatial and body frames. This naturally extends to a method of expressing the Kinematics of a system.

2.3 Geometric Robotics- Kinematics

Kinematics is the study of the motions of a system. In the previous section, a number of key results were found for a simple single rigid-body motion. This section extends these results to multi-jointed serial chain structures. These structures can be the movements of a robotic arm, or the rotations of the ankle, knee, and hip during standing.

2.3.1 Positions

The first stage of Kinematic analysis is obtaining an expression for the positions of points on a rigid-body structure. Consider the system shown in Figure 2.3. This structure consists of a series of n joints, with the world frame located at the base, and the tool frame at the end of the chain. In this system, the positions of the prior joints will change the locations of joints located distally to it. To determine the configuration of the tool frame relative to the world frame ($\boldsymbol{g}_{W,T}(\boldsymbol{\theta})$), a representation of the intermediary segments is required.

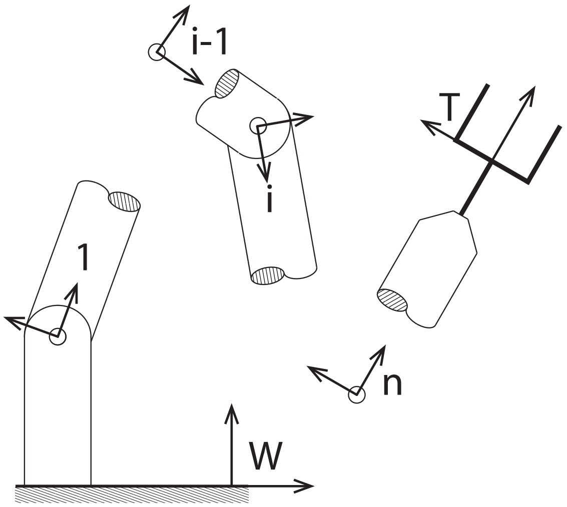

Figure 2.3: The segments of a serial chain structure. The world and tool frames are shown as W and T respectively. The frames of intermediary joints are shown, with the origin of the frame at the centre of the joint.

As shown from Equation 2.29, it is possible to describe a single rigid-body motion as:

$$\boldsymbol{g}_{A,B}(\theta_1) = e^{\hat{\boldsymbol{\xi}}^{A}_{A,B}\theta_1}\boldsymbol{g}_{A,B}(0)$$

This can be extended to a two joint system. Consider the two frames A and C which span two joints. The combined action of the two joints can be written as:

$$\begin{aligned}\boldsymbol{g}_{A,C}(\theta_1,\theta_2) &= \boldsymbol{g}_{A,B}(\theta_1)\boldsymbol{g}_{B,C}(\theta_2)\\ &= e^{\hat{\boldsymbol{\xi}}^{A}_{A,1}\theta_1}\boldsymbol{g}_{A,B}(0)e^{\hat{\boldsymbol{\xi}}^{B}_{B,2}\theta_2}\boldsymbol{g}_{B,C}(0)\end{aligned} \tag{2.37}$$

where the notation $\boldsymbol{\xi}^B_{B,2}\theta_2$ shows the second twist relative to frame B, as viewed in frame B. These twists are written in the initial configuration of the manipulator. Therefore $\boldsymbol{\xi}^B_{B,2}\theta_2$ can be rewritten to find the representation as viewed in frame A. This has the form:

$$\begin{aligned}\hat{\boldsymbol{\xi}}^A_{B,2} &= Ad_{\boldsymbol{g}_{A,B}(0)}(\hat{\boldsymbol{\xi}}^B_{B,2}) \\ &= \boldsymbol{g}_{A,B}(0)\hat{\boldsymbol{\xi}}^B_{B,2}\boldsymbol{g}^{-1}_{A,B}(0)\end{aligned} \tag{2.38}$$

This allows Equation 2.37 to be written as:

$$\begin{aligned}\boldsymbol{g}_{A,C}(\theta_1,\theta_2) &= e^{\hat{\boldsymbol{\xi}}^A_{A,1}\theta_1}\boldsymbol{g}_{A,B}(0)\boldsymbol{g}^{-1}_{A,B}(0)e^{\hat{\boldsymbol{\xi}}^A_{B,2}\theta_2}\boldsymbol{g}_{A,B}(0)\boldsymbol{g}_{B,C}(0) \\ &= e^{\hat{\boldsymbol{\xi}}^A_{A,1}\theta_1}e^{\hat{\boldsymbol{\xi}}^A_{B,2}\theta_2}\boldsymbol{g}_{A,C}(0)\end{aligned} \tag{2.39}$$

This can be generalised for a n-joint system resulting in the *Product of Exponentials* formula written in terms of the spatial twists:

$$\boldsymbol{g}_{W,T}(\boldsymbol{\theta}) = e^{\hat{\boldsymbol{\xi}}^W_{W,1}\theta_1}e^{\hat{\boldsymbol{\xi}}^W_{1,2}\theta_2}\dots e^{\hat{\boldsymbol{\xi}}^W_{n-1,n}\theta_n}\boldsymbol{g}_{W,T}(\mathbf{0}) \tag{2.40}$$

A similar expression for a serial chain system can be derived for based on the body twists. A body frame alternative to Equation 2.29 can be written:

$$\begin{aligned}\boldsymbol{g}_{A,B}(\theta_1) &= e^{\hat{\boldsymbol{\xi}}^A_{A,B}\theta_1}\boldsymbol{g}_{A,B}(0) \\ &= Ad_{\boldsymbol{g}_{A,B}(0)}\left(e^{\hat{\boldsymbol{\xi}}^B_{A,B}\theta_1}\right)\boldsymbol{g}_{A,B}(0) \\ &= \boldsymbol{g}_{A,B}(0)e^{\hat{\boldsymbol{\xi}}^B_{A,B}\theta_1}\end{aligned} \tag{2.41}$$

This results in the *Product of Exponentials* formula written in terms of the body twists[102][17]:

$$\boldsymbol{g}_{W,T}(\boldsymbol{\theta}) = \boldsymbol{g}_{W,T}(\mathbf{0})e^{\hat{\boldsymbol{\xi}}^T_{W,1}\theta_1}e^{\hat{\boldsymbol{\xi}}^T_{1,2}\theta_2}\dots e^{\hat{\boldsymbol{\xi}}^T_{n-1,n}\theta_n} \tag{2.42}$$

Equations 2.40 and 2.42 give representations for the configuration of any two frames in a serial chain system. From these expressions, it is possible to obtain expressions for the velocities of each of the rigid-bodies that comprise the system.

2.3.2 Velocities

Equations 2.30 and 2.31 introduced the spatial and body velocities of a single rigid-body. Given a system of two rigid bodies, the spatial velocity can be written as:

$$\begin{aligned}\hat{\boldsymbol{V}}^A_{A,C} &= \dot{\boldsymbol{g}}_{A,C}\boldsymbol{g}^{-1}_{A,C} \\ &= \left(\dot{\boldsymbol{g}}_{A,B}\boldsymbol{g}_{B,C} + \boldsymbol{g}_{A,B}\dot{\boldsymbol{g}}_{B,C}\right)\boldsymbol{g}^{-1}_{B,C}\boldsymbol{g}^{-1}_{A,B} \\ &= \dot{\boldsymbol{g}}_{A,B}\boldsymbol{g}^{-1}_{A,B} + \boldsymbol{g}_{A,B}\dot{\boldsymbol{g}}_{B,C}\boldsymbol{g}^{-1}_{B,C}\boldsymbol{g}^{-1}_{A,B} \\ &= \hat{\boldsymbol{V}}^A_{A,B} + Ad_{\boldsymbol{g}_{A,B}(\theta_1)}\left(\hat{\boldsymbol{V}}^B_{B,C}\right)\end{aligned} \tag{2.43}$$

and the body velocity as:

$$\begin{aligned}\hat{\boldsymbol{V}}_{A,C}^{C} &= \boldsymbol{g}_{A,C}^{-1}\dot{\boldsymbol{g}}_{A,C} \\ &= \boldsymbol{g}_{B,C}^{-1}\boldsymbol{g}_{A,B}^{-1}\left(\dot{\boldsymbol{g}}_{A,B}\boldsymbol{g}_{B,C} + \boldsymbol{g}_{A,B}\dot{\boldsymbol{g}}_{B,C}\right) \\ &= \boldsymbol{g}_{B,C}^{-1}\boldsymbol{g}_{A,B}^{-1}\dot{\boldsymbol{g}}_{A,B}\boldsymbol{g}_{B,C} + \boldsymbol{g}_{B,C}^{-1}\dot{\boldsymbol{g}}_{B,C} \\ &= Ad_{\boldsymbol{g}_{B,C}^{-1}(\theta_2)}\left(\hat{\boldsymbol{V}}_{A,B}^{B}\right) + \hat{\boldsymbol{V}}_{B,C}^{C}\end{aligned} \tag{2.44}$$

This provides two expressions for representing the body and spatial rigid-body velocities of a system.

These equations can be used recursively to construct the spatial and body Jacobians of the system. Starting from expressions for the parameterisations of twists written in the spatial or body initial conditions ($\boldsymbol{\xi}_{i-1,i}^{W}$ or $\boldsymbol{\xi}_{i-1,i}^{T}$ respectively), the re-mappings of these twists in the non-initial configuration are written as $\boldsymbol{\xi}_{i-1,i}^{\prime W}$ and $\boldsymbol{\xi}_{i-1,i}^{\prime T}$ where:

$$\boldsymbol{\xi}_{i-1,i}^{\prime W} = \boldsymbol{Ad}_{\left(e^{\hat{\boldsymbol{\xi}}_{W,1}^{W}\theta_1} e^{\hat{\boldsymbol{\xi}}_{1,2}^{W}\theta_2} \ldots e^{\hat{\boldsymbol{\xi}}_{i-2,i-1}^{W}\theta_{i-1}}\right)}\boldsymbol{\xi}_{i-1,i}^{W} \tag{2.45}$$

$$\boldsymbol{\xi}_{i-1,i}^{\prime T} = \boldsymbol{Ad}_{\left(e^{\hat{\boldsymbol{\xi}}_{i-1,i}^{W}\theta_i} e^{\hat{\boldsymbol{\xi}}_{i,i+1}^{W}\theta_{i+1}} \ldots e^{\hat{\boldsymbol{\xi}}_{n-1,n}^{W}\theta_n}\boldsymbol{g}_{W,T}(0)\right)^{-1}}\boldsymbol{\xi}_{i-1,i}^{W} \tag{2.46}$$

The resulting Jacobians are written:

$$\boldsymbol{J}_{W,T}^{W}(\boldsymbol{\theta}) = \begin{bmatrix}\boldsymbol{\xi}_{W,1}^{\prime W} & \boldsymbol{\xi}_{1,2}^{\prime W} & \ldots & \boldsymbol{\xi}_{n-1,n}^{\prime W}\end{bmatrix} \tag{2.47}$$

$$\boldsymbol{J}_{W,T}^{T}(\boldsymbol{\theta}) = \begin{bmatrix}\boldsymbol{\xi}_{W,1}^{\prime T} & \boldsymbol{\xi}_{1,2}^{\prime T} & \ldots & \boldsymbol{\xi}_{n-1,n}^{\prime T}\end{bmatrix} \tag{2.48}$$

2.3.3 Recursive Kinematic Formulation

Park[102] derives a recursive form for the body velocities and accelerations of a system. This recursive relationship is developed below, correcting an error in the formulation.

The body form for rigid-body motion is shown in Equation 2.42, and relates the initial configuration of two frames $\boldsymbol{g}_{i-1,i}(0)$, the body twist in local coordinates $\boldsymbol{\xi}_{i-1,i}^{i}$. Differentiating this relationship gives the expression:

$$\begin{gathered}\dot{\boldsymbol{g}}_{i-1,i}(\theta) = \boldsymbol{g}_{i-1,i}(0)e^{\hat{\boldsymbol{\xi}}_{i-1,i}^{i}\theta_i}\hat{\boldsymbol{\xi}}_{i-1,i}^{i}\dot{\theta}_i \\ \boldsymbol{g}_{i-1,i}^{-1}(\theta)\dot{\boldsymbol{g}}_{i-1,i}(\theta) = \hat{\boldsymbol{\xi}}_{i-1,i}^{i}\dot{\theta}_i\end{gathered} \tag{2.49}$$

The generalised body velocity of link i relative to the world frame can be written as:

$$\hat{\boldsymbol{V}}_{W,i}^{i} = \boldsymbol{g}_{W,i}^{-1}(\boldsymbol{\theta})\dot{\boldsymbol{g}}_{W,i}(\boldsymbol{\theta}) \tag{2.50}$$

This can be separated into a recursive step:

$$\begin{aligned} \hat{\boldsymbol{V}}^{i}_{W,i} &= (\boldsymbol{g}_{W,i-1}(\boldsymbol{\theta})\boldsymbol{g}_{i-1,i}(\theta_i))^{-1}\frac{d}{dt}(\boldsymbol{g}_{W,i-1}(\boldsymbol{\theta})\boldsymbol{g}_{i-1,i}(\theta_i)) \\ &= Ad_{\boldsymbol{g}^{-1}_{i-1,i}(\theta_i)}(\hat{\boldsymbol{V}}^{i-1}_{W,i-1}) + \hat{\boldsymbol{V}}^{i}_{i-1,i}\dot{\theta}_i \end{aligned} \tag{2.51}$$

This expression can be differentiated a second time to obtain an expression for the generalised acceleration $\dot{\hat{\boldsymbol{V}}}^{i}_{W,i}$:

$$\begin{aligned} \dot{\hat{\boldsymbol{V}}}^{i}_{W,i} &= \frac{d}{dt}\left(Ad_{\boldsymbol{g}^{-1}_{i-1,i}(\theta_i)}(\hat{\boldsymbol{V}}^{i-1}_{W,i-1})\right) + \hat{\boldsymbol{V}}^{i}_{i-1,i}\ddot{\theta}_i \\ &= \left(\dot{\boldsymbol{g}}^{-1}_{i-1,i}(\theta_i)\hat{\boldsymbol{V}}^{i-1}_{W,i-1}\boldsymbol{g}_{i-1,i}(\theta_i) + Ad_{\boldsymbol{g}^{-1}_{i-1,i}(\theta_i)}(\dot{\hat{\boldsymbol{V}}}^{i-1}_{W,i-1}) + \boldsymbol{g}^{-1}_{i-1,i}(\theta_i)\hat{\boldsymbol{V}}^{i-1}_{W,i-1}\dot{\boldsymbol{g}}_{i-1,i}(\theta_i)\right) + \hat{\boldsymbol{V}}^{i}_{i-1,i}\ddot{\theta}_i \\ &= \left[Ad_{\boldsymbol{g}^{-1}_{i-1,i}(\theta_i)}(\hat{\boldsymbol{V}}^{i-1}_{W,i-1}), \hat{\boldsymbol{\xi}}^{i}_{i-1,i}\dot{\theta}_i\right] + Ad_{\boldsymbol{g}^{-1}_{i-1,i}(\theta_i)}(\dot{\hat{\boldsymbol{V}}}^{i-1}_{W,i-1}) + \hat{\boldsymbol{V}}^{i}_{i-1,i}\ddot{\theta}_i \\ &= ad_{Ad_{\boldsymbol{g}^{-1}_{i-1,i}(\theta_i)}(\hat{\boldsymbol{V}}^{i-1}_{W,i-1})}\left(\hat{\boldsymbol{\xi}}^{i}_{i-1,i}\dot{\theta}_i\right) + Ad_{\boldsymbol{g}^{-1}_{i-1,i}(\theta_i)}(\dot{\hat{\boldsymbol{V}}}^{i-1}_{W,i-1}) + \hat{\boldsymbol{V}}^{i}_{i-1,i}\ddot{\theta}_i \end{aligned} \tag{2.52}$$

Therefore, given the knowledge of the generalised body velocities and accelerations for the previous links, the body velocity and acceleration for the current link can be expressed by the parameterised matrix expressions:

$$\begin{aligned} \boldsymbol{V}^{i}_{W,i} &= \boldsymbol{Ad}_{\boldsymbol{g}^{-1}_{i-1,i}(\theta_i)}\boldsymbol{V}^{i-1}_{W,i-1} + \boldsymbol{V}^{i}_{i-1,i}\dot{\theta}_i \\ \dot{\boldsymbol{V}}^{i}_{W,i} &= \boldsymbol{ad}_{\boldsymbol{Ad}_{\boldsymbol{g}^{-1}_{i-1,i}(\theta_i)}\boldsymbol{V}^{i-1}_{W,i-1}}\boldsymbol{\xi}^{i}_{i-1,i}\dot{\theta}_i + \boldsymbol{Ad}_{\boldsymbol{g}^{-1}_{i-1,i}(\theta_i)}(\dot{\boldsymbol{V}}^{i-1}_{W,i-1}) + \boldsymbol{V}^{i}_{i-1,i}\ddot{\theta}_i \end{aligned} \tag{2.53}$$

2.4 Geometric Robotics- Dynamics

Dynamics is the study of the relation between the forces acting on a system and the resulting motion. The linear forces and rotational torques are linked to the linear and rotational motions via the mass and inertia of the system[36].

2.4.1 Wrenches and Adjoints

The linear forces $\boldsymbol{F}_i$ and rotational torques $\boldsymbol{\tau}_i$ acting on a rigid body can be combined into a single vector $\boldsymbol{\Gamma}_i$ termed the wrench. While velocities in a system are related by the Adjoint, wrenches are related by the transpose of the Adjoint:

$$\boldsymbol{\Gamma}_i = \begin{bmatrix} \boldsymbol{F}_i \\ \boldsymbol{\tau}_i \end{bmatrix} = Ad^T_{\boldsymbol{g}_{i+1,i}(\theta_{i+1})} \boldsymbol{\Gamma}_{i+1} = Ad^T_{\boldsymbol{g}^{-1}_{i,i+1}(\theta_{i+1})} \boldsymbol{\Gamma}_{i+1} \tag{2.54}$$

2.4.2 Recursive Dynamic Formulation

Given a rigid-body i with mass m_i, located at the point with coordinates $\boldsymbol{r}_i$, and matrix of inertia $\boldsymbol{J}_i$ about the centre of mass, the corresponding wrench exerted at the origin is given by the expression[102]:

$$\boldsymbol{\Gamma}_i = \boldsymbol{I}_i \dot{\boldsymbol{V}}_i^i - \boldsymbol{ad}^T_{\hat{\mathbf{V}}_i} \boldsymbol{I}_i \boldsymbol{V}_i \tag{2.55}$$

where:

$$\boldsymbol{I}_i = \begin{bmatrix} m_i \mathbb{I} & -m_i \hat{\boldsymbol{r}}_i \\ m_i \hat{\boldsymbol{r}}_i & \boldsymbol{J}_i - m_i \hat{\boldsymbol{r}}_i^2 \end{bmatrix} \tag{2.56}$$

Combining this relation with Equation 2.54 gives an expression for the wrench acting at the origin of the joint i given in the i frame:

$$\boldsymbol{\Gamma}_i = Ad^T_{\boldsymbol{g}^{-1}_{i,i+1}(\theta_{i+1})} \boldsymbol{\Gamma}_{i+1} + \boldsymbol{I}_i \dot{\boldsymbol{V}}_i^i - \boldsymbol{ad}^T_{\hat{\mathbf{V}}_i} \boldsymbol{I}_i \boldsymbol{V}_i + \boldsymbol{\Gamma}_{i,E} \tag{2.57}$$

where $\boldsymbol{\Gamma}_{i,E}$ is the external wrench acting on the rigid body. Equation 2.57 is the backwards dynamics recursion. After determining the velocities and the accelerations of each link, and measuring the external wrenches acting on the object, the wrench acting at the origin of each frame can be computed from distal to proximal.

Part I

Human Modelling

Chapter 3

Kinematic Modelling

This chapter outlines methods for creating a representative kinematic model of an individual. Building on the mathematical framework introduced in Section 2, this chapter extends these methods to the biomechanical modelling problem. Section 3.1 introduces the standard state of the art for kinematic modelling. Section 3.2 develops a robust kinematic recovery framework. These individualised kinematic models are then used in the development of an individualised dynamic model in Chapter 4.

3.1 State of the Art

Biological motion has been formally studied over the course of centuries, with some of the first work being developed by da Vinci. The connection between anatomical structure and corresponding motions has been studied through a number of methods. This section outlines the state of the art in Kinematic modelling[22][93][136][146]. Section 3.1.1 outlines the methods that can be used to locate joints and track range of motion. A number of these methods track points on the body that are then used to infer joint state and location (Sections 3.1.2, 3.1.3). The challenges faced by existing methods are outlined in Section 3.1.4, and the improvements from the presented work shown in Section 3.1.5.

3.1.1 Methods

The methods used to quantify human motion will be separated into two categories: direct and indirect. Direct methods attach a measurement device (such as a goniometer or accelerometer) directly to the subject. In contrast, indirect methods typically use optical methods to track an individual's motions potentially without any alterations made to the individual.

3.1.1.1 Direct Methods

One of the most common clinical methods for measuring an individual's range of motion is through direct goniometry. Traditionally this is a purely mechanical device similar to a protractor that is used to measure the angle between two limb segments. This measure is one of the most frequently used clinical measures for quantifying range of motion due to the low training burden and affordability. While being commonly used, goniometry is frequently limited by the time required to take the measurements. These devices have been instrumented with encoders to help expedite this process, however this does not reduce the time required to correctly pose the subject. The variability and reliability of these methods is questionable, with a number of papers suggesting that these methods are not suitable for tracking a patient over time due to significant inter- and intra- clinician variability in goniometric measurements and variability with the type of goniometer used[14][45]. These effects were found to be compounded during longitudinal studies, making their clinical reliability as a quantitative measure questionable[86]. Furthermore, only the relative angles between surface landmarks are tracked in a single plane, making the extension to more complicated joint movements challenging[50].

X-rays, and X-ray fluoroscopy can also be used to find the location and rotation of a joint[129]. By taking a number of X-rays in sequence, it is possible to directly track the motion of the underlying skeleton[30]. These methods are extremely useful for measuring the true position of the limb. The use of X-rays is an *invasive* procedure due to the use of ionising radiation.

The accelerations and rotational velocities of a limb can also be measured directly through the use of wearable Inertial Measurement Units (IMUs). While these sensors are relatively easy to use and affordable, their use for estimation of joint angles and positions is limited as these are estimated through integration of the acceleration and velocity measurements. As a direct measure of acceleration, their use is limited due to their mass and the need for accurate attachment. IMUs will measure the acceleration component of the device directly, not the limb segment. The conversion from the IMU acceleration to the limb acceleration requires knowledge of the rigid-body transform between the limb coordinate system and that of the IMU axes. Any relative motion between the device and the bone due to a combination of soft tissue motion (skin etc.) and attachment method will reduce the reliability of the IMU tracking system[72].

3.1.1.2 Indirect Methods

While the use of IMUs as a direct sensor is limited, there are a number of methods for extending them to act as an indirect measurement device for joint angles. Based on the potential for noise in the sensor readings, there has been substantial work on developing methods to fuse the accelerometer, gyroscope, and magnetometer data into a smoothed estimate of joint state[89]. One of the frequently used methods is a non-linear *Kalman Filter* in either the *Extended* (EKF)[16] or *Unscented* (UKF)[120] forms. These methods have been shown to provide improved estimates of joint angle compared to using the sensors independently though gradient decent methods have also been shown to provide similar improvements under less computational load[77].

Magnetometers can also be used to estimate the position of key points on the body using a structured magnetic field. The subject wears a number of small sensors that estimate their location by measuring the magnetic flux. These devices have been shown to provide high resolution measurements of position, but can suffer from errors near metallic or magnetic objects.

There are a number of optical methods for motion capture, which can be separated into markered and markerless categories. Markered motion capture requires the user to wear a number of markers on their body. These markers can be active: emitting light at a known frequency[104], or passive: retro-reflecting light back to the camera[99]. While these methods often present similar spatial accuracies, they are differentiated through the method of sensing. Active markers are automatically labelled allowing the exact position of a specific marker to be tracked over time. Passive markers are unlabelled and need to be manually tracked in post. The benefit of passive markers is the lightweight, non-powered nature of the markers. In contrast, active markers need to be powered resulting in a larger, heavier form factor.

There are a number of markerless methods that can be used to estimate pose. These methods can build 2D/3D silhouettes using a standard camera, or by adding depth sensing using a projected Infra-Red grid/through time of flight. These silhouettes can then be used to estimate pose through machine learning methods, comparing the observed silhouette to a database, or by fitting a shape model to the system[93].

3.1.2 Recovering Joint State

While a number of these methods extract joint angles directly, the majority of motion capture methods return the 3D location of markers or rigid-body position and rotation for the segment. In these cases it is necessary to convert these point and rigid-body measurements into a set of representative angles.

Traditionally, this is done by assigning markers points to specific body landmarks, then measuring the angles of these markers relative to the world frame. These marker locations are subject to variation depending on lab and study protocol, making clarification of marker location necessary.

A more mathematical approach is to assign sets of 3D points to lie on a rigid-body, then determining the position and orientation for this rigid body at each instance in time. This allows for the generation of a time series of homogeneous matrices $\boldsymbol{g}_{W,i}(t)$ for each rigid-body segment. The relative transformation between these two frames can then be computed for that instant via $\boldsymbol{g}_{W,i}^{-1}\boldsymbol{g}_{W,j}$. The resulting rotation matrix can then be decomposed into an appropriate angle convention[89].

One problem that arises with these techniques is a marker *dropping* or *swapping* during a trial. Marker drop can result from occlusion, resulting in a marker disappearing during a sample. Marker swap can occur in the case of passive motion capture when two passive markers move close to each other. As passive markers are indistinguishable from each other, it is impossible to determine if two markers are moving past each other, or making contact then recoiling.

In these cases, the recovery of joint state may be complicated by an insufficient number of markers being viewable in a frame for estimation of the instantaneous rigid-body transform. A common method for overcoming this issue is by fitting a smoothing spline to the missing data. While this does allow for the recovery of a rigid-body transform, there may be substantial error as the sections of motion capture that may be missing could occur during sections of rapidly changing movement[37]. Marker position can be estimated using marker prediction methods at the action[37], segment[54] and marker[141] levels. These methods will be used as inspiration for the presented work.

3.1.2.1 State Derivatives

While the majority of methods recover a joint angle, the joint derivatives are often needed, particularly in the case of dynamic modelling. Typically these are recovered through repeated low pass filtering the data and numeric differentiation steps. While this method is used extensively, there is relatively little investigation on the correct cut-off frequency to ensure validity of the angular derivatives, with analysis being performed by Pezzack[103] and Sinclair[115]. From these studies it was found that filtering-differentiation methods out performed Chebyshev polynomial fitting, and finite differencing alone. The choice of cut-off frequency was found to have a substantial effect on the recovered state derivatives.

Another challenge that is faced in the recovery of the state dynamics, is the requirement that the state derivatives are *dynamically consistent*, i.e. that the state and the derivatives are coupled dynamically. In the methods listed above, the dynamic consistency is not assured, potentially leading to estimated joint states that are not representative of the system's evolution.

The recovered joint state may also be infeasible, returning motions that are outside the system's range of motion. These artefacts can arise through motion capture drop, motion of markers on the skin, or through the unconstrained transform recovery. These errors can be reduced through the use of a representative kinematic model. These kinematic models can provide rigid-body constraints to the measurements, ensuring that the motions are *kinematically consistent*. The use of kinematic models to assist in the joint recovery process has been shown to improve accuracy and repeatability during the recovery process[75][109][120].

3.1.3 Extracting Joint Location

The use of kinematic models to aid the kinematic recovery process is limited by the accuracy of the model parameters such as joint locations. The length of the limbs and the locations of each joint can vary with the individual, particularly in the case of patient interventions. Therefore a method is required to estimate the locations of the joint centres.

There are a number of methods to estimate the kinematic parameters of an individual. The most direct method is to use imaging based methods such as X-ray fluoroscopy (as mentioned in Section 3.1.1.1), however this method is limited by the invasiveness of the procedure. The alternatives to these methods can be divided into allometric scaling and functional methods.

3.1.3.1 Allometric Scaling

Allometric scaling is heavily used in the biomechanics community. By measuring the locations of easily located anatomical landmarks, statements are made about the underlying anatomy of the subject. These methods extended from general principles where joint centres are estimated from surface landmarks[26][38][63][126][139][140] or from the overall height of the subject[136]. These methods have been shown to provide joint location accuracies of approximately 1-2cm for the hip[10][66][96].

While these methods are widely used, there are known issues with locating certain joints (such as the hip), and significant variations due to sex and ethnicity. To overcome these limitations, the *functional centre* of the joint can be estimated by observing the motions of the individual.

3.1.3.2 Functional Methods

Building on the kinematic modelling and state recovery methods, joint centres can be estimated by examining the motions of the limb[33].

The computation of the matrix $\boldsymbol{g}_{W,i}^{-1}\boldsymbol{g}_{W,j}$ can be used to determine the instantaneous centre between two rigid body frames which have been defined apriori[89][111]. There are a number of different formulations for determining the joint centre using this approach. These methods are often separated into one and two sided methods depending on whether one or both segments are moving at that instant[53][111][116][138]. These methods have shown accuracies of approximately 2mm for the joint centre, and are robust to noise in cases where the joint is sufficiently moved through its range of motion[33][105].

In addition to these methods are a number of sphere fitting methods that attempt to find the best fit sphere given markers on the limb[19][28][42][41][48][80][98]. While there are a number of variations in these methods, they are typically one sided which can present a problem in practice. These functional methods have been shown to be accurate for the test cases, but variations can occur based on the formulation chosen, and the actions used[10][73][105][114].

3.1.4 Challenges

From this prior work, it is clear that there are a number of techniques that offer the ability to create a representative kinematic model for an individual which can surpass the methods currently being used clinically. The biggest challenge is developing a framework that allows for the translation of these techniques in a manner that does not result in a retraining burden for the healthcare provider, and a cost/time burden on the patient/clinician team. The existing state of the art from the biomechanics community requires precise marker placement, manual post-processing, and adherence to exact protocols to generate a reliable human model and state estimate. These high requirements limit the clinical deployment of the existing state of the art.

3.1.5 Novelty

This chapter will introduce a method for developing a kinematic model for an individual that is aimed at clinical deployment. The method adopts a physics-based approach, extracting model features in a structured manner. This allows for the recovery of parameters that are physically meaningful allowing for tracking over time and estimation of recovery and intervention efficacy.

The presented method generates a best fit serial chain model from the provided motion capture data without making assumptions on the location of joints, the length of limb segments, or abilities of the individual. This data-driven approach allows for recovery of a model that represents the individual's actions, reducing the effect of investigator biases, and variation.

The actions being analysed are selected based on simplicity and on standardised clinical tests such as the five-times sit-to-stand test. This reduces the training burden on clinicians and is expected to improve protocol adherence during out-of-clinic deployment.

Setup time is minimised, with conventional motion-capture calibrations such as T-pose and sequential joint excitation being avoided. This reduces patient and clinician burden by reducing the amount of time required to calibrate the experimental setup.

Markers are automatically assigned to segments based on their observed trajectories, allowing for errors in marker placement. Furthermore markers are not constrained to lie at specific points on the individual enabling flexibility in the protocol setup.

The framework is robust to marker *drop* filling gaps in missing markers data, including cases where less than three markers are known for a segment. This is achieved through a dynamic filtering method which also ensures dynamic consistency in the angular state and its derivatives.

3.2 Kinematic Recovery Framework

This section outlines the mathematics behind the proposed skeletonisation process. An overview of the mathematical intuition is provided in Section 3.2.1 with more details provided in Sections 3.2.3 to 3.2.6. The applications of this algorithm to robotic and human modelling are shown in Chapters 5 and 6 respectively.

This algorithm simplifies the Kinematic recovery process to the recovery of planar, serial chain motions. This simplification allows for the development and testing of the complete kinematic and dynamic recovery process on a structured system, allowing for analysis of the recovered model. The extension to full 3D structures is relatively straightforward, only requiring the circle fitting algorithm (Section 3.2.4) to be changed to a sphere fitting algorithm. However the resulting dynamic model will dramatically increase in complexity. Therefore this work focuses on the planar case.

3.2.1 Overview

Returning to the preliminaries on rigid-body motion, the relative motion between two adjacent links in a serial chain structure can be described by the equation:

$$\begin{bmatrix} \boldsymbol{q}_{j-1} \\ 1 \end{bmatrix} = \boldsymbol{g}_{j-1,j}(\theta_j) \begin{bmatrix} \boldsymbol{q}_j \\ 1 \end{bmatrix} = \begin{bmatrix} \boldsymbol{R}_{j-1,j}(\theta_j) & \boldsymbol{p}_{j-1,j} \\ \boldsymbol{0} & 1 \end{bmatrix} \begin{bmatrix} \boldsymbol{q}_j \\ 1 \end{bmatrix} \tag{3.1}$$

where $\boldsymbol{g}_{j-1,j}$ is a rotation parametrised by $\boldsymbol{R}_{j-1,j}(\theta_j)$ at the point with the local coordinates $\boldsymbol{p}_{j-1,j}$.

In a serial chain structure, the motions of points on the j^{th} link will depend on the angles $\{\theta_1 \dots \theta_j\}$

$$\begin{bmatrix} \boldsymbol{q}_{W,j}(t) \\ 1 \end{bmatrix} = [\boldsymbol{g}_{W,1}(\theta_1(t)), \dots, \boldsymbol{g}_{j-1,j}(\theta_j(t))] \begin{bmatrix} \boldsymbol{q}_j \\ 1 \end{bmatrix} = \boldsymbol{g}_{W,j}(\boldsymbol{\theta}_{1,\dots,j}(t)) \begin{bmatrix} \boldsymbol{q}_j \\ 1 \end{bmatrix} \tag{3.2}$$

where the local coordinates of point $\boldsymbol{q}_j$ do not vary with time. Motion capture systems return marker trajectories in the world frame $\boldsymbol{q}_{W,j}(t)$ which may appear as elaborate arcs in space. However the motions represented by Equation 3.1 are that of a point moving about a sphere. Therefore Equation 3.2 can be separated to:

$$\begin{bmatrix} \boldsymbol{q}_{W,j}(t) \\ 1 \end{bmatrix} = \boldsymbol{g}_{W,j-1}(\boldsymbol{\theta}_{1,\dots,j-1}(t))\boldsymbol{g}_{j-1,j}(\theta_j(t)) \begin{bmatrix} \boldsymbol{q}_j \\ 1 \end{bmatrix} \tag{3.3}$$

$$\boldsymbol{g}^{-1}_{W,j-1}(\boldsymbol{\theta}_{1,\dots,j-1}(t)) \begin{bmatrix} \boldsymbol{q}_{W,j}(t) \\ 1 \end{bmatrix} = \boldsymbol{g}_{j-1,j}(\theta_j(t)) \begin{bmatrix} \boldsymbol{q}_j \\ 1 \end{bmatrix} \tag{3.4}$$

$$\begin{bmatrix} \boldsymbol{q}_{j-1,j}(t) \\ 1 \end{bmatrix} = \boldsymbol{g}_{j-1,j}(\theta_j(t)) \begin{bmatrix} \boldsymbol{q}_j \\ 1 \end{bmatrix} \tag{3.5}$$

where Equation 3.5 is of the same form as Equation 3.1. This equation shows that in the relative coordinate system, the motions of markers will be reduced into motion about a sphere. Therefore if the rigid-body motions of the prior $j-1$ joints are known $(\boldsymbol{g}_{W,j-1}(\boldsymbol{\theta}_{1,\ldots,j-1}(t)))$, then the centre of rotation $(\boldsymbol{p}_{j-1,j})$, local coordinates of the markers on segment j $(\boldsymbol{q}_j)$ and the relative rotation matrix $(\boldsymbol{R}_{j-1,j}(\theta_j(t)))$ can be found from the world trajectories $(\boldsymbol{q}_{W,j})$ via:

$$\boldsymbol{g}^{-1}_{W,j-1}(\boldsymbol{\theta}_{1,\ldots,j-1}(t))\begin{bmatrix}\boldsymbol{q}_{W,j}(t)\\ 1\end{bmatrix} = \begin{bmatrix}\boldsymbol{R}_{j-1,j}(\theta_j(t)) & \boldsymbol{p}_{j-1,j}\\ \boldsymbol{0} & 1\end{bmatrix}\begin{bmatrix}\boldsymbol{q}_j\\ 1\end{bmatrix} \tag{3.6}$$

Equation 3.6 therefore defines a recursive algorithm. Starting at a base link W, motions of the next link 1 can be identified as simple rotations. Therefore by finding points that move in a sphere relative to link W, the markers on segment 1, the relative position of the centre of rotation $\boldsymbol{p}_{W,1}$ to the origin of the previous frame, and the local coordinates of the points on frame 1 $(\boldsymbol{q}_1)$ can be determined. After this identification, inverse kinematics can be used to recover the corresponding joint trajectory $\theta_1(t)$. This defines the time-series $\boldsymbol{g}_{W,1}(t)$. This process is then repeated, identifying the markers on subsequent segments.

This process of circle fitting, parameter identification, and state recovery is outlined in Sections 3.2.3 to 3.2.6.

3.2.2 Assumptions

The following assumptions will be made in order to simplify the kinematic recovery process.

A1 The system and actions to be recovered can be reduced to motion on a plane.

A2 The system can be represented as a rigid-body serial chain.

A3 Marker swap does not occur.

A4 The observed actions are sufficiently kinematically exciting.

Assumption **A1** simplifies the kinematic and dynamic recovery process, while **A2** allows for the use of the outlined rigid-body recovery method. Assumption **A3** allows for circle fitting to take place over full trajectories, making use of active motion capture or similar unique marker methods. Assumption **A4** states that the joints in the system are moved sufficiently in their range of motion to allow for recovery.

3.2.3 Planarisation

Under assumption **A1** the trajectories of markers in 3D $(\tilde{\boldsymbol{q}}(t))$ need to be *flattened* onto a representative plane $(\boldsymbol{q}(t))$. In this work, the plane of action is assumed to be perpendicular to the ground. This best-fit plane can therefore be found by projecting all of the trajectories onto the ground plane, then finding the line of action.

Consider the 3D trajectories $\tilde{\boldsymbol{q}}(t)$. These trajectories can be flattened onto the ground (X,Y) plane, and centred to the origin via the transformation:

$$\breve{\boldsymbol{q}}_i(t) = \begin{bmatrix} \breve{\boldsymbol{q}}_{x,i}(t) \\ \breve{\boldsymbol{q}}_{y,i}(t) \end{bmatrix} = \begin{bmatrix} 1 & 0 & 0 \\ 0 & 1 & 0 \end{bmatrix} \begin{bmatrix} \tilde{\boldsymbol{q}}_{x,i}(t) \\ \tilde{\boldsymbol{q}}_{y,i}(t) \\ \tilde{\boldsymbol{q}}_{z,i}(t) \end{bmatrix} - \begin{bmatrix} \bar{\boldsymbol{q}}_{x,i} \\ \bar{\boldsymbol{q}}_{y,i} \end{bmatrix} \tag{3.7}$$

where $\bar{\boldsymbol{q}}_{x,i}$ and $\bar{\boldsymbol{q}}_{y,i}$ are the mean positions of marker i. Given the n marker trajectories $\breve{\boldsymbol{q}}_i(t)$ for $i \in [1, n]$, the angle between the laboratory frame and the plane of movement can be computed through the arctan of the x, y components. This defines the angle that the data needs to be rotated about to flatten the motion onto a plane. These flattened trajectories in the laboratory world frame are denoted $\boldsymbol{q}_{W,i}(t)$.

3.2.4 Circle Fitting

The circle fitting process is the first step of the recursive kinematic recovery process. It is initialised with a set of marker trajectories $\mathcal{Q}$ that have been flattened onto a plane. Each marker trajectory $q_{W,i}(t) \in \mathcal{Q}$ is known to track a single marker over time as there is no marker-swap (assumption **A3**). Therefore markers can be allocated to a rigid-body segment by finding circles in the non-assigned marker trajectories.

Consider set $\mathcal{Q}$ of all n markers, and $\mathcal{Q}_A \subset \mathcal{Q}$ the subset of markers that have already been allocated to a segment. This leaves set $\mathcal{Q}_C$, the set of candidate markers that will be used for the circle fitting process for this iteration.

The circle fitting process requires knowledge of the prior rigid-body transformations for the prior links. For iteration i, it is assumed that $\boldsymbol{g}_{W,i-1}(\boldsymbol{\theta}_{1,\dots,i-1})$ are known. In the special case of the first iteration, this is the matrix $\boldsymbol{g}_{W,W}$: the 4×4 identity matrix.

Given the set of candidate markers $\mathcal{Q}_C$, and the rigid-body transforms $\boldsymbol{g}_{W,i-1}(\boldsymbol{\theta}_{1,\dots,i-1})$ the centre $\boldsymbol{p}_j$ and radius $\boldsymbol{r}_j$ can be found for each candidate marker trajectory $\boldsymbol{q}_j(t)$ via the optimisation problem:

$$\min_{\boldsymbol{p}_j, \boldsymbol{r}_j} \left\| \|\boldsymbol{q}_{i-1,j}(t) - \boldsymbol{p}_j\|_2^2 - \boldsymbol{r}_j \mathbb{1} \right\|_2^2 \tag{3.8}$$

where $\mathbb{1}$ is a vector of ones, and $\boldsymbol{q}_{i-1,j}(t)$ is the trajectory of candidate marker j after being transformed from the world frame coordinates $\boldsymbol{q}_{W,j}$ to the $i-1^{th}$ frame coordinates $\boldsymbol{q}_{W,i-1}$ via:

$$\boldsymbol{q}_{i-1,j}(t) = \boldsymbol{g}_{W,i-1}^{-1}(\boldsymbol{\theta}_{1,\dots,i-1}) \boldsymbol{q}_{W,j}(t) \tag{3.9}$$

The residuals of this minimisation acts as an indicator of how circular the trajectories of a marker j in the candidate marker set $\mathcal{Q}_C$ are for the observed actions. Markers with low residuals are kept in the set $\mathcal{Q}_C$, while markers that do not appear to move in a circle are removed. Markers remaining in $\mathcal{Q}_C$ have been found to be move along circular paths, allowing for a common centre to be recovered.

3.2.5 Parameter Identification

Given the set of candidate markers $\mathcal{Q}_C$, which have been found to rotate through circular paths when viewed in $i-1$ frame, the next step is to determine the common centre of rotation, and the local coordinates of the marker.

Consider the k candidate markers in set $\mathcal{Q}_C$. At a single sample s, these markers have the planar coordinates:

$$\boldsymbol{q}_{i-1}(s) = \begin{bmatrix}\boldsymbol{q}_{i-1,1}(s) & \dots & \boldsymbol{q}_{i-1,j}(s) & \dots & \boldsymbol{q}_{i-1,k}(s)\end{bmatrix} \in \mathbb{R}^{2\times k} \tag{3.10}$$

The fixed local coordinates of marker j can be written in polar coordinates as a radius r_j and an angle ϕ_j:

$$\boldsymbol{q}_j = \begin{bmatrix}\boldsymbol{q}_{x,j} \\ \boldsymbol{q}_{y,j}\end{bmatrix} = \begin{bmatrix}-r_j sin(\phi_j) \\ r_j cos(\phi_j)\end{bmatrix} \tag{3.11}$$

These local coordinates can be concatenated into the homogeneous matrix:

$$\boldsymbol{q}_i = \begin{bmatrix}\begin{bmatrix}\boldsymbol{q}_1 \\ 1\end{bmatrix} & \dots \begin{bmatrix}\boldsymbol{q}_j \\ 1\end{bmatrix} & \dots \begin{bmatrix}\boldsymbol{q}_k \\ 1\end{bmatrix}\end{bmatrix} \in \mathbb{R}^{3\times k} \tag{3.12}$$

The expected coordinates of the candidate markers at sample s as seen in the $i-1$ frame are therefore related via the expression:

$$\boldsymbol{q}_{i-1}(s) = \begin{bmatrix}\boldsymbol{R}_{i-1,i}(\theta(s)) & \boldsymbol{p}_{i-1,i}\end{bmatrix} \boldsymbol{q}_i \tag{3.13}$$

This expression can be extended for the entire data set. As the local marker coordinates $\boldsymbol{q}_i$ do not change, and the coordinates of the markers in the $i-1$ frame are parametrised only by the angle θ_i, the expected coordinates of the markers for m samples can be written:

$$\begin{bmatrix}\boldsymbol{q}_{i-1}(1) \\ \vdots \\ \boldsymbol{q}_{i-1}(s) \\ \vdots \\ \boldsymbol{q}_{i-1}(m)\end{bmatrix} = \begin{bmatrix}\begin{bmatrix}\boldsymbol{R}_{i-1,i}(\theta(1)) & \boldsymbol{p}_{i-1,i}\end{bmatrix} \\ \vdots \\ \begin{bmatrix}\boldsymbol{R}_{i-1,i}(\theta(s)) & \boldsymbol{p}_{i-1,i}\end{bmatrix} \\ \vdots \\ \begin{bmatrix}\boldsymbol{R}_{i-1,i}(\theta(m)) & \boldsymbol{p}_{i-1,i}\end{bmatrix}\end{bmatrix} \boldsymbol{q}_i = \boldsymbol{G}_{i-1,i}(\boldsymbol{\theta}_i, \boldsymbol{p}_{i-1,i})\boldsymbol{q}_i \tag{3.14}$$

By computing the error between the expected marker positions $\boldsymbol{G}_{i-1,i}(\boldsymbol{\theta}_i, \boldsymbol{p}_{i-1,i})\boldsymbol{q}_i$ and the transformed measurements $\boldsymbol{Q}_{i,j}$, it is possible to determine the local marker positions $\boldsymbol{q}_i$. The rotation component is ill-posed however as both ϕ_j and $\theta(s)$ are unknown. To make this problem tractable, the angles $\boldsymbol{\phi}$ are also minimised, effectively aligning the Y-axis of the i^{th} frame to lie midway between the observed markers.

In cases where markers are known to be located near joints, the error between these *auxiliary* markers $\boldsymbol{p}_A$ and the recovered joint position can also be minimised. Forming a matrix of these markers allows the error in the joint position to be written:

$$\boldsymbol{\epsilon}_A = \begin{bmatrix} \boldsymbol{p}_A(1) \\ \vdots \\ \boldsymbol{p}_A(s) \\ \vdots \\ \boldsymbol{p}_A(m) \end{bmatrix} - \begin{bmatrix} [\mathbb{I}_2] \\ \vdots \\ [\mathbb{I}_2] \\ \vdots \\ [\mathbb{I}_2] \end{bmatrix} \boldsymbol{p}_{i-1,i} \tag{3.15}$$

This forms the optimisation problem:

$$\min_{\boldsymbol{\theta}_i, \boldsymbol{p}_{i-1,i} \boldsymbol{q}_i} \left\| \left\| \boldsymbol{Q}_{i,j} - \boldsymbol{G}_{i-1,i}(\boldsymbol{\theta}_i, \boldsymbol{p}_{i-1,i}) \boldsymbol{q}_i \right\|_2^2 + \lambda_\phi \left\| \boldsymbol{\phi} \right\|_2^2 + \lambda_A \left\| \boldsymbol{\epsilon}_A \right\|_2^2 \right\|_2^2 \tag{3.16}$$

where λ_ϕ and λ_A are weighting terms for the optimisation. Examining the columns of the first term allows for the detection of markers that, while moving along a circular path, are not on the same rigid body as the rest. These markers can be removed from the candidate marker set. Solving this optimisation problem recovers the joint centre $\boldsymbol{p}_{i-1,i}$, the local marker coordinates $\boldsymbol{q}_i$, and a set of joint angles $\boldsymbol{\theta}_i$.

3.2.6 State Recovery

While the parameter identification step will return estimates of the joint state $\boldsymbol{\theta}_i$, these joint angles are not ideal representations of joint state. The parameter identification step does not consider the dynamics of the system, and may result in joint angles that suddenly jump between samples. The parameter identification step also requires all the markers to be visible during the optimisation, a constraint that may not hold true in experiments.

This section introduces a method for obtaining a dynamically consistent estimate for the angular position and its derivatives. The method is a robust rigid-body method that is tolerant of marker drop. By using a template dynamic model, the joint states can be coupled together ensuring dynamic coherency. As the exact dynamic model of the system is not known a priori, the system is modelled as a random walk process with noise entering in the snap term. By modelling the perturbation in the high order derivative, the recovered state up to the acceleration term will be smoothed. The discrete time form of this dynamic system can be written:

$$\begin{bmatrix} \theta \\ \dot{\theta} \\ \ddot{\theta} \\ \dddot{\theta} \end{bmatrix}_{k+1} = \begin{bmatrix} 1 & \frac{\delta t}{1!} & \frac{(\delta t)^2}{2!} & \frac{(\delta t)^3}{3!} \\ 0 & 1 & \frac{(\delta t)}{1!} & \frac{(\delta t)^2}{2!} \\ 0 & 0 & 1 & \frac{(\delta t)}{1!} \\ 0 & 0 & 0 & 1 \end{bmatrix} \begin{bmatrix} \theta \\ \dot{\theta} \\ \ddot{\theta} \\ \dddot{\theta} \end{bmatrix}_{k} + \begin{bmatrix} \frac{(\delta t)^4}{4!} \\ \frac{(\delta t)^3}{3!} \\ \frac{(\delta t)^2}{2!} \\ \frac{(\delta t)}{1!} \end{bmatrix} \boldsymbol{v}_k \tag{3.17}$$

where δt is the incremental time step, and $\boldsymbol{v}_k$ is the process noise.

While the exact form of the process model is not know, the *observation* model that links the system state to the observed sensor values is known. This is the forward kinematic map f_{FK} and can be formed from the kinematic model that has been recovered for the i segments.

From the parameter identification process, the rigid body transform representing the joints 1 to i have been recovered, as have the local marker coordinates for each link $\boldsymbol{q}_1, \ldots, \boldsymbol{q}_i$. This gives expressions for expected coordinates of all assigned markers in the world frame as a function of the joint state $\boldsymbol{\theta}$:

$$\begin{bmatrix} \boldsymbol{q}_{W,1} \\ \vdots \\ \boldsymbol{q}_{W,i} \end{bmatrix} = \begin{bmatrix} \boldsymbol{g}_{W,1}(\theta_1)\boldsymbol{q}_1 + \boldsymbol{n} \\ \vdots \\ \boldsymbol{g}_{W,i}(\theta_1 \ldots \theta_i)\boldsymbol{q}_i + \boldsymbol{n} \end{bmatrix} \tag{3.18}$$

where $\boldsymbol{n}$ is the associated noise in the measurements. Equation 3.18 is the observation equation for the system and gives the mapping from the state space to the observations.

Given models for both the process and observation of the system (Equations 3.17 and 3.18), an Unscented Kalman Filter (UKF) can be used to rectify potential mismatches between the observations and the expected state[62][131].

The UKF is supplemented by a marker prediction step. In the event a marker is missing from a particular sample, the marker position is estimated from the previous state estimate using Equation 3.18. This uses the state at step $s - 1$ ($\boldsymbol{\theta}_{s-1}$) to predict where the markers should be at sample s. These marker estimates are used to fill in the gaps in the missing state vector at sample s. As these are estimates, not true measurements, the corresponding marker noise term $\boldsymbol{n}$ is increased for the markers with estimated locations. This ensures that the UKF can run at each step, while capturing the uncertainty in the estimation process.

The UKF is run both forwards and backwards in time. This reduces the effect of phase distortion, and allows for the state to be recovered for the entire time series. This recovers the angular state and its derivatives for all samples for joints 1 to i. This fully recovers the kinematic model and the states for the first i joints. The recovery process can now be repeated for the $i + 1$ link. The full kinematic recovery process is summarised in Figure 3.1.

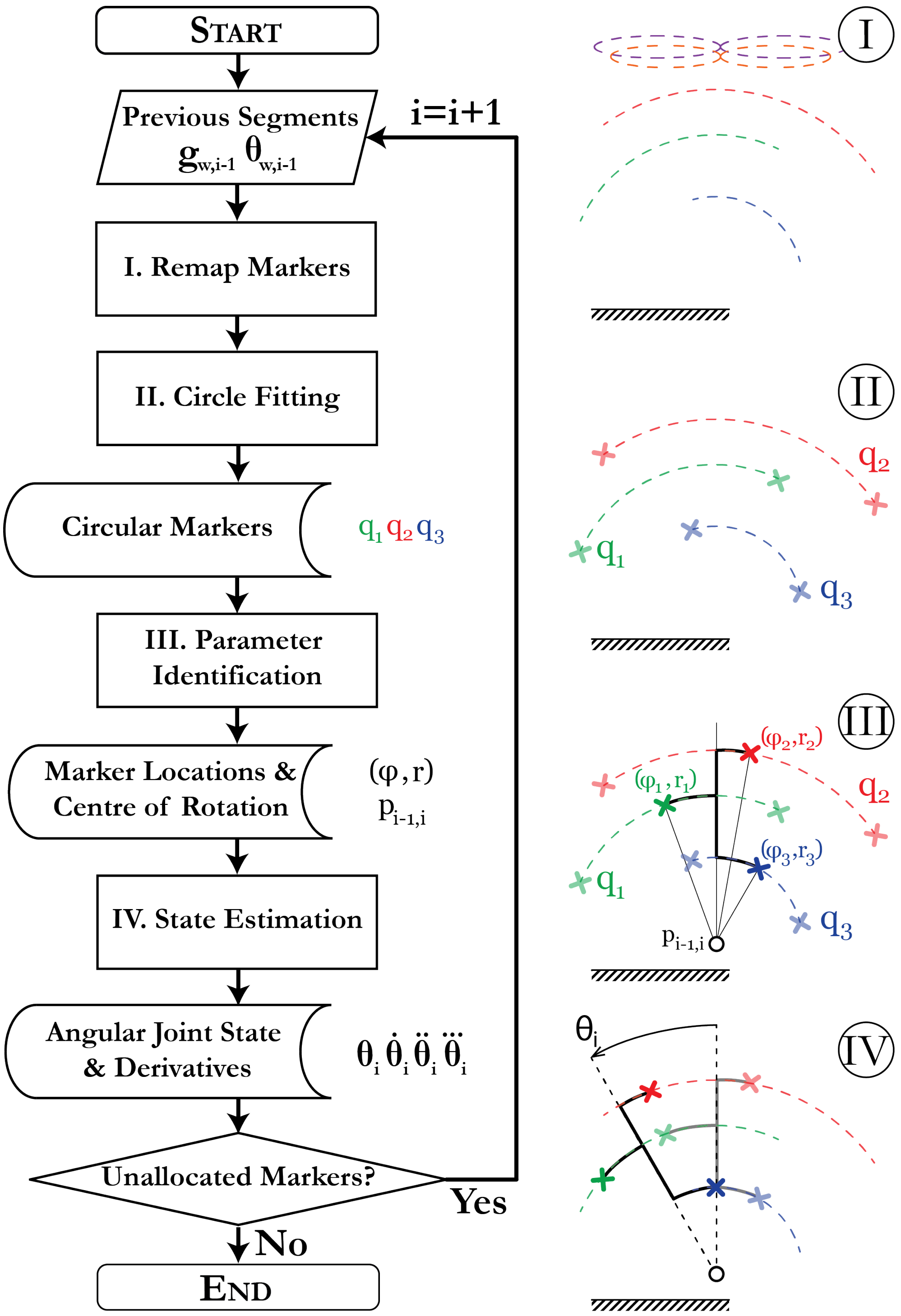
START
Previous Segments
g w,i-1 θ w,i-1
i=i+1
I. Remap Markers
II. Circle Fitting
Circular Markers
q1 q2 q3
III. Parameter Identification
Marker Locations & Centre of Rotation
(φ,r)
pi-1,i
IV. State Estimation
Angular Joint State & Derivatives
θi θ̇i θ̈i θ⃛i
Unallocated Markers?
Yes
No
END
I
II
q2
q1
q3
III
(φ2,r2)
(φ1,r1)
q2
(φ3,r3)
q1
q3
pi-1,i
θi
IV

Figure 3.1: Overview of the Kinematic recovery framework. Left: Flowchart of algorithm. Right: Corresponding cartoons of steps in the algorithm. I. Markers remapped to the $i-1$ frame, II. Markers moving along circular paths, III. Markers moving about a common centre $\boldsymbol{p}_{i-1,i}$ with local coordinates $(\boldsymbol{\phi}, \boldsymbol{r})$, IV. Inverse Kinematics to recover joint state $\boldsymbol{\theta}, \dot{\boldsymbol{\theta}}, \ddot{\boldsymbol{\theta}}, \dddot{\boldsymbol{\theta}}$.

Chapter 4

Dynamic Modelling

The kinematic models introduced in Chapter 3 give a representation of the geometry and motions of an individual. This chapter builds on these kinematic models, by linking the motions of the individual to the forces they exert on their surroundings. This allows for estimation of the dynamic model of an individual. This model includes estimates of an individual's *dynamic parameters*, the set of their limb masses and inertias.

Section 4.1 reviews the existing literature on system dynamic modelling methods used in robotics and biological systems. Building on the geometric tools introduced in Chapter 2 and the kinematic models from Chapter 3, a geometric method for dynamic parameter recovery is introduced in Section 4.2. The applications of these dynamic recovery methods are applied to robots in Chapter 5 and to clinical tests in Chapter 6.

4.1 State of the Art

The dynamics of a system can be written in the form:

$$\boldsymbol{I}(\boldsymbol{\theta})\ddot{\boldsymbol{\theta}} + \boldsymbol{C}(\boldsymbol{\theta}, \dot{\boldsymbol{\theta}}) = \boldsymbol{\tau} \tag{4.1}$$

where $\boldsymbol{I}$ is the matrix of generalised inertias of the system and $\boldsymbol{C}$ is a generalised bias force[36]. Applications of dynamic models are typically separated into *forward* and *inverse* dynamics. Forward dynamics studies the evolution of the system state $\boldsymbol{\theta}(t)$ given knowledge of the applied forces and torques $\boldsymbol{\tau}$. Inverse dynamics investigates the inverse of this problem, determining the torques required to perform a desired trajectory.

This work focuses on the estimation of the matrices $\boldsymbol{I}$ and $\boldsymbol{C}$ for a given system, allowing for application of the forward and inverse problems. The development and estimation of dynamic models is introduced in the application to robotic systems in Section 4.1.1. Section 4.1.2 shows the current state of the art for human modelling, covering conventional techniques for estimation of an individual's dynamic parameters, and the prior work on extending the robotics framework to biological systems.

4.1.1 Robotics

There is a natural application of dynamic modelling to the field of robotics and control. This has led to a significant amount of prior work focusing on the development of dynamic models.

A common method for performing this identification is via *Closed Loop Output Error* methods (CLOE)[47][57][61][67]. These methods compare the responses of a simulated and true system when given an input torque, and updates the model parameters until the error between the two systems is negligible. While these methods are useful in robotic applications they depend on direct measurement of the joint torques, which are challenging to observe directly in a non-invasive manner in biological systems. Instead the Dynamic Identification Modelling (DIM) approach will be explored based on the prior application in human modelling[7][59][127].

4.1.1.1 Dynamic Identification Modelling

While there is a geometric formulation for the model of a dynamic system (Section 2.4), a more common approach to the kinematic and dynamic modelling process is through the use of the Denavit-Hartenberg notation[36][65]. This is a framework for constructing kinematic and dynamic models of a system. Under this formulation, it is possible to develop a *Dynamic Identification Model* (DIM)[60][65] that allows for estimation of the system dynamics.

The dynamics of a system can be written in the form:

$$\begin{bmatrix} \boldsymbol{I}_{1,1} & \boldsymbol{I}_{1,2} \\ \boldsymbol{I}_{2,1} & \boldsymbol{I}_{2,2} \end{bmatrix} \begin{bmatrix} \ddot{\boldsymbol{q}}_0 \\ \ddot{\boldsymbol{\theta}} \end{bmatrix} + \begin{bmatrix} \boldsymbol{c}_1 \\ \boldsymbol{c}_2 \end{bmatrix} = \begin{bmatrix} \boldsymbol{0} \\ \boldsymbol{\tau} \end{bmatrix} + \sum_{k=1}^{N_c} \begin{bmatrix} \boldsymbol{K}_{k,1} \\ \boldsymbol{K}_{k,2} \end{bmatrix} \boldsymbol{F}_k \tag{4.2}$$

where $\boldsymbol{F}_k$ are the external forces acting on the system.

Equation 4.2 can be rewritten to obtain a linear expression of the dynamic parameters of the system[65]:

$$\begin{bmatrix} \boldsymbol{Y}_1 \\ \boldsymbol{Y}_2 \end{bmatrix} \boldsymbol{\phi}_F = \begin{bmatrix} \boldsymbol{0} \\ \boldsymbol{\tau} \end{bmatrix} + \sum_{k=1}^{N_c} \begin{bmatrix} \boldsymbol{K}_{k,1} \\ \boldsymbol{K}_{k,2} \end{bmatrix} \boldsymbol{F}_k \tag{4.3}$$

where $\boldsymbol{Y}$ is the *regressor* of the kinematic state. The regressor is a matrix constructed from the kinematic model of the system, and the observed state trajectories. The vector $\boldsymbol{\phi}_F$

contains the *full* dynamic parameters for the n links in the system and can be written as:

$$\boldsymbol{\phi}_F = \begin{bmatrix} \boldsymbol{\phi}_{F,1} \\ \vdots \\ \boldsymbol{\phi}_{F,i} \\ \vdots \\ \boldsymbol{\phi}_{F,n} \end{bmatrix} = \begin{bmatrix} \vdots \\ \begin{bmatrix} m_i \\ mrx_i \\ mry_i \\ mrz_i \\ Ixx_i \\ Iyy_i \\ Izz_i \\ Ixy_i \\ Ixz_i \\ Iyz_i \end{bmatrix} \\ \vdots \end{bmatrix} \in \mathbb{R}^{10n \times 1} \tag{4.4}$$

The generation of the full regressor $\boldsymbol{Y}$ is explored in Khalil[65], and an open source Python script for DIM generation from modified Denavit-Hartenburg parameters provided through Open SyMoRo[64].

Given knowledge of the kinematics of the system and the contact forces, Equation 4.3 becomes a simple matrix equation of the form:

$$\boldsymbol{Y}_F \boldsymbol{\phi}_F = \boldsymbol{\Gamma} \tag{4.5}$$

where $\boldsymbol{\phi}_F$ is to be determined. Equation 4.5 can be used to estimate the dynamic parameters from the observations through the optimisation cost function:

$$f(\boldsymbol{\phi}_F) = \left\| \boldsymbol{Y}_F \boldsymbol{\phi}_F - \boldsymbol{\Gamma} \right\|_2^2 + \lambda_\phi \left\| \boldsymbol{\phi}_F \right\|_2^2 \tag{4.6}$$

where the λ_ϕ term weights and minimises the total size of the recovered dynamic parameters.

This process requires $\boldsymbol{Y}_F$ to be *well conditioned.* The condition number of $\boldsymbol{Y}_F$ is dependent on both the kinematic model of the system and the excitation of the observed action. In many cases Equation 4.5 will not be well conditioned leading to an ill-posed recovery process.

To overcome this limitation, the well conditioned components of Equation 4.5 can be used in recovery. This results in a DIM that recovers the well-conditioned subset of $\boldsymbol{\phi}_F$. These recoverable dynamic parameters are termed the *base parameters.*

4.1.1.2 Base Parameters

There are a number of conditions that can result in a poorly conditioned regressor. Some dynamic parameters may not be observable in the system, due to coupling with other parameters or not being excited. These parameters can be regrouped or removed from the regressor. The vector of these regrouped dynamic parameters are the base parameters $\boldsymbol{\phi}_b$ and form the *minimal* DIM:

$$\boldsymbol{Y}_b \boldsymbol{\phi}_b = \boldsymbol{\Gamma} \tag{4.7}$$

The minimal regressor $\boldsymbol{Y}_b$ can be constructed through application of the QR decomposition[65]. Each column of the regressor $\boldsymbol{Y}$ corresponds to a single dynamic parameter in $\boldsymbol{\phi}$. If a column is found to be entirely zeros, then the corresponding dynamic parameter is not excited and is removed from the regressor. These parameters can be found by identifying the zero elements on the diagonal of the matrix $\boldsymbol{Y}_F^T\boldsymbol{Y}_F$. Removing these zero columns results in a reduced regressor $\boldsymbol{Y}_r$.

The $\boldsymbol{R}$ matrix from the QR decomposition of $\boldsymbol{Y}_r$ can be used determine the linearly independent parameters. The numerical zero for the dataset containing r samples can be defined as:

$$\mathbf{0}_N = r\epsilon \max|\boldsymbol{R}_{i,i}| \tag{4.8}$$

This numerical zero can be used to split the reduced regressor $\boldsymbol{Y}_r$ into a linearly independent part $\boldsymbol{Y}_{r1}$ where $|\boldsymbol{R}_{i,i}| \geq \mathbf{0}_N$, and a linearly dependent component $\boldsymbol{Y}_{r2}$. The linearly dependent columns can be written as a combination of the linearly independent terms via:

$$\boldsymbol{Y}_{r2} = \boldsymbol{Y}_{r1}\boldsymbol{\beta} \tag{4.9}$$

Therefore, parameters can be regrouped based on the structure of $\boldsymbol{\beta}$. The regressor of the regrouped parameters is termed the *minimal* regressor and is denoted $\boldsymbol{Y}_b$ with the corresponding *base* parameters $\boldsymbol{\phi}_b$. The cost function for the minimal regressor is therefore:

$$f(\boldsymbol{\phi}_b) = \|\boldsymbol{Y}_b\boldsymbol{\phi}_b - \boldsymbol{\Gamma}\|_2^2 + \lambda_\phi \|\boldsymbol{\phi}_b\|_2^2 \tag{4.10}$$

4.1.1.3 Physical Consistency

While the estimation of base parameters via the minimal regressor is better conditioned than from the full regressor, the recovered parameters are not guaranteed to be physically achievable. This may result in negative masses, non-positive-semi-definite matrices of inertia, and infeasible combinations of zero, first, and second mass moments of inertia[81][144].

When performing dynamic recovery, the most common method for avoiding physical inconsistency is to minimise the error between the recovered parameters and a reference model[8]. This reference model can be taken from literature or a CAD model, leading to the cost function:

$$f(\boldsymbol{\phi}_F) = \|\boldsymbol{Y}_F\boldsymbol{\phi}_F - \boldsymbol{\Gamma}\|_2^2 + \lambda_{ref}\|\boldsymbol{\phi}_F - \boldsymbol{\phi}_{ref}\|_2^2 + \lambda_\phi \|\boldsymbol{\phi}_F\|_2^2 \tag{4.11}$$

While this method anchors the parameters to lie near their expected values, there is still no guarantee that the parameters themselves are physically consistent. Constraints on the positive-semi-definiteness of the inertia matrix may not be possible if the corresponding elements are not in the set of linearly independent parameters. This presents a challenge for the estimation of a set of physically consistent dynamic parameters.

A method to ensure physical consistency was introduced by Ayusawa[8]. A finite grid of mass points is used to represent the rigid-body object (Figure 4.1). While the locations of

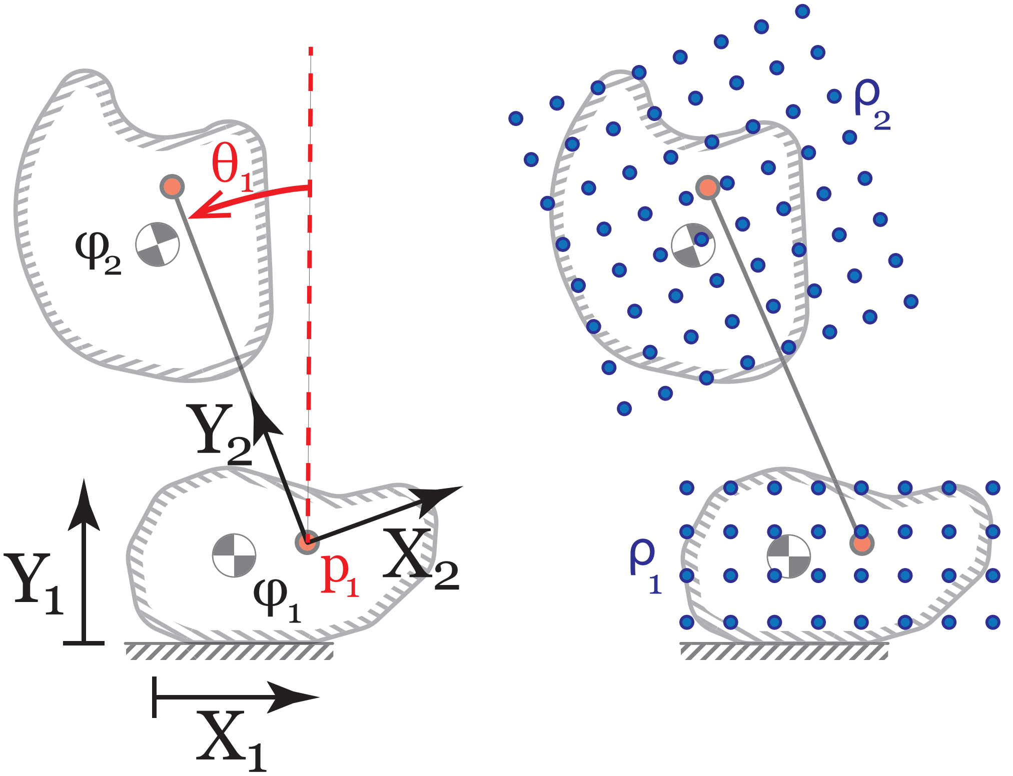

Figure 4.1: Cartoons showing the Ayusawa method for a single pendulum system. Left: Dynamic system for a single pendulum. The joint location is denoted $\boldsymbol{p}_1$, with the angle of rotation parametrised by θ_1. The frame of the fixed link and moving link are labelled as frames one and two respectively. The dynamic parameters for each link are contained in the parameter vectors $\boldsymbol{\psi}_1$ and $\boldsymbol{\psi}_2$. Right: Cartoon of the point mass grid for the physically consistent recovery. A grid of points of unknown mass distribution $\boldsymbol{\rho}_1$ and $\boldsymbol{\rho}_2$ are used to represent the true dynamic parameters.

these mass points are known apriori, their weightings can be found through an optimisation process via the equation:

$$\boldsymbol{\phi}_F = \begin{bmatrix} \vdots \\ \begin{bmatrix} m_i \\ mrx_i \\ mry_i \\ \vdots \end{bmatrix} \\ \vdots \end{bmatrix} = \begin{bmatrix} \ddots & \mathbf{0} & \mathbf{0} \\ \mathbf{0} & \begin{bmatrix} 1 & \dots & 1 \\ rx_{i,1} & \dots & rx_{i,p} \\ ry_{i,1} & \dots & ry_{i,p} \\ \vdots & & \vdots \end{bmatrix} & \mathbf{0} \\ \mathbf{0} & \mathbf{0} & \ddots \end{bmatrix} \begin{bmatrix} \vdots \\ \begin{bmatrix} \rho_{i,1} \\ \vdots \\ \rho_{1,p_i} \end{bmatrix} \\ \vdots \end{bmatrix} = \boldsymbol{P}\boldsymbol{\rho} \tag{4.12}$$

This relation matrix $\boldsymbol{P}$ can then be used to form the cost function:

$$f(\rho) = \|\boldsymbol{Y}_F\boldsymbol{P}\boldsymbol{\rho} - \boldsymbol{\Gamma}\|_2^2 + \lambda_{ref}\,\|\boldsymbol{P}\boldsymbol{\rho} - \boldsymbol{\phi}_{ref}\|_2^2 + \lambda_\rho\,\|\boldsymbol{\rho}\|_2^2 \tag{4.13}$$

4.1.2 Human Modelling

While there are a number of methods for estimating the dynamic parameters in robotic systems, the lack of a non-invasive method to estimate joint torques makes the conventional approaches to DIM challenging. To overcome this challenge, it is possible to develop a DIM that only requires knowledge of the contact forces of a system, without the true joint torques being known. While this may result in a reduction in the number of recoverable base parameters, it allows for a direct extension from robotics to biological systems.

4.1.2.1 Contact Modelling

The full dynamics of a system were expressed in Equation 4.2. The top portion of these equations do not have a dependence on the system torques, only the contact forces. This allows for the dynamic equations for the base link to be written as:

$$\begin{bmatrix} \boldsymbol{I}_{1,1} & \boldsymbol{I}_{1,2} \end{bmatrix} \begin{bmatrix} \ddot{\boldsymbol{q}}_0 \\ \ddot{\boldsymbol{\theta}} \end{bmatrix} + \boldsymbol{b}_1 = \sum_{k=1}^{N_c} \boldsymbol{K}_{k,1} \boldsymbol{F}_k \tag{4.14}$$

Equation 4.14 can be converted into regressor form, allowing for estimation of the full and base parameters as before. This method has been used in the estimation of humanoid systems through the measurement of the ground contact forces and aerial motions[6][7]. An online formulation of the contact based modelling method has been developed to allow for feedback of the condition number of different limbs, assisting in the recovery process[5][128]. This has led to the extension to affordable sensors such as the Wii balance board and Kinect [13][44][145].

4.1.3 Challenges

While there have been a number of significant advances in the development of dynamic human models through contact modelling, the tools are still in their infancy. One of the largest limitations in the existing work is the separate treatment of the kinematic and dynamic modelling processes. It has been shown that variation in the kinematic model parameters can have a substantial effect on dynamic analysis[108]. Despite this, the majority of the prior work treats the dynamic recovery process in isolation, making comparison between studies challenging. Error due to the kinematic recovery method used, and the sensitivity of the recovered parameters to noise in the dynamic parameters has not been studied. The effect of temporal misalignment between the motion capture and contact force streams has not been studied.

There are limitations in the methods used to experimentally validate these techniques. The error in the contact wrench is typically taken to be the measure of model performance[78]. However as the same error is used as the optimisation cost function, these methods are *doomed to succeed.*

With the use of reference models, it is challenging to determine the correct weightings between matching the observed contact wrench and remaining close to the expected dynamic parameters. Due to the significant variation between individuals and the lack of a unified modelling approach, there is a clear need for a link between the kinematic and dynamic modelling approaches.

4.2 Dynamic Recovery Framework

This section outlines the original work performed on dynamic identification modelling. Building on the kinematic results of Chapter 3, a geometric form of the regressor is constructed. A modification of the minimal modelling process is introduced, allowing for a linear relation to be formed between the full and base parameters. This allows for the development of a method that is both physically consistent while only operating on the base parameters.

4.2.1 Geometric DIM

The recursive formulation for deriving the dynamics of a system under the geometric notation was introduced in Section 2.4. Recalling the matrix form of backward recursive dynamics equation (Equation 2.57), the dynamic parameters can be rewritten in terms of combinations of $\boldsymbol{IV}$ and $\boldsymbol{I\dot{V}}$. These terms have the similar form of the inertial matrix post multiplied by a velocity or acceleration twist. To generate the dynamic model, these terms are rewritten in terms of the full dynamic parameter vector $\boldsymbol{\phi}_F$:

$$\begin{aligned}\boldsymbol{IV} &= \begin{bmatrix} m_i\mathbb{I} & -m_i\hat{\boldsymbol{r}}_i \\ m_i\hat{\boldsymbol{r}}_i & \boldsymbol{J}_i - m_i\hat{\boldsymbol{r}}_i^2 \end{bmatrix} \begin{bmatrix} \boldsymbol{v}_i \\ \boldsymbol{\omega}_i \end{bmatrix} \\ &= \begin{bmatrix} \boldsymbol{v}_i & \hat{\boldsymbol{\omega}}_i & \boldsymbol{0} & \boldsymbol{0} \\ \boldsymbol{0} & -\hat{\boldsymbol{v}}_i & diag(\boldsymbol{\omega}_i) & \begin{bmatrix} \omega_2 & \omega_3 & 0 \\ \omega_1 & 0 & \omega_3 \\ 0 & \omega_1 & \omega_2 \end{bmatrix} \end{bmatrix} \boldsymbol{\phi}_{F,i} \\ &= \boldsymbol{Y}_{i,\boldsymbol{V}}\boldsymbol{\phi}_{F,i}\end{aligned} \tag{4.15}$$

$$\boldsymbol{I\dot{V}} = \begin{bmatrix} \dot{\boldsymbol{v}}_i & \hat{\dot{\boldsymbol{\omega}}}_i & \boldsymbol{0} & \boldsymbol{0} \\ \boldsymbol{0} & -\hat{\dot{\boldsymbol{v}}}_i & diag(\dot{\boldsymbol{\omega}}_i) & \begin{bmatrix} \dot{\omega}_2 & \dot{\omega}_3 & 0 \\ \dot{\omega}_1 & 0 & \dot{\omega}_3 \\ 0 & \dot{\omega}_1 & \dot{\omega}_2 \end{bmatrix} \end{bmatrix} \boldsymbol{\phi}_{F,i} = \boldsymbol{Y}_{i,\dot{\boldsymbol{V}}}\boldsymbol{\phi}_{F,i} \tag{4.16}$$

This allows the recursive dynamic equations to be rewritten in the form:

$$\boldsymbol{\Gamma}_i = Ad^T_{\boldsymbol{g}^{-1}_{i,i+1}(\theta_{i+1})}\boldsymbol{\Gamma}_{i+1} + \boldsymbol{Y}_{i,\dot{\boldsymbol{V}}}\boldsymbol{\phi}_{F,i} - \boldsymbol{ad}^T_{\hat{\boldsymbol{V}}_i}\boldsymbol{Y}_{i,\boldsymbol{V}}\boldsymbol{\phi}_{F,i} + \boldsymbol{\Gamma}_{i,E} \tag{4.17}$$

Exploiting the matrix form of adjoint, the recursive DIM element $\boldsymbol{Y}_i$ can be defined:

$$\begin{aligned}\boldsymbol{\Gamma}_i &= Ad^T_{\boldsymbol{g}^{-1}_{i,i+1}(\theta_{i+1})}\boldsymbol{\Gamma}_{i+1} + \left[\boldsymbol{Y}_{i,\dot{\boldsymbol{V}}} - \boldsymbol{ad}^T_{\hat{\boldsymbol{V}}_i}\boldsymbol{Y}_{i,\boldsymbol{V}}\right]\boldsymbol{\phi}_{F,i} + \boldsymbol{\Gamma}_{i,E} \\ &= Ad^T_{\boldsymbol{g}^{-1}_{i,i+1}(\theta_{i+1})}\boldsymbol{\Gamma}_{i+1} + \boldsymbol{Y}_i\boldsymbol{\phi}_{F,i} + \boldsymbol{\Gamma}_{i,E}\end{aligned} \tag{4.18}$$

The recursion shown in Equation 4.18 can be used to find the relation between the ground contact wrench $\boldsymbol{\Gamma}_0$ and the systems dynamic parameters:

$$\begin{aligned}
\boldsymbol{\Gamma}_0 &= \boldsymbol{Y}_0\boldsymbol{\phi}_{F,0} + \boldsymbol{\Gamma}_{0,E} + Ad^T_{\boldsymbol{g}_{0,1}^{-1}(\theta_1)}\boldsymbol{\Gamma}_1 \\
&= \boldsymbol{Y}_0\boldsymbol{\phi}_{F,0} + \boldsymbol{\Gamma}_{0,E} + Ad^T_{\boldsymbol{g}_{0,1}^{-1}(\theta_1)}\left(\boldsymbol{Y}_1\boldsymbol{\phi}_{F,1} + \boldsymbol{\Gamma}_{1,E} + Ad^T_{\boldsymbol{g}_{1,2}^{-1}(\theta_2)}\boldsymbol{\Gamma}_2\right) \\
&= \left(\boldsymbol{Y}_0\boldsymbol{\phi}_{F,0} + Ad^T_{\boldsymbol{g}_{0,1}^{-1}(\theta_1)}\boldsymbol{Y}_1\boldsymbol{\phi}_{F,1}\right) + \left(\boldsymbol{\Gamma}_{0,E} + Ad^T_{\boldsymbol{g}_{0,1}^{-1}(\theta_1)}\boldsymbol{\Gamma}_{1,E}\right) + Ad^T_{\boldsymbol{g}_{0,2}^{-1}(\theta_2)}\boldsymbol{\Gamma}_2
\end{aligned} \tag{4.19}$$

This results in the recursive geometric dynamic identification model:

$$\boldsymbol{\Gamma}_W = \boldsymbol{Y}\boldsymbol{\phi}_F + \boldsymbol{\Gamma}_C \tag{4.20}$$

where $\boldsymbol{\Gamma}_W$ is the contact wrench at the base frame, $\boldsymbol{Y}$ is the regressor:

$$\boldsymbol{Y} = \begin{bmatrix} \boldsymbol{Y}_0 & Ad^T_{\boldsymbol{g}_{0,1}^{-1}(\theta_1)}\boldsymbol{Y}_1 & \dots & Ad^T_{\boldsymbol{g}_{0,n}^{-1}(\theta_n)}\boldsymbol{Y}_n \end{bmatrix} \tag{4.21}$$

$\boldsymbol{\phi}_F$ is the vector of the full dynamic parameters:

$$\boldsymbol{\phi}_F = \begin{bmatrix} \boldsymbol{\phi}_{F,0} \\ \boldsymbol{\phi}_{F,1} \\ \vdots \\ \boldsymbol{\phi}_{F,n} \end{bmatrix} \tag{4.22}$$

and $\boldsymbol{\Gamma}_C$ is the net contact wrench acting on the base frame:

$$\boldsymbol{\Gamma}_C = \boldsymbol{\Gamma}_{0,E} + Ad^T_{\boldsymbol{g}_{0,1}^{-1}(\theta_1)}\boldsymbol{\Gamma}_{1,E} + \cdots + Ad^T_{\boldsymbol{g}_{0,n}^{-1}(\theta_n)}\boldsymbol{\Gamma}_{n,E} \tag{4.23}$$

4.2.2 Physically Consistent Minimal Modelling

From the prior work, there are a number of variations on the cost functions investigators can use in their research. This work introduces a minimal modelling adaptation of the physically consistent modelling approach introduced by Ayusawa[8]. The Ayusawa approach is chosen over other methods for physical consistency[81][117][144] as it has an intuitive physical meaning and a convenient matrix expression to move from the point masses to the full segment parameters.

Section 4.1.1.2 showed the conventional method for obtaining the base regressor and parameters. During this conversion process, a relation is obtained between the linearly independent and dependent columns (Equation 4.9). These relations can be instead used to build a *regrouping matrix* $\boldsymbol{M}$ that represents how the full dynamic parameters should be regrouped to form the base parameters:

$$\boldsymbol{\phi}_b = \boldsymbol{M}\boldsymbol{\phi}_F \tag{4.24}$$

This regrouping allows for direct application of the Ayusawa method, providing a relationship between the base parameters and the discretised point mesh $\boldsymbol{\rho}$:

$$\boldsymbol{\phi}_b = \boldsymbol{M}\boldsymbol{P}\boldsymbol{\rho} \tag{4.25}$$

(where $\boldsymbol{P}$ is the matrix relation between the grid of point masses and the full dynamic parameters). This leads directly to the cost function:

$$f(\boldsymbol{\rho}) = \|\boldsymbol{Y}_b\boldsymbol{M}\boldsymbol{P}\boldsymbol{\rho} - \boldsymbol{\Gamma}\|_2^2 + \lambda_\phi \|\boldsymbol{\rho}\|_2^2 \tag{4.26}$$

This cost function allows for a guarantee of physical consistency, while operating on the minimal regressor, resulting in a better posed optimisation problem.

Chapter 5

Robotic Validation

This chapter tests the kinematic and dynamic modelling methods introduced in Chapters 3 and 4 on a simple robotic manipulator. The robot has a kinematic and dynamic model that can be used for validation of the techniques, as well as internal encoding of joint state. This allows for validation of each step of the recovery process, and the development of an experimental validation methodology for interpreting the results of DIM recovery.

5.1 UR5 Robot

The UR5 is a six degree-of-freedom robot that can be controlled over an Ethernet connection[125]. The UR5 robot is capable of publishing the joint angles, angular velocities, and torques at 125Hz allowing for comparisons in the state and torque estimates. The *UR5 modern driver*[123] was used to control the robot through *Robotic Operating System* (ROS)[106].

A kinematic and dynamic model is provided from the ROS controller[88], and an improved dynamic model has been developed by Kufieta[67]. In their thesis, Kufieta developed and evaluated a number of uniform and varying density models for the UR5 robot based on the inner components of the robot. These models were evaluated based on their ability to estimate the end-effector accelerations for given inputs.

5.2 Method

The UR5 robot was attached to an *AMTI OPT 464508*[1] force platform using a custom tool steel bracket. The steel bracket used was 12mm thick and a total mass (including fittings and fasteners) of $7.817kg$. A *Phasespace Impulse X2*[104] motion capture system was used to track eighteen active markers on the robot, and seven active markers on the base (Figure 5.1). These two systems were synchronised using *Meinburg NTP*[87] with a temporal accuracy of $\leq 2ms$.

The vertical position was used as the robot's resting state, with the shoulder, elbow, and wrist joints all rotating in the same plane. Each joint was moved individually in a sinusoid

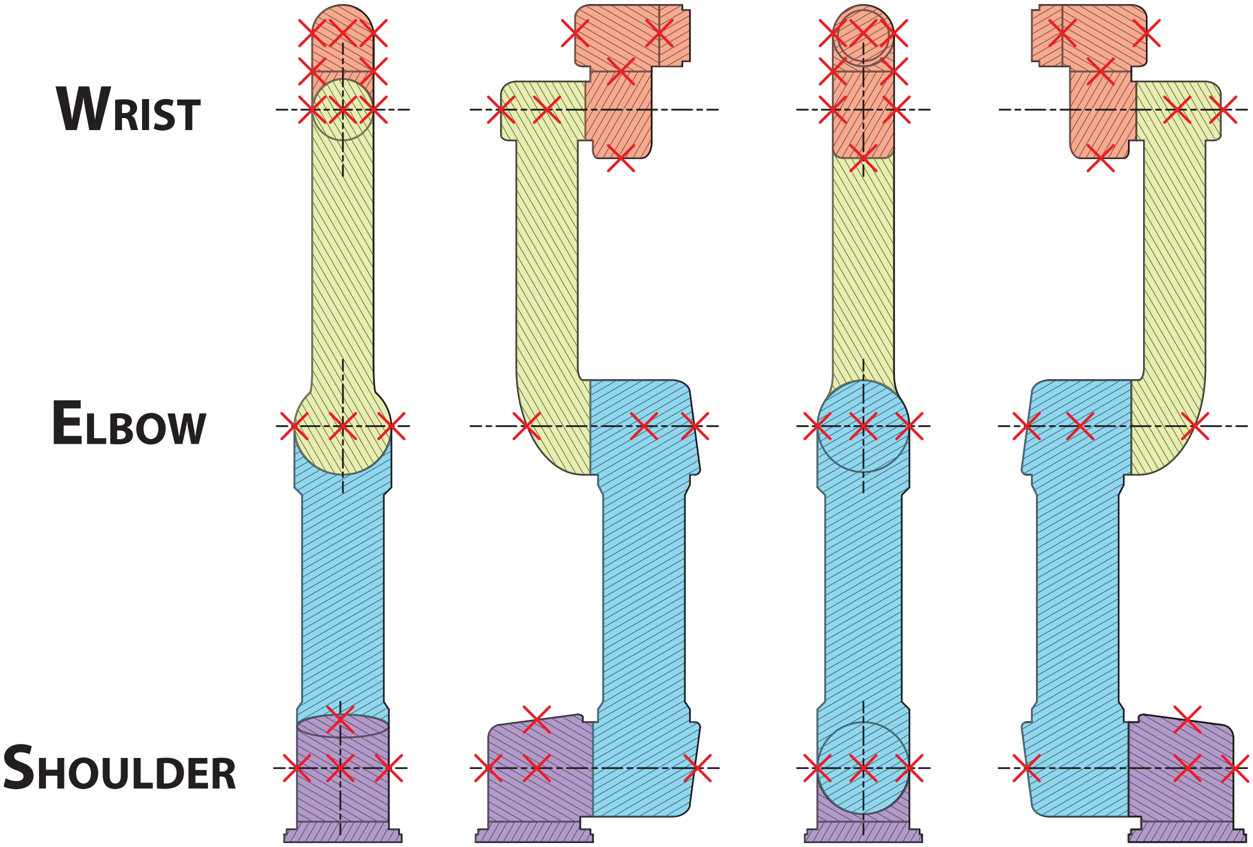

Figure 5.1: Cartoon of the UR5 robot. The four segments of the robot that were excited are shown in different colours. The joint centres are marked with dotted lines. The location of motion capture markers on the UR5 robot are shown as red crosses.

of magnitude $\frac{\pi}{4}$ radians for a total of 5 reps. This was repeated at two frequencies, a fast motion at $0.5Hz$ and a slow motion at $0.25Hz$.

This protocol was performed on the shoulder, elbow, and wrist in the vertical configuration, and again with the robot rotated $\frac{\pi}{4}$ radians about the vertical axis. Each experiment of 5 repetitions of a single joint were processed as a single trial. This allows for a comparison between joints, orientations, and speeds. The fast speed was not attempted on the shoulder axis due to the risk of tipping the robot.

5.3 Kinematic Recovery

The kinematic recovery method introduced in Chapter 3 was used to recover the kinematic parameters for the robot. Section 5.3.1 outlines the results of this process, which are then interpreted in Section 5.3.2

5.3.1 Results

The results for this recovery process are shown in Table 5.1. Plots showing the result of each step of the kinematic recovery process are shown in Figures 5.2 and 5.3. The results of these experiments are discussed in Section 5.3.2, and used in the dynamic recovery of the UR5 manipulator (Section 5.4).

Table 5.1: Kinematic parameters and associated errors in marker positions, angles and angular velocities for the single axis experiments. Mean values shown with standard deviation in parenthesis.

Joint	Orientation	Speed	l_1 (mm)	ϵ_M (mm)	ϵ_θ (deg.)	$\epsilon_{\dot{\theta}}$ (deg./s)
Sho.	0 deg	Slow	100.7 (0.5)	1.3 (0.8)	0.0 (0.1)	0.0 (1.4)
	45 deg	Slow	101.7 (0.5)	0.8 (0.5)	0.0 (0.3)	0.0 (1.5)
Elb.	0 deg	Slow	528.9 (0.7)	0.7 (0.4)	0.0 (0.1)	0.0 (1.2)
		Fast	529.6 (0.4)	0.6 (0.4)	0.0 (0.3)	0.1 (3.7)
	45 deg	Slow	525.6 (0.0)	0.6 (0.3)	0.0 (0.3)	0.0 (1.1)
		Fast	525.0 (0.0)	0.6 (0.3)	0.0 (0.4)	0.0 (3.5)
Wri.	0 deg	Slow	917.4 (0.4)	1.8 (0.9)	0.0 (2.6)	0.0 (4.6)
		Fast	917.2 (1.2)	1.4 (0.8)	0.0 (2.6)	0.0 (9.3)
	45 deg	Slow	914.2 (3.2)	2.4 (1.2)	0.0 (3.0)	0.0 (4.9)
		Fast	915.5 (4.3)	1.6 (0.9)	0.0 (3.6)	0.3 (10.8)

5.3.2 Discussion

Table 5.1 summarises the key results for the kinematic recovery process of the UR5 robot. From this table it is possible to estimate the accuracy and precision of the recovery method.

The lengths shown in Table 5.1 show high precision, with a standard deviation of under 1 mm for the shoulder and elbow. The precision decreases in the wrist case for the 45 degree orientation experiments. Using the published segment lengths as a reference, the expected lengths for the segments are $101, 526, 918$ mm respectively for the shoulder, elbow, and wrist positions from the base frame[88][125]. This indicates that the accuracy of the proposed method is high, with mean length errors of under 2 mm. The mean errors in the lengths appear to correlate with the orientation of the experiment instead of the speed of the motion.

This is potentially due to variation in camera viewpoint, with the elbow being more visible in the 45 degree orientation, and the wrist in the 0 degree orientation.

The marker re-projection errors ϵ_M indicate how well the kinematic recovery method matched the observed motion capture data. The re-projection appears to be low, with the major variations being on at the segment level, instead of varying with speed or orientation. This suggests that the number and locations of the markers may be a significant factor for the kinematic recovery process.

This appears to be confirmed by the errors in the recovered state trajectories. The angular position appears to be well recovered for the shoulder and elbow, with low mean and standard deviations. This angular position error increases for the wrist. Combined with the increased error in marker re-projection, it is possible that the relatively poor recovery of the wrist is due to the low Cartesian movement of the markers compared to the shoulder and elbow experiments.

The standard deviations of recovered angular velocities are higher, with faster motions having a larger associated error in angular velocity. This increases significantly for the wrist due to the relatively poor angular position recovery. While the standard deviations in the angular velocity trajectories are higher than for the positions, their overall value is still small.

Figures 5.2 and 5.3 show the recovery process for two representative trials. The raw markers, fit kinematic model, and recovered joint state are shown.

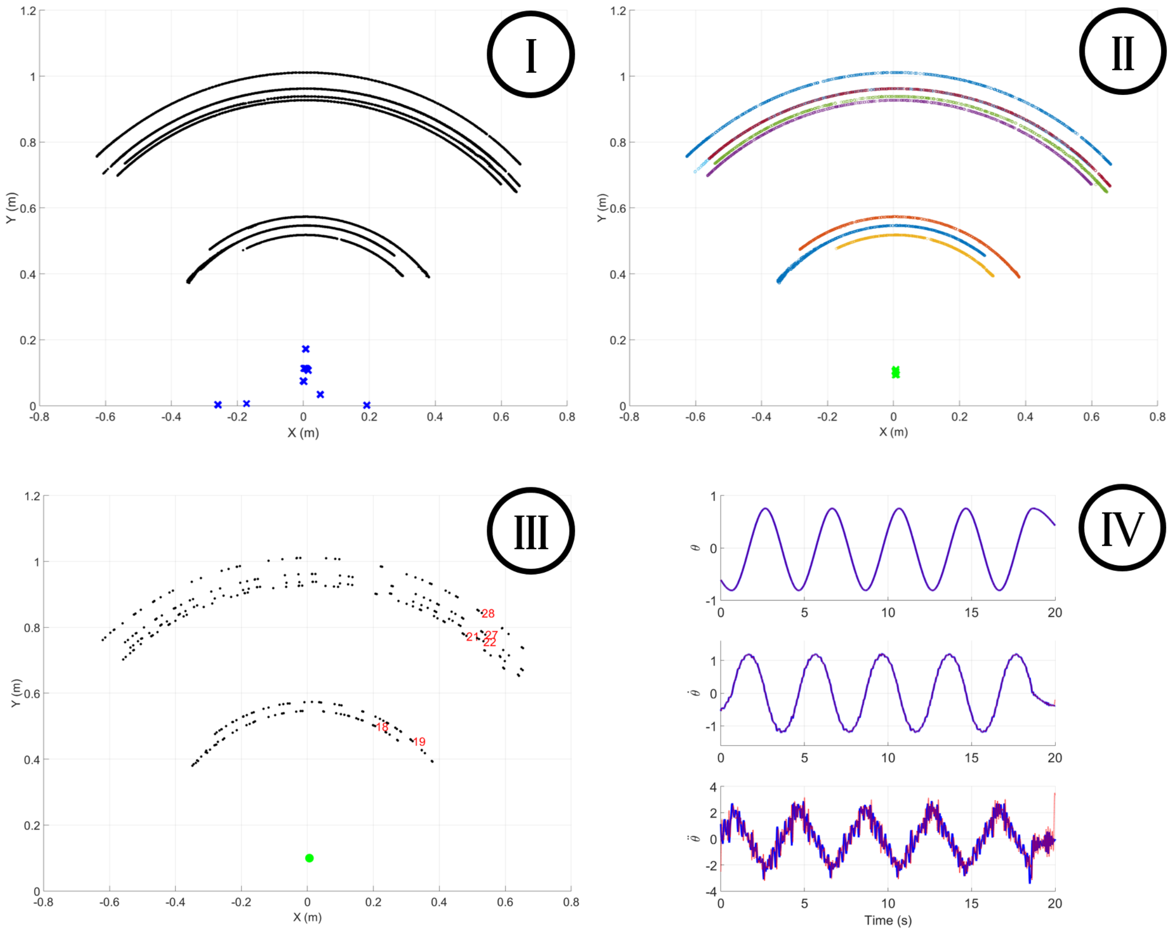

Figure 5.2: Plots showing the kinematic recovery process for the slow rotation of the shoulder joint. I. Separation into moving, and stationary markers (black circles and blue crosses respectively). II. Circle fitting. Individual marker traces (colour arcs), and corresponding circle centres (green crosses). III. Parameter identification. Local marker coordinates (annotations), and centre of rigid body (green circle) shown. IV. Kinematic recovery. Recovered angular position, velocity, and acceleration data. Units are in radians. Blue trajectory is recovered via the proposed fourth order UKF. The red trajectory is the result of differentiating and filtering the recovered position trajectory. [67].

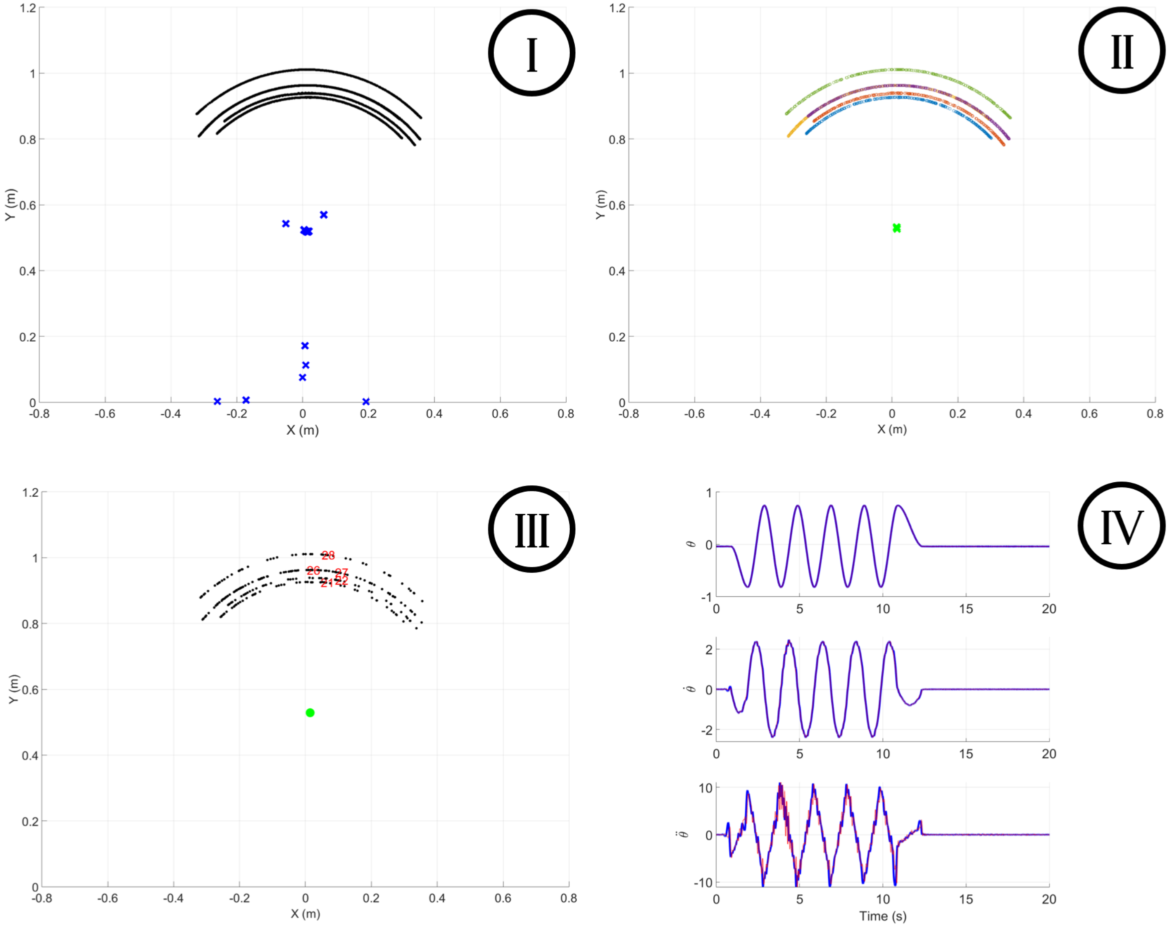

Figure 5.3: Plots showing the kinematic recovery process for the fast rotation of the elbow joint. I. Separation into moving, and stationary markers (black circles and blue crosses respectively). II. Circle fitting. Individual marker traces (colour arcs), and corresponding circle centres (green crosses). III. Parameter identification. Local marker coordinates (annotations), and centre of rigid body (green circle) shown. IV. Kinematic recovery. Recovered angular position, velocity, and acceleration data. Units are in radians. Blue trajectory is recovered via the proposed fourth order UKF. The red trajectory is the result of differentiating and filtering the recovered position trajectory. [67].

5.4 Dynamic Recovery

The dynamic recovery process introduced in Chapter 4 was used to recover the dynamic parameters for the UR5 robot. The joint locations recovered in Section 5.3 were used to compute the joint twists in the world frame using the equation:

$$\boldsymbol{\xi}_{W,1}^{W} = \begin{bmatrix} -\hat{\boldsymbol{\omega}}\boldsymbol{p}_J \\ \boldsymbol{\omega} \end{bmatrix} \tag{5.1}$$

where $\boldsymbol{p}_J$ is the recovered joint location, and $\boldsymbol{\omega}$ is the joint axis. As this is a planar system, $\boldsymbol{\omega}$ can be set as the axis normal to the plane.

These twists are then used to build a regressor using the recovered kinematic parameters from Section 5.3. The symbolic regressor was then compared to the regressor generated from OpenSyMoRo, a DH based toolbox for generating robotic dynamics[64]. The regressor recovered through the presented geometric framework (Equation 4.20) gave an identical result when compared to the DH model.

This regressor was then used in the minimal, physically consistent DIM outlined in Equation 4.26. The results of this DIM are shown in Section 5.4.1, and discussed in Section 5.4.2.

5.4.1 Results

The dynamic parameters recovered using the proposed DIM are shown in Table 5.2. The parameters are computed using both the robot's internal joint state (R) comprising of position and velocity measurements, and the recovered kinematic trajectories from the proposed framework (P). The error in the joint torque for each model is also shown, with the associated r^2 fit. The reference model used is the improved dynamic model from Kufieta[67].

The associated error in the joint state is shown in Table 5.3. The ground truths for the kinematic state were the directly encoded positions and velocities. The ground truth acceleration was obtained by filtering and differentiating the velocity data using a third order low pass Butterworth filter with a cutoff frequency of 20Hz. The robot joint state R was obtained by fusing the robot position and velocity state through a third order unscented Kalman filter. Table 5.4 shows the associated errors in the contact wrench for these experiments.

The five reps for a single trial were synchronised and overlaid to examine the inherent variation in each of the methods. Figures 5.4 and 5.5 show these averaged wrench trajectories and the errors for the fast elbow motion.

5.4.2 Discussion

The recovered dynamic parameters for the system are shown in Table 5.2. The condition number for these trials was found to be low, approximately 25 for the slow actions, and 5 for the fast actions. This suggests that the minimal regressors used in the recovery process were suitable for dynamic parameter recovery[128].

Table 5.2: Results of the dynamic model recovery process for three joints at two speeds. Mean values shown with standard deviation in parenthesis. Reference model from [67]. An observation of R is based on the robot's internal measurements of position and velocity, P refers to recovery via the proposed kinematic framework.

				m_1+m_2	$mx_1 +$ T_xm_2	mx_2	my_2	I_{ZZ2}	ϵ_τ	
Joint	Speed	Obs	Cond	kg	$kg \cdot m$	$kg \cdot m$	$kg \cdot m$	$kg \cdot m^2$	$N \cdot m$	r^2
Sho.	Ref.	R	-	26.633	0.000	0.000	5.540	3.760	0.039 (2.960)	0.988 (0.000)
	Slow.	R	24.329 (0.419)	27.341 (0.005)	0.080 (0.006)	-0.061 (0.009)	5.915 (0.028)	3.307 (0.110)	-0.500 (1.924)	0.995 (0.000)
		P	22.615 (0.410)	27.327 (0.005)	0.078 (0.008)	-0.059 (0.010)	5.837 (0.029)	3.413 (0.112)	-0.485 (1.967)	0.994 (0.000)
Elb.	Ref.	R	-	26.633	0.000	0.000	1.760	0.700	-0.046 (1.637)	0.972 (0.002)
	Fast	R	4.718 (0.107)	27.332 (0.005)	0.036 (0.003)	-0.001 (0.003)	1.756 (0.011)	0.767 (0.005)	-0.059 (1.441)	0.978 (0.002)
		P	5.056 (0.106)	27.315 (0.005)	0.034 (0.007)	0.005 (0.010)	1.675 (0.016)	0.766 (0.010)	-0.033 (1.572)	0.974 (0.008)
	Slow	R	27.584 (0.678)	27.352 (0.002)	0.028 (0.002)	0.003 (0.003)	1.874 (0.010)	0.493 (0.038)	-0.047 (1.231)	0.983 (0.000)
		P	25.293 (0.675)	27.347 (0.002)	0.029 (0.003)	0.002 (0.004)	1.850 (0.011)	0.516 (0.059)	-0.013 (1.063)	0.983 (0.001)
Wri.	Ref.	R	-	26.633	0.000	0.000	0.110	0.010	0.033 (0.385)	0.569 (0.003)
	Fast	R	5.424 (0.116)	27.348 (0.002)	0.036 (0.001)	0.000 (0.001)	0.139 (0.000)	0.035 (0.000)	0.047 (0.412)	0.503 (0.001)
		P	5.056 (0.106)	27.346 (0.002)	0.036 (0.001)	0.000 (0.000)	0.134 (0.000)	0.034 (0.000)	0.045 (0.399)	0.535 (0.001)
	Slow	R	28.130 (1.180)	27.347 (0.004)	0.031 (0.001)	0.003 (0.002)	0.147 (0.000)	0.038 (0.000)	0.049 (0.318)	0.635 (0.014)
		P	25.943 (1.094)	27.346 (0.004)	0.032 (0.001)	0.003 (0.002)	0.145 (0.000)	0.037 (0.000)	0.045 (0.311)	0.651 (0.014)

Table 5.3: Errors and r^2 values for the residuals of the dynamic model recovery process for three joints at two speeds. Mean values shown with standard deviation in parenthesis. Reference model from [67]. An observation of R is based on the robot's internal measurements of position and velocity, P refers to recovery via the proposed kinematic framework.

			ϵ_θ		$\epsilon_{\dot{\theta}}$		$\epsilon_{\ddot{\theta}}$	
Joint	Speed	Obs.	rad	r^2	rad/s	r^2	rad/s^2	r^2
Sho.	Slow	R	0.000 (0.001)	1.000 (0.000)	0.000 (0.005)	1.000 (0.000)	0.000 (0.229)	0.952 (0.002)
		P	0.000 (0.001)	1.000 (0.000)	0.000 (0.011)	1.000 (0.000)	0.000 (0.132)	0.983 (0.000)
Elb.	Fast	R	0.000 (0.003)	1.000 (0.000)	0.000 (0.015)	1.000 (0.000)	-0.003 (0.563)	0.979 (0.001)
		P	0.000 (0.002)	1.000 (0.000)	-0.001 (0.043)	0.999 (0.000)	0.003 (0.487)	0.985 (0.013)
	Slow	R	0.000 (0.001)	1.000 (0.000)	0.000 (0.004)	1.000 (0.000)	0.001 (0.178)	0.972 (0.000)
		P	0.000 (0.001)	1.000 (0.000)	0.000 (0.011)	1.000 (0.000)	-0.001 (0.135)	0.983 (0.009)
Wri.	Fast	R	0.000 (0.003)	1.000 (0.000)	0.000 (0.040)	1.000 (0.000)	-0.001 (0.590)	0.976 (0.001)
		P	0.000 (0.003)	1.000 (0.000)	0.000 (0.040)	0.999 (0.000)	0.001 (0.329)	0.993 (0.000)
	Slow	R	0.000 (0.001)	1.000 (0.000)	0.000 (0.005)	1.000 (0.000)	-0.001 (0.206)	0.961 (0.001)
		P	0.000 (0.001)	1.000 (0.000)	0.000 (0.013)	1.000 (0.000)	0.001 (0.172)	0.972 (0.013)

Table 5.4: Errors and r^2 values for the residuals of the dynamic model recovery process for three joints at two speeds. Mean values shown with standard deviation in parenthesis. Reference model from [67]. An observation of R is based on the robot's internal measurements of position and velocity, P refers to recovery via the proposed kinematic framework.

			ϵ_{Γ_X}		ϵ_{Γ_Y}		ϵ_{Γ_τ}	
Joint	Speed	Obs.	N	r^2	N	r^2	$N \cdot m$	r^2
Sho.	Ref.	R	0.142 (1.003)	0.975 (0.002)	-6.947 (0.810)	-0.814 (0.099)	-0.241 (2.148)	0.995 (0.001)
	Slow	R	0.146 (0.908)	0.980 (0.002)	0.000 (0.747)	0.979 (0.003)	0.000 (1.702)	0.997 (0.001)
		P	0.154 (0.865)	0.981 (0.001)	0.000 (0.873)	0.974 (0.002)	0.000 (1.812)	0.997 (0.000)
Elb.	Ref.	R	0.053 (1.737)	0.950 (0.015)	-6.859 (1.065)	-0.373 (0.086)	-0.337 (1.813)	0.985 (0.003)
	Fast	R	0.053 (1.737)	0.950 (0.015)	0.000 (1.060)	0.968 (0.008)	0.000 (1.791)	0.986 (0.003)
		P	0.078 (1.932)	0.938 (0.024)	0.000 (1.283)	0.953 (0.013)	0.000 (2.047)	0.982 (0.006)
	Slow	R	0.031 (0.429)	0.975 (0.002)	0.000 (0.276)	0.974 (0.001)	0.000 (0.639)	0.996 (0.000)
		P	0.029 (0.477)	0.947 (0.019)	0.000 (0.319)	0.966 (0.005)	0.000 (0.709)	0.995 (0.001)
Wri.	Ref.	R	-0.003 (0.278)	0.828 (0.011)	-7.014 (0.170)	-186.1 (12.03)	-0.366 (0.391)	0.828 (0.002)
	Fast	R	-0.004 (0.230)	0.882 (0.012)	0.000 (0.128)	0.939 (0.010)	0.000 (0.213)	0.973 (0.003)
		P	-0.004 (0.232)	0.880 (0.011)	0.000 (0.144)	0.922 (0.012)	0.000 (0.222)	0.970 (0.003)
	Slow	R	-0.028 (0.187)	0.429 (0.043)	0.000 (0.096)	0.645 (0.139)	0.000 (0.149)	0.971 (0.004)
		P	-0.028 (0.187)	0.430 (0.045)	0.000 (0.097)	0.636 (0.148)	0.000 (0.151)	0.970 (0.004)

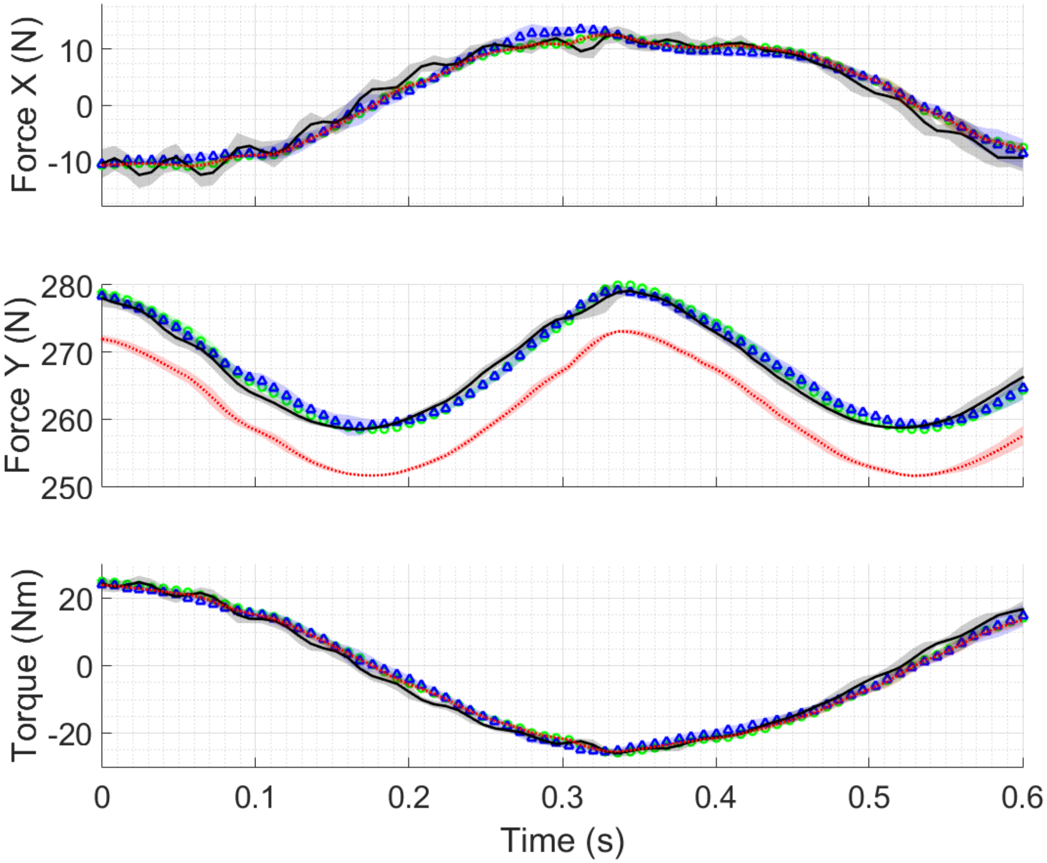

Figure 5.4: Graphs comparing the measured and recovered wrenches for fast elbow motions. All fifteen repetitions were time aligned and the mean and standard deviations found. The mean is plotted as a line, with the standard deviation as a shaded region about this line. The measured wrench is shown in black, and the recovered wrench using the Kufieta model shown in red. The wrench recovered using the robot measurements of position and velocity are shown as green circles. The wrench recovered using motion capture is shown in blue.

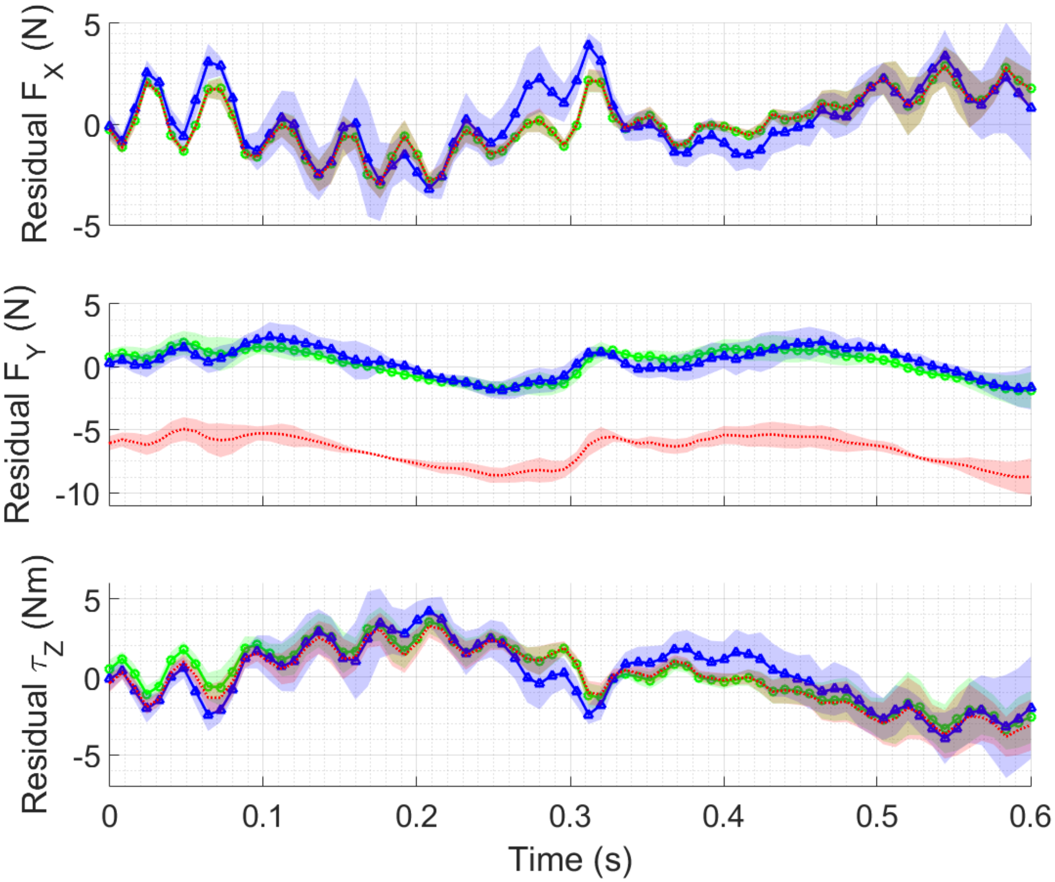

Figure 5.5: Graphs comparing the errors in the measured and recovered wrenches for fast elbow motions. All fifteen repetitions were time aligned and the mean and standard deviations found. The mean is plotted as a line, with the standard deviation as a shaded region about this line. The measured wrench is shown in black, and the recovered wrench using the Kufieta model shown in red. The wrench recovered using the robot measurements of position and velocity are shown as green circles. The wrench recovered using motion capture is shown in blue.

The recovered dynamic parameters were found to closely match those from the Kufieta model for the shoulder and elbow. This suggests that these links were suitable for dynamic parameter recovery using the proposed DIM framework. The repeatability of these results seem high, with small standard deviations.

The good match in the dynamic parameters led to low recovered torque error, with r^2 values exceeding 97%. It was found that the torque error from the proposed framework outperformed the Kufieta model.

There is an interesting tradeoff between the my_2 and I_{ZZ2} terms for the fast and slow motions of the elbow. This may be due to changes in the excitation of the first and second mass moments, resulting in improved recovery in the fast actions. This is supported by the lower condition number in the faster actions. At lower speeds, the accelerations and velocities are less exciting, reducing the recoverability.

The performance on the wrist link was found to be lower, with poor torque recovery, and proportionally higher variations in the recovered parameters. This decrease in performance was found with both the internal measurements of joint state and the joint state recovered through the kinematic recovery process. This suggests that this is a function of the dynamics of these actions instead of resulting from a kinematic error. These errors could arise from the relatively low mass and inertia of the wrist link, resulting in a poor signal to noise ratio and therefore poor recovery.

A comparison of the full kinematic state using the robotic state measurements and motion capture are shown in Table 5.3 compared to the conventional filter/differentiate method. From this table, it was found that there was good agreement between the recovered state derivatives.

The residuals of the contact wrench are shown in Table 5.4. These residual values were found to be low for the shoulder, elbow, and the fast wrist experiments. The slow wrist experiments were found to be significantly different in the X and Y directions. This poor fit agrees with the poor dynamic fit for the slow wrist actions. The seemingly good fit for the fast wrist case is problematic, as there is no indication that the associated dynamic parameters are inaccurate.

The Kufieta model was found to closely match the observed wrench, with the exception of the Y force. This offset is likely caused by an incorrect mass of the stationary base link which was not included in their analysis.

Figures 5.4 and 5.5 show the recovered contact wrench for the fast elbow experiments. These figures show the accuracy and repeatability of the dynamic recovery method. The recovery from the motion capture appears to have the largest standard deviation, but closely tracks the mean trajectory of the other algorithms. The Y offset of the Kufieta can be clearly seen, with the trajectory being offset by approximately 5N.

5.5 Guidelines for Dynamic Modelling

When performing dynamic analysis, an investigator has relatively few observables to determine the performance of the recovery process. The results for the wrist joint shown in Section 5.4.2 showed that while there can be small errors in the joint state and contact wrench, the recovered dynamic parameters can be inaccurate. The experimental data from the UR5 robot experiments were altered in post to investigate the effect common errors in experimental procedure have on the DIM process, and to allow for understanding of the residuals and r^2 values from the DIM process.

Three state recovery methods were examined, the proposed UKF method, the common differentiation/filtering method, and fitting then differentiating a spline. The effects these methods have on the condition number and recovered dynamic parameters was examined (Tables 5.5 and 5.6).

Additive noise was added to the joint states and wrench components to determine the effect that these errors have on the recovered dynamic parameters. The effect of a time offset between the kinematic and dynamic dataset was also simulated to determine the effect on the recovered parameters.

5.5.1 Results

The differences between the proposed UKF method and the differentiation/filtering method, and the spline fit method are shown in Tables 5.5 and 5.6, with the accelerations for a representative trial shown in Figure 5.6.

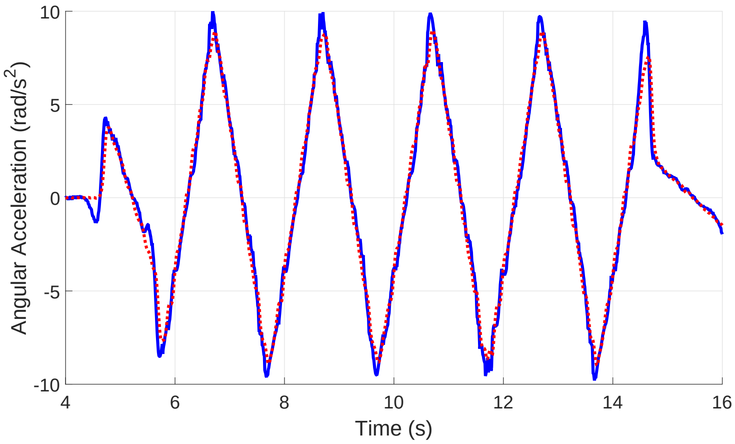

Figure 5.6: Graph comparing the estimated angular acceleration for a single trial of a fast rotation about the elbow joint. The UKF estimate from the observed angular position and velocity is shown as a solid blue line. The estimate recovered by filtering, differentiating, and filtering the measured angular velocity is shown as a dotted red line.

Table 5.5: Results of the dynamic model recovery process for three joints at two speeds using different methods for recovering the kinematic state. Mean values shown with standard deviation in parenthesis. Reference model from [67].

				$m_1 + m_2$	$mx_1 + T_x m_2$	mx_2	my_2	I_{ZZ2}	ϵ_τ	
Joint	Speed	Obs	Cond	kg	$kg \cdot m$	$kg \cdot m$	$kg \cdot m$	$kg \cdot m^2$	$N \cdot m$	r^2
Sho.	Slow.	UKF	22.615 (0.410)	27.327 (0.005)	0.078 (0.008)	-0.059 (0.010)	5.837 (0.029)	3.413 (0.112)	-0.485 (1.967)	0.994 (0.000)
		Diff.	25.331 (0.476)	27.334 (0.006)	0.068 (0.014)	-0.047 (0.017)	5.844 (0.034)	3.544 (0.148)	-0.382 (2.097)	0.994 (0.000)
		Spline	51.267 (3.362)	27.336 (0.005)	0.112 (0.062)	-0.095 (0.086)	6.773 (0.014)	1.748 (0.054)	-0.828 (2.479)	0.991 (0.001)
Elb.	Fast	UKF	5.056 (0.106)	27.315 (0.005)	0.034 (0.007)	0.005 (0.010)	1.675 (0.016)	0.766 (0.010)	-0.033 (1.572)	0.974 (0.008)
		Diff.	4.982 (0.104)	27.342 (0.003)	0.031 (0.002)	0.005 (0.003)	1.792 (0.012)	0.799 (0.002)	-0.004 (1.492)	0.977 (0.004)
		Spline	47.653 (20.157)	27.347 (0.012)	-0.025 (0.019)	0.002 (0.023)	3.460 (0.054)	0.869 (0.013)	0.483 (3.600)	0.862 (0.013)
	Slow	UKF	25.293 (0.675)	27.347 (0.002)	0.029 (0.003)	0.002 (0.004)	1.850 (0.011)	0.516 (0.059)	-0.013 (1.063)	0.983 (0.001)
		Diff.	28.708 (0.876)	27.349 (0.002)	0.025 (0.004)	0.007 (0.004)	1.849 (0.010)	0.578 (0.042)	-0.013 (1.063)	0.983 (0.001)
		Spline	46.954 (21.347)	27.351 (0.005)	0.065 (0.034)	-0.044 (0.040)	2.176 (0.019)	0.555 (0.013)	-0.369 (1.096)	0.980 (0.003)

Table 5.6: Results of the dynamic model recovery process for three joints at two speeds using different methods for recovering the kinematic state. Mean values shown with standard deviation in parenthesis. Reference model from [67].

				$m_1 + m_2$	$mx_1 + T_x m_2$	mx_2	my_2	I_{ZZ2}	ϵ_τ	
Joint	Speed	Obs	Cond	kg	$kg \cdot m$	$kg \cdot m$	$kg \cdot m$	$kg \cdot m^2$	$N \cdot m$	r^2
Wri.	Fast	UKF	5.056 (0.106)	27.346 (0.002)	0.036 (0.001)	0.000 (0.000)	0.134 (0.000)	0.034 (0.000)	0.045 (0.399)	0.535 (0.001)
		Diff.	5.742 (0.120)	27.349 (0.002)	0.036 (0.001)	0.000 (0.000)	0.142 (0.000)	0.036 (0.000)	0.048 (0.414)	0.498 (0.002)
		Spline	54.089 (2.475)	27.348 (0.002)	0.024 (0.004)	0.008 (0.005)	0.292 (0.000)	0.075 (0.001)	0.045 (0.399)	0.535 (0.001)
	Slow	UKF	25.943 (1.094)	27.346 (0.004)	0.032 (0.001)	0.003 (0.002)	0.145 (0.000)	0.037 (0.000)	0.045 (0.311)	0.651 (0.014)
		Diff.	29.128 (1.522)	27.347 (0.004)	0.031 (0.001)	0.003 (0.002)	0.146 (0.000)	0.037 (0.001)	0.049 (0.314)	0.644 (0.015)
		Spline	29.140 (2.947)	27.347 (0.004)	0.032 (0.002)	0.002 (0.003)	0.178 (0.002)	0.045 (0.001)	0.040 (0.372)	0.507 (0.014)

5.5.2 Discussion

Figure 5.6 shows an important difference between the artefacts that arise from the UKF and differentiation/filtering methods. As the UKF method adheres to the dynamics of the system, there is a lead/lag effect. As each successive state is sampled, the filter balances the potential change in the state value to the potential errors in the observations. The differentiation/filtering method in comparison can result in undershoot during sudden changes in state. This is seen in the peaks of the differentiation method always being smaller than that of the UKF method.

The differences between the proposed UKF method and the differentiation/filtering method, and the spline fit method are shown in Tables 5.5 and 5.6. Comparable performances were found between the UKF and differentiation/filtering methods, with a slight improvement in performance in the wrist experiments. This suggests that there is good agreement between these methods and that the effects seen in Figure 5.6 were negligible. It is important to note, that while the derivatives were found via differentiation/filtering in the *Diff* trials, the initial angular positions were found through the proposed UKF method. If this method was not chosen, an alternative method for converting motion capture markers to joint positions would have been used, which may have resulted in inferior performance, a source of error explored in Section 5.5.2.2.

Changes were also made to the UKF model parameters, the recovered position and wrench measurements, and the temporal alignment between the kinematic and dynamic data.

5.5.2.1 UKF Parameters

The UKF used in the proposed framework used a process and observation noise of $1 \times 10^2 rad/s^4$ and $1 \times 10^{-3} m$ respectively and were based on estimates from differentiation/filtering and the published accuracy of the motion capture system. These values were swept through a range of magnitudes to determine the sensitivity of these parameters on the system, with the process model noise varying from 1×10^1 to 1×10^4, and the observation noise varying from 1×10^{-4} to 1×10^{-1}. These perturbations were not found to vary the kinematic state significantly, with changes in r^2 values of under 1%. The most significant variation occurred when the UKF process model over-constrained (1×10^1) and the observations error set high (1×10^{-1}). This led to a decrease in acceleration accuracy of 8.7% for fast elbow motion (3% in other cases). This is likely caused by the introduction of significant lag in the system which became more pronounced in the fast elbow experiments.

5.5.2.2 Angular Noise

The recovered joint angles were injected with Gaussian noise with means of 0.01 to 0.1 radians, and standard deviations of 0.001 to 0.01 radians. The effect of a mean offset in the angles, was a counter rotation in the dynamic parameters, with the mx_2 and my_2 values shifting to compensate for this change. The addition of noise to the angular measurements substantially affected the recovered kinematic state, and dynamic parameters. This could be compensated through tuning of the UKF model, however there is a trade-off between the lag in the filter, and the accuracy of the recovered states.

5.5.2.3 Temporal Offset

Simulated lead/lags between the kinematic states and contact wrench of 0.001 to 0.1 seconds were introduced. It was found that a temporal misalignment of under 0.01 seconds had a negligible variation on the recovered dynamic parameters (under 0.5%). This increased to approximately 10% for a lead/lag of 0.1 seconds.

5.5.2.4 Contact Wrench Noise

Gaussian noise was also artificially added to the contact wrench with means of 0.1 to 10 and standard deviations of 0.01 to 1 for both the linear forces (N) and torques (Nm).

The addition of linear noise in the X direction was found to be rejected by the recovery process, with little change to the recovered dynamic parameters. This is likely due to the system dynamics closely coupling the X force to the other observable components of the contact wrench, reducing the effect of this error.

Addition of noise to the Y direction had two different effects on the recovered dynamic parameters. A mean offset resulted in a change in the first dynamic parameter, the grouped total mass $m_1 + m_2$ of the system. As a mean offset is indistinguishable from the base mass m_1, this is absorbed into this first parameter, making its effect undetectable. While this is problematic for recovering the full model, only the first parameter is affected, resulting in negligible change in the excited link. Noise of up to 1N in the linear direction had a negligible change to the recovered dynamic parameters.

The addition of a mean torque error had a similar effect as the linear Y case, with the second dynamic parameter $mx_1 + T_x m_2$ absorbing the offset. Noise with a standard deviation of up to 1 Nm was found to have a negligible change to the recovered dynamic parameters.

5.6 Conclusion

These robotic tests show the potential of these methods to recover the dynamic parameters of a system. In this simple system, the dynamic parameters were found accurately and precisely for the shoulder and elbow without the use of a reference model when performing the DIM optimisation. The model was found to closely match the Kufieta model, with the r^2 values for the recovered contact wrench and internal torques reporting a better fit when using the recovered models. This suggests that the proposed kinematic/dynamic recovery framework has potential for the study of biological systems.

The kinematic recovery process was found to have a sub-millimetre accuracy, and a precision of approximately 2 mm for the robotic system. The most significant variations were found based on the visibility of the markers and the magnitude of Cartesian displacement in their movements.

While the dynamic recovery process was successful in the majority of cases, there are a number of important lessons from these robot experiments. The recovery process requires sufficient excitation for a recovery of the dynamic parameters. This is not simply a function of the kinematic actions (which result in a low condition number), but also the relative magnitudes of the dynamic parameters. The wrist of the UR5 was found to have insufficient mass/inertia to allow for recovery.

There were also two interactions seen in the recovery of the dynamic parameters. Differences in the recovered kinematic models were found to result in offsets in the dynamic parameters. An angular offset was found to cause the relative weightings of the first mass moment terms to rebalance. This results in the norm of the first mass moment to be the same, but the direction to be offset by the angular displacement.

A dynamic interplay was also found between the first and second mass moments. Based on the speed of the observed motion, a bias towards the first or second mass moment could be seen. To minimise this effect, constant velocity actions and exciting actions should be performed to decouple these parameters.

Chapter 6

Clinical Applications

The methods outlined in Chapters 3, 4, and 5 were extended to the five-times sit-to-stand protocol, an assessment measure used clinically to evaluate balance and stability. This Chapter attempts to *augment* an existing clinical test, keeping the same experimental protocol, but attempting to recover additional metrics on an individual's performance. Emphasis is placed on developing a rapid system that could be deployed in a clinical setting, prioritising reductions in the setup and protocol time, and robustness to experimenter error.

Section 6.1 outlines the background of the sit-to-stand protocol and its uses in clinics. The experimental protocols used to collect data are explored in Section 6.2, with the kinematic and dynamic analysis explored further in Sections 6.3 and 6.4. The feasibility of these methods to augment existing clinical measures is then explored in Section 6.5.

6.1 Sit-to-Stand

The sit-to-stand action was chosen for investigation due to the need for an improved method of modelling an individuals stability, the expected kinematic and dynamic excitation of the action, and the relatively simple serial chain structure of the action. The Centers for Disease Control and Prevention in the United States reports an incidence of fall-related hospitalisations of 700,000 per year[21]. These falls are the most common cause of traumatic brain injury in the US, and have an associated direct medical cost of approximately $34 billion annually.

There a number of methods that have been used to evaluate an individual's mobility and stability. The most commonly used methods are timed action methods such as the five-times sit-to-stand[134] and point-score methods such as the Berg balance score[12]. These methods estimate an individual's abilities based on the time taken to complete a given action, or via similar thresholding based methods.

There are a number of model based approaches that can be used, that simplify the body to a single, telescoping single, or double pendulæ[40][100][101]. While these methods look at the dynamics of the system, the conversion of motion capture data taken from a sit-to-stand action to the motions of a pendulum may not be readily apparent. Similarly, the dynamics of the situation requires knowledge of the dynamic parameters of the individual to determine an individual's stability. These challenges have led to poor success in translating these methods into a discriminator between stable and unstable individuals[4][113][122].

6.2 Method

Ten healthy subjects aged 26.3 ± 4.1 years old, mass 66.6 ± 7.7kg, and 1.71 ± 0.09m were recruited under UCB IRB 2015-07-7767. The height and mass of every subject was recorded and used to calculate an estimate of the segment lengths, masses, and inertias using the allometric scaling relationships based on sex and ethnicity[136]. In cases where individuals did not fit into the categorisation, the results from all applicable categories were taken and averaged.

An ultrasound device[147] was used to determine the locations of the lateral and medial malleolus, apex of the fibula and medial condyles. These bone landmarks were then used to estimate four functional segment lengths for the individual's shank and thigh[29].

Figure 6.1 shows the experimental setup. A motion capture suit was worn by the subject, with forty-three active markers placed on the subject's limb segments (Figure 6.4). Seven motion capture markers were placed on the base of the force platform to allow for calibration between the force platform and motion capture coordinate frames. An adjustable stool was provided for subjects to sit on. The height of the stool was set so that the subject's thighs were parallel to the ground.

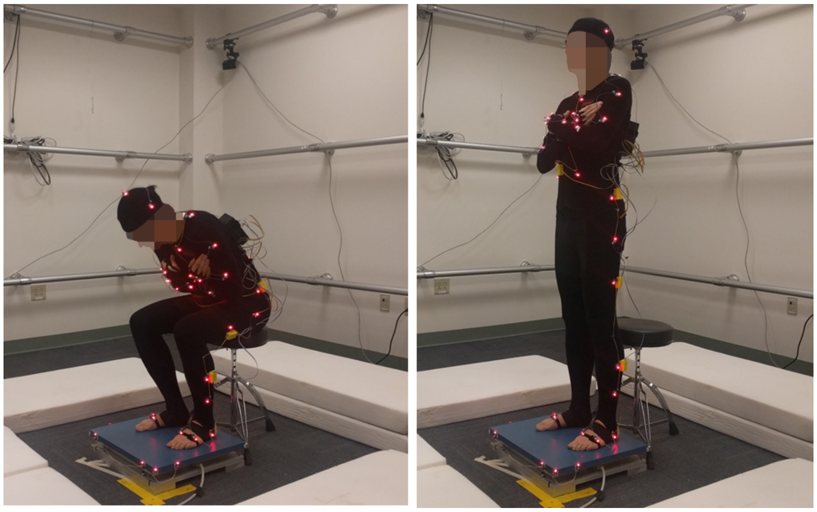

Figure 6.1: Subject in the seated and standing phases. Subject is wearing a motion capture suit with active markers placed on limb segments. Force platform is visible underneath the subject. Adjustable stool is shown. Mattresses are placed around the subject in case of falls.

Subjects were asked to stand five times in a row with their arms crossed in front of them using three different strategies[3][9][55]. The first strategy was their normal standing action. Subjects were told to stand five times in a row with no additional prompts. The second strategy was a *dynamic* standing action. Subjects were shown a video demonstrating a momentum transfer strategy for standing- swinging the torso rapidly to move off the chair. The third strategy was a *stable* standing, where subjects were asked to stand such that they could stop at any point during the standing action.

Motion capture was recorded at 480Hz, and force platform data at 2.4kHz. The order of experiments was not randomised to avoid the normal action being *primed* by the other two standing methods.

6.3 Kinematic Recovery

The observed motion capture data was processed using the proposed kinematic framework. The two markers at the ankles were used to assist in the recovery of the ankle position due to the small rotation about the ankle during the sit-to-stand action. The results of the recovery process are shown in Section 6.3.1, and are discussed in Section 6.3.2.

6.3.1 Results

The results of the kinematic recovery process are shown in Figure 6.2 for a representative subject and trial. Each of the intermediary steps in the kinematic recovery process are shown in Figure 6.3. The marker transformation, circle fitting, and state recovery processes are shown for the recovery of the shank, thigh, and torso segments. Figure 6.5 compares the recovered skeleton and joint states between the proposed framework and the commercial recovery process.

Table 6.1 compares the recovered limb lengths using the anatomical *landmark* method, the proposed *framework*, and allometric scaling of an individual's *stature*. The landmark method is used as the ground truth. Table 6.2 compares the recovered skeletal lengths under the three different standing strategies.

Table 6.1: Errors in recovered kinematic parameters and marker re-projection for healthy sit-to-stand actions. The percentage difference between the means of each method and *landmark* method are shown. The standard deviation of each method is shown in parenthesis.

Method	Landmark	Framework	Stature
$\epsilon_{l_{shank}}$ (%)	- ± 4.8	-0.4±2.8	-6.0±2.9
$\epsilon_{l_{thigh}}$ (%)	- ± 4.5	3.2±5.3	-6.5±3.0

Table 6.2: Errors in recovered kinematic parameters and marker re-projection for the three different sit-to-stand strategies for healthy subjects. Mean values shown with standard deviation in parenthesis.

Action	Dynamic	Normal	Stable
$\epsilon_{l_{shank}}$ (%)	-0.2 (4.2)	1.0 (3.7)	0.3 (4.0)
$\epsilon_{l_{thigh}}$ (%)	-3.9 (5.4)	-4.3 (5.7)	-1.3 (3.6)
ϵ_M (mm)	4.3 (2.4)	5.2 (4.1)	3.8 (2.8)

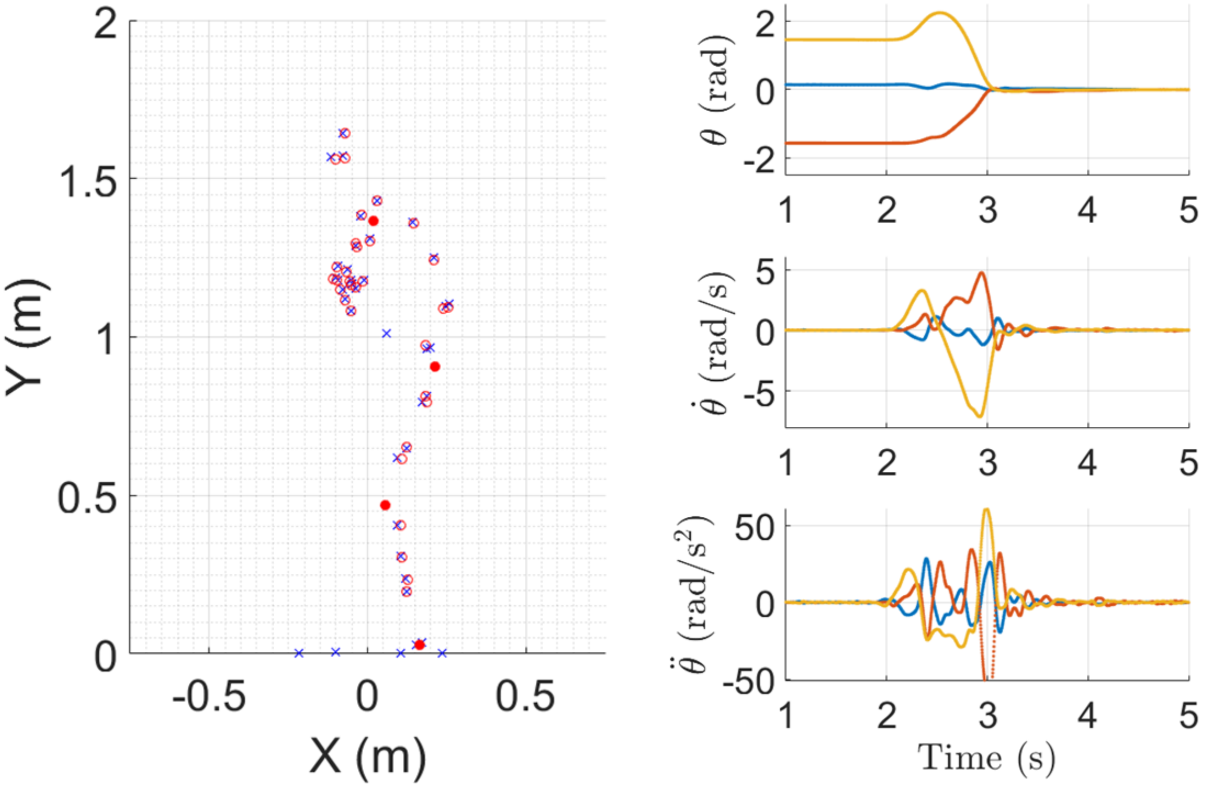

Figure 6.2: Results of the kinematic recovery process. Left: Recovered kinematic skeleton as seen in the sagittal plane. Blue true marker locations at a particular frame. Red filled circles model joint centres. Red empty circles estimated marker locations based on recovered kinematic model and states. Right: Recovered joint state trajectories. Ankle, knee, and hip joints are shown in blue, red, and yellow respectively.

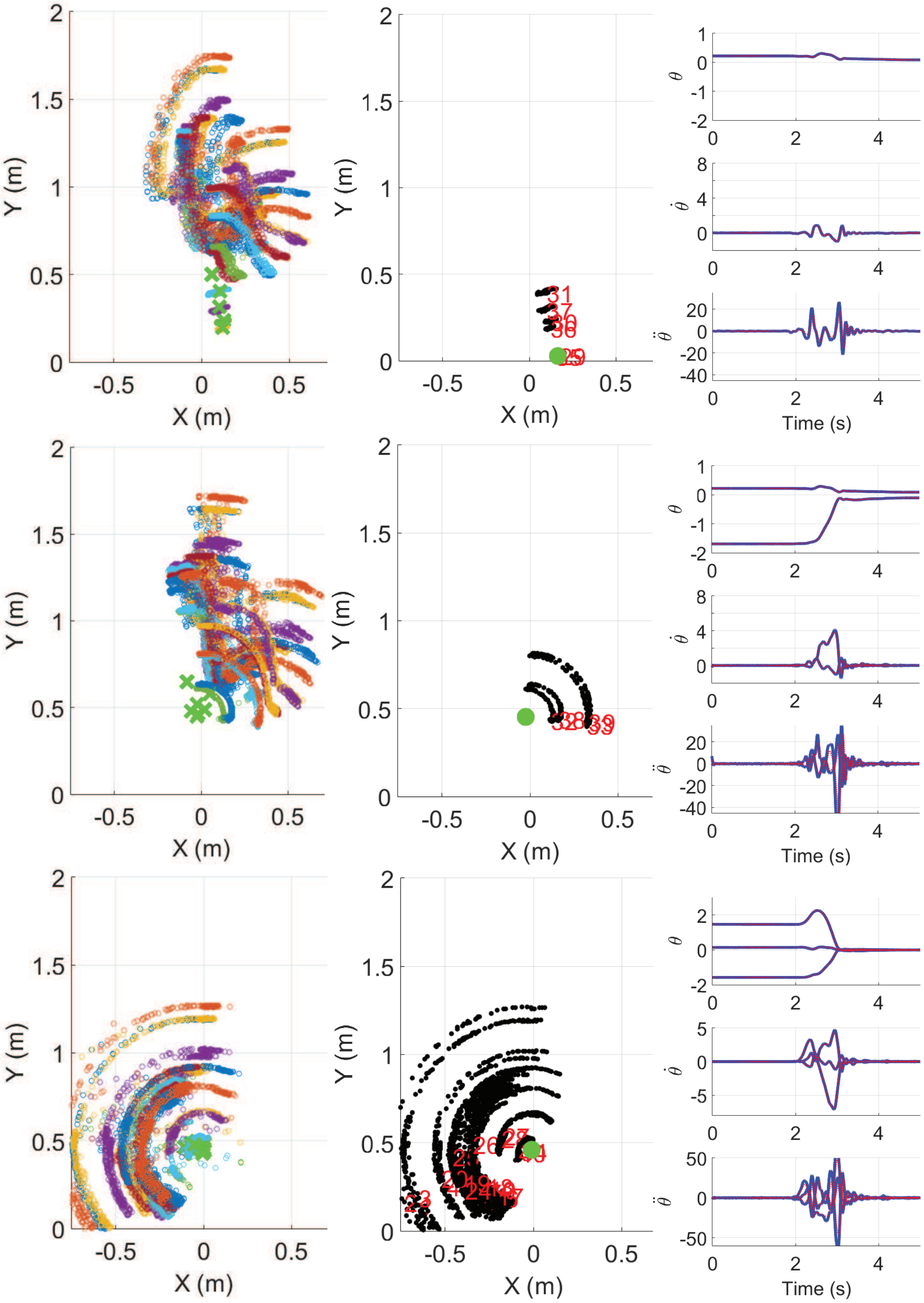

Figure 6.3: Stages in the kinematic recovery process for the sit-to-stand actions for a representative subject. Rows: Top to bottom: recovery of the second, third, and fourth kinematic segments. Columns: Recovery stages. Left: Motion capture markers remapped to local coordinate frame. Markers with valid circle centres shown as green crosses. Centre: Segment kinematic parametrisation. Localised markers are shown along with recovered joint centre. Right: Recovered state trajectories. Units are rad, rad/s, and rad/s^2.

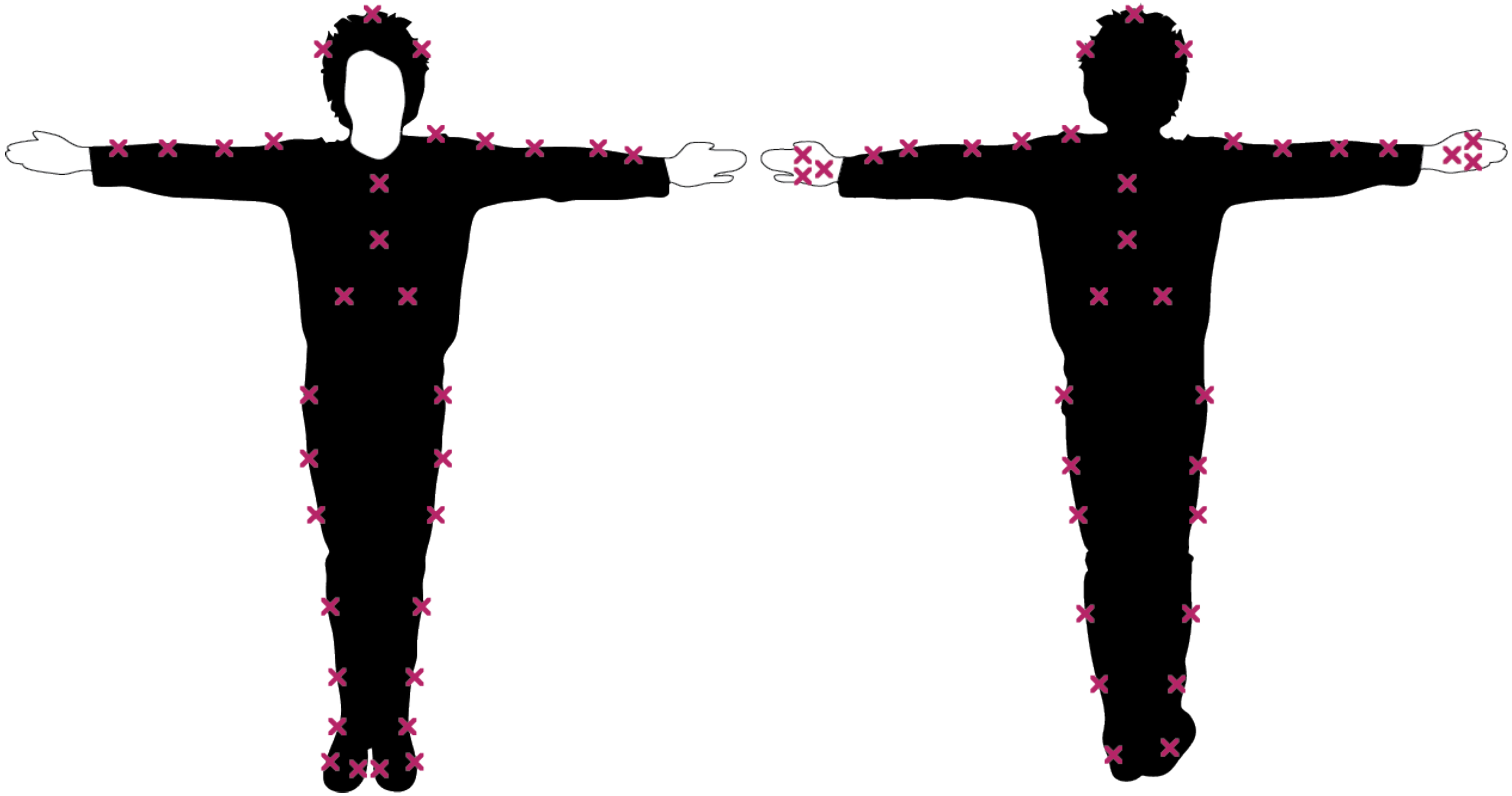

Figure 6.4: Cartoon of the active motion capture marker locations. Three markers are located on the top, left and right sides of the head. A single marker is located at the top of the left shoulder, with two markers on the upper and lower arms. Three markers are locates on the back of each hand. Four markers are placed on the clavicle, solar-plexus, and at the base of the ribcage. A marker are placed on either side of the hi pat the anterior superior iliac spine. Two markers are placed on the thigh and shank. A single marker is placed on the lateral malleous. Two markers are then placed on the foot near the proximal phalanges of the little and big toe.

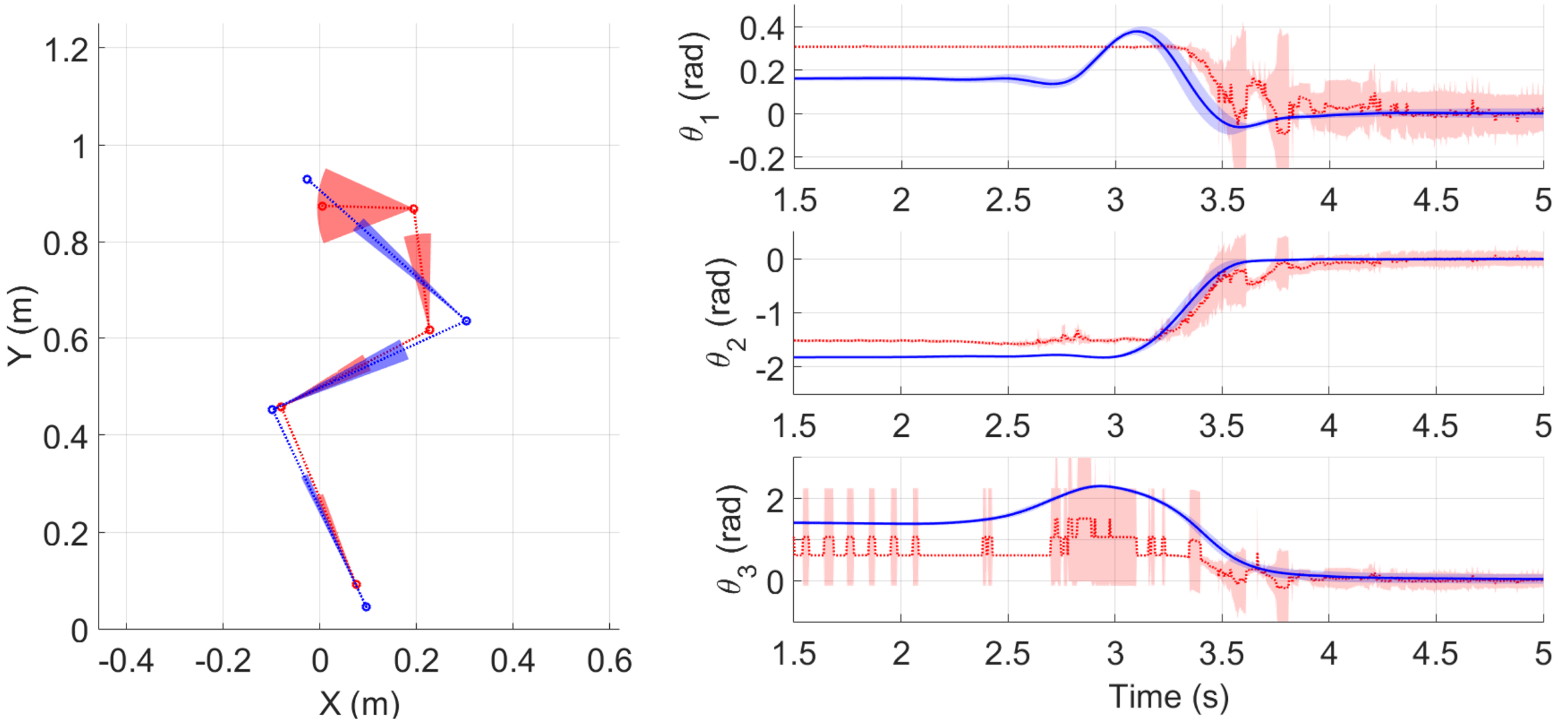

Figure 6.5: Comparison of proposed kinematic recovery framework (blue), and commercial motion capture system (red). Five sit to stand actions are averaged, with the mean shown as the solid line, and the standard deviation shown as the shaded region. Left: Skeleton showing joint positions and limb segments. Arc shows the variation in joint angle for that phase of the sit-to-stand. Right: State Trajectories for joint angles

6.3.2 Discussion

Table 6.1 compares the performance of the proposed recovery method to the height scaling and landmark methods. The height scaling method was chosen as it is frequently used to obtain limb length estimates in subjects with minimal additional measures being taken. The landmark method was chosen due to the accuracy of the recovered joint positions. These two methods were compared to the models recovered from the proposed framework, operating on approximately 30 seconds of experimental data per subject per standing strategy.

Table 6.1 shows good agreement between the proposed framework and the landmark method, and offers improved precision over the stature based scaling. The accuracy of proposed framework was found comparable to the other methods. The short duration of the experiment and the simplicity to perform makes this method a potential *augmentation* of the existing sit-to-stand action, providing an additional measurement of the limb lengths without requiring additional actions to be performed.

Table 6.2 compares the recovered skeletal parameters under the different standing strategies. The shank length was found consistently regardless of action, suggesting that the action is sufficiently kinematically exciting for recovery. The thigh length was found to be more variable, with the faster mean error for the dynamic and normal actions being smaller than expected. This reduction in functional thigh length could be due to the motion of the torso being a combination of spine and hip motion. This variation may also explain the corresponding increase in marker error for the dynamic and normal actions.

A comparison between the commercially recovered skeleton and states and the proposed recovery framework is shown in Figure 6.5. These figures show that the commercial skeletonisation shows significant chattering in the recovery process, resulting in sudden jumps in the mean trajectory, and a significant spread in the standard deviation. This irregularity is likely due to markers on the body becoming occluded in the initial part of the sit to stand action. In the commercial recovery process, the subject stands in a T-pose, and rotates each joint in sequence. The local coordinates of the joint are then assigned based on the motion of the markers. When the individual performs the sit to stand action, the motion capture suit shifts on the skin, changing the local coordinates. During the rapid movement in the sit to stand action, the motion capture markers on the torso and arms may be occluded by the flexion of the torso. As the commercial skeleton is for the full body, this leads to an ill-posed recovery process, leading to significant joint errors. This can be seen in the improbable spine angle, and the chattering in the states process suggesting instability in the inverse kinematic problem.

While these differences were seen between the dynamic and normal strategies when compared to the stable strategy, the absolute length difference between the actions was under 2mm. This suggests that the proposed framework is suitable for recovery of the kinematic states and parameters for a system.

6.4 Dynamic Recovery

The dynamic recovery process was then applied to the recovered kinematic skeleton. Only the F_Y and τ_Z components of the wrench were used in this recovery process. These two components were chosen as they are the only two contact dynamic forces required for estimation of the *Centre of Pressure* (CoP), one of the clinically relevant measures for assessing stability.

Due to the contact forces when the subject was seated, the DIM process was performed on data where the knee angle rose above -0.8 radians. This threshold was used to ensure that the subject was no longer in contact with the chair, but was still in a dynamically exciting part of the standing action.

In contrast to the robot experiments, a reference model was used in the recovery process. This model was based on an allometric model[136] and was scaled to each individual using their mass and height measurements.

The dynamic model used for the DIM recovery process is shown in Figure 6.6. Of the full vector of sixteen dynamic parameters, eleven regrouped parameters were found. The symbolic form of these base parameters $\boldsymbol{\phi}_b$ are shown in Equation 6.1. It can be seen that the base parameters are dependent on the local coordinates of the joints $\boldsymbol{p}_2, \boldsymbol{p}_3, \boldsymbol{p}_4$.

$$\boldsymbol{\phi}_b = \begin{bmatrix} m_1 + m_2 + m_3 + m_4 \\ mx_1 + p_{2,x}\left(m_2 + m_3 + m_4\right) \\ mx_2 + p_{3,x}\left(m_3 + m_4\right) \\ my_2 + p_{3,y}\left(m_3 + m_4\right) \\ I_2 + \left(p_{3,x}^2 + p_{3,y}^2\right)\left(m_3 + m_4\right) \\ mx_3 + p_{4,x}m_4 \\ my_3 + p_{4,y}m_4 \\ I_3 + (p_{4,x}^2 + p_{4,y}^2)m_4 \\ mx_4 \\ my_4 \\ I_4 \end{bmatrix} \tag{6.1}$$

The recovered DIM and torque models were found to contain different subsets of dynamic parameters. While this would ordinarily result in a problem for torque recovery, the recovered point mass grid was used to recover an estimate of the full dynamic parameters $\boldsymbol{\phi}_F$. The full parameter vector was then used to recover the joint torques.

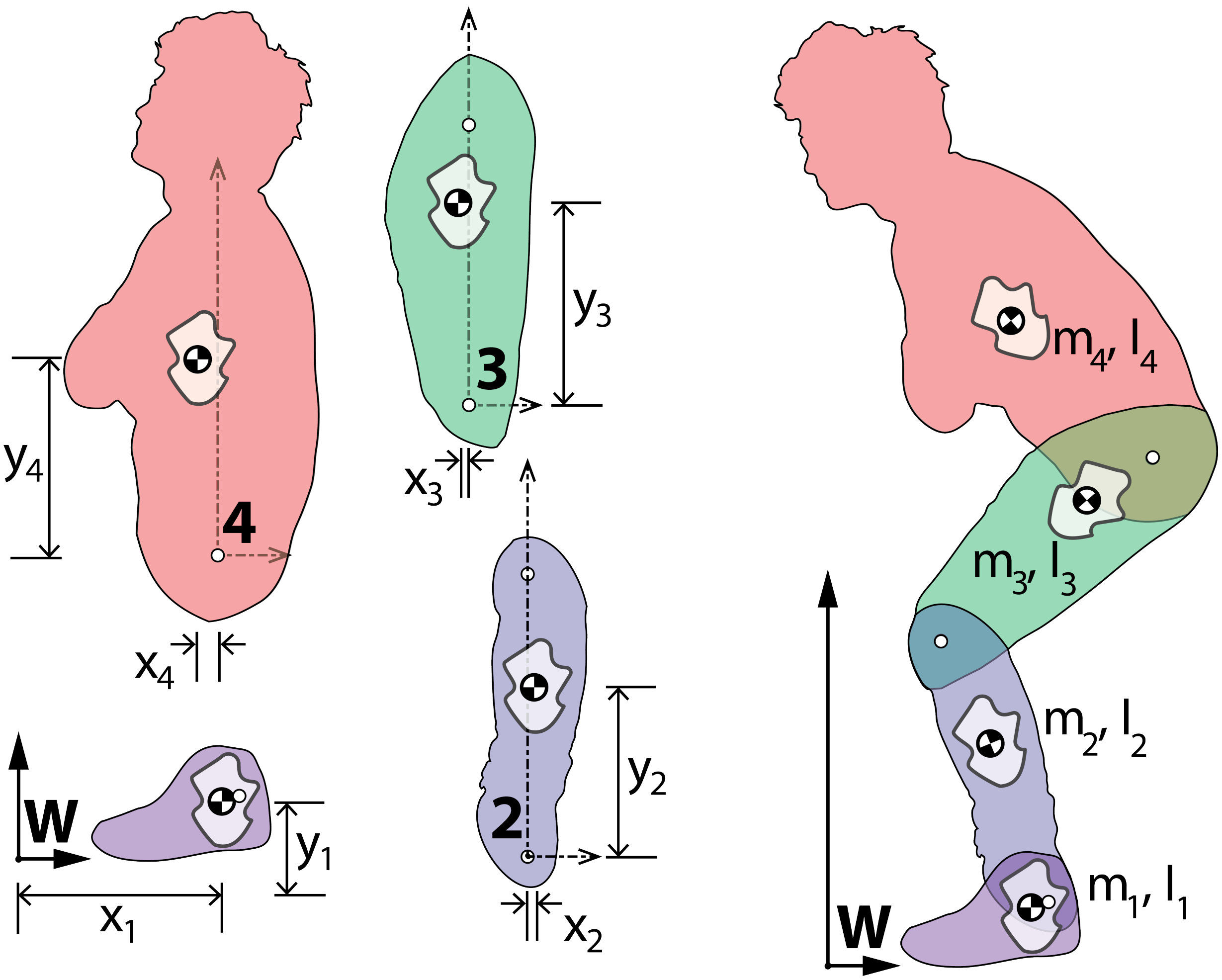

Figure 6.6: Labelling convention for the DIM recovery process. Coordinate frames are defined by the kinematic recovery process. The four limb segments are shown, each with the notation for their zeroth, first, and second mass moments of inertia.

6.4.1 Results

Figure 6.7 shows a comparison in the expected contact wrench between the models recovered under the different strategies, and the allometric scaled model. The correspondence between the contact wrench components and the CoP is also shown.

The variation between the recovered dynamic models for each standing strategy is shown in Figure 6.8. The base parameters are shown on the left with a modified set shown on the right. The modified set reduces the effect of changes in the system coordinate frames by modelling the mx_i my_i components as a single inertial parameter mr_i. This decreases the sensitivity to small variations in mx_i values which are relatively small.

A heat-map of the recovered point mass grid is shown in Figure 6.9. The weightings of each node is shown with more massive points resulting in a brighter coloured face.

A summary of the recovered models is shown in Table 6.3 comparing the recovered wrench, COP for each model and action. The variation in the corresponding joint torques compared to the torques recovered via the model recovered via that trial is also shown.

6.4.2 Discussion

Figure 6.7 shows the estimation of the contact wrench under the proposed framework process as compared to the Winter model. From this Figure it is clear that the Winter model provides a good estimate of the F_Y forces, but fails to provide a good estimate of the reaction torques for the action. As the CoP is calculated from the F_Y and τ_Z values, this error in the torque leads to a poor estimate of the COP. By comparison, the recovered models under the *dynamic* and *normal* standing strategies provide a better torque estimate. This results in a corresponding improvement in the recovery of the CoP.

A clear difference between the estimated and measured contact forces is the effect of the contact with the chair. There is a clear transition near sample 860 in the ability of these models to fit the provided data. This is due to a transition in the contact dynamics between the individual and the chair. After sample 860, modelling the individual as a triple pendulum appears to be valid with low errors in the contact wrench. Prior to sample 860, this assumption breaks down, suggesting that the individual is still interacting with the chair. This transition aligns with the instant where the measured F_Y crosses rises past 72% of the steady state value. This agrees with the sit-to-stand model presented by Etnyre[35], suggesting that the modelling method is able to provide a dynamic basis for the transition between the seated and standing states.

A graphical description of the dynamic model parameters are shown in Figure 6.8. The left figure shows the coefficient of variation (COV) for the base parameters. Due to the small expected size of parameters ρ_6 and ρ_9, the COV for these parameters is large. It is likely that this is due to small changes in the coordinate frames between trials, a factor seen in the robotic experiments. To reduce this effect, the base parameters for the first mass moment can be regrouped to be acting at a single radius r_i. The COV for these modified base parameters are shown on the right. The dynamic parameters for the recovered models appear to be more self-consistent than the corresponding Winter models, with lower mean and deviation in the COV. The largest variation in COV for both the recovered and Winter models appears to be in the base parameter $\boldsymbol{\phi}_2$. Base parameter $\boldsymbol{\phi}_2$ consists of two parameters- the ankle location $p_{x,2}$ and the first mass moment of the foot mx_1. While the ankle position is measured and tracked between trials, the dynamic parameters of the foot are taken to be relative to the force platform, with the ankle and more distal segments floating about the force platform. This variation in the COV of $\boldsymbol{\phi}_2$ could be an indicator that the subject is standing on a different part of the force platform, resulting in an increased COV. The kinematic position of the ankle was also challenging to recover due to the limited rotation of the joint. These two factors may have compounded resulting in the higher COV for $\boldsymbol{\phi}_2$.

Figure 6.9 shows the point mass grid for a representative subject for *normal* standing. This figure shows the differences in how each segment is modelled, with the foot, shank,

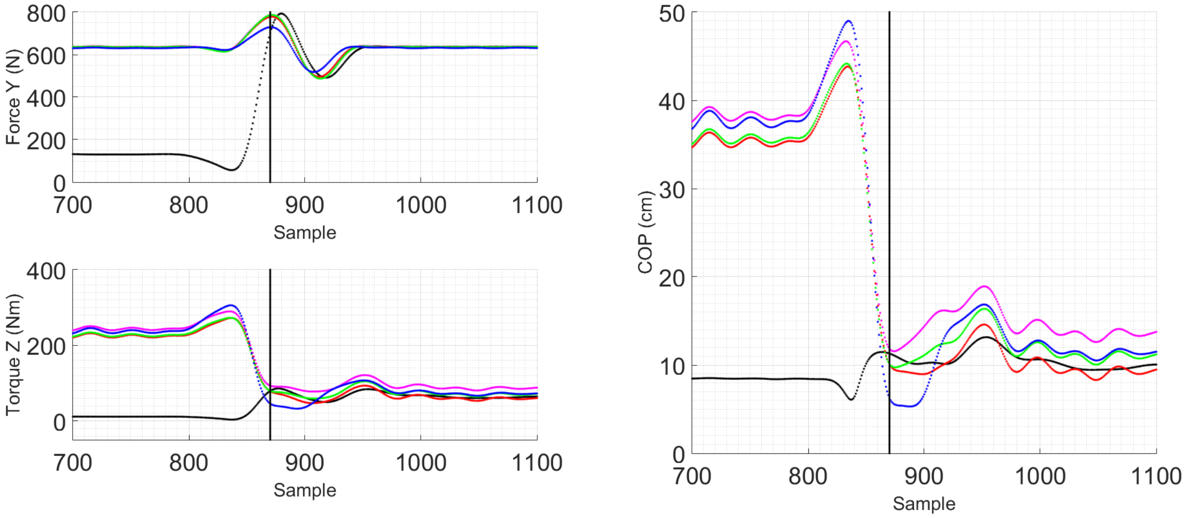

Figure 6.7: Comparison of recovered dynamic models, Winter model, and observed contact forces on the *normal* standing action. Sample 860 is marked by a vertical black line. Black: Observed wrench; magenta: Winter model; red, green, and blue: models recovered from the *dynamic*, *normal*, and *stable* datasets. Left: Comparison of contact wrench components. Right: Comparison of corresponding Centre of Pressure.

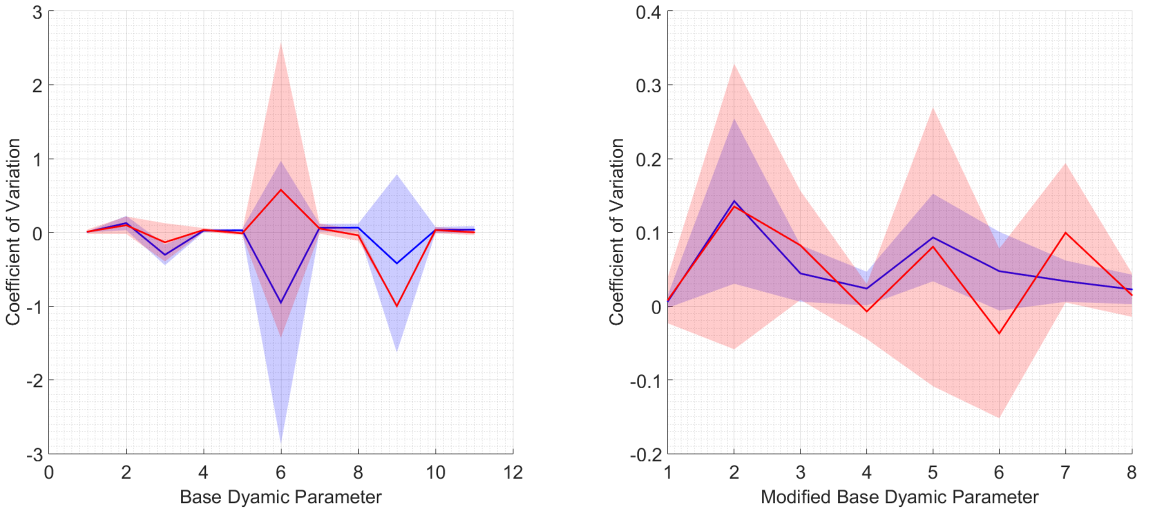

Figure 6.8: Comparison of recovered dynamic recovery framework, and expected Winter dynamic parameters (red). The mean and standard deviations of the mean recovered model is shown in blue. The variation between the recovered model and the expected Winter models are shown in red. Left: Base parameters. Right: Modified base parameters to account for rotations of segments frames.

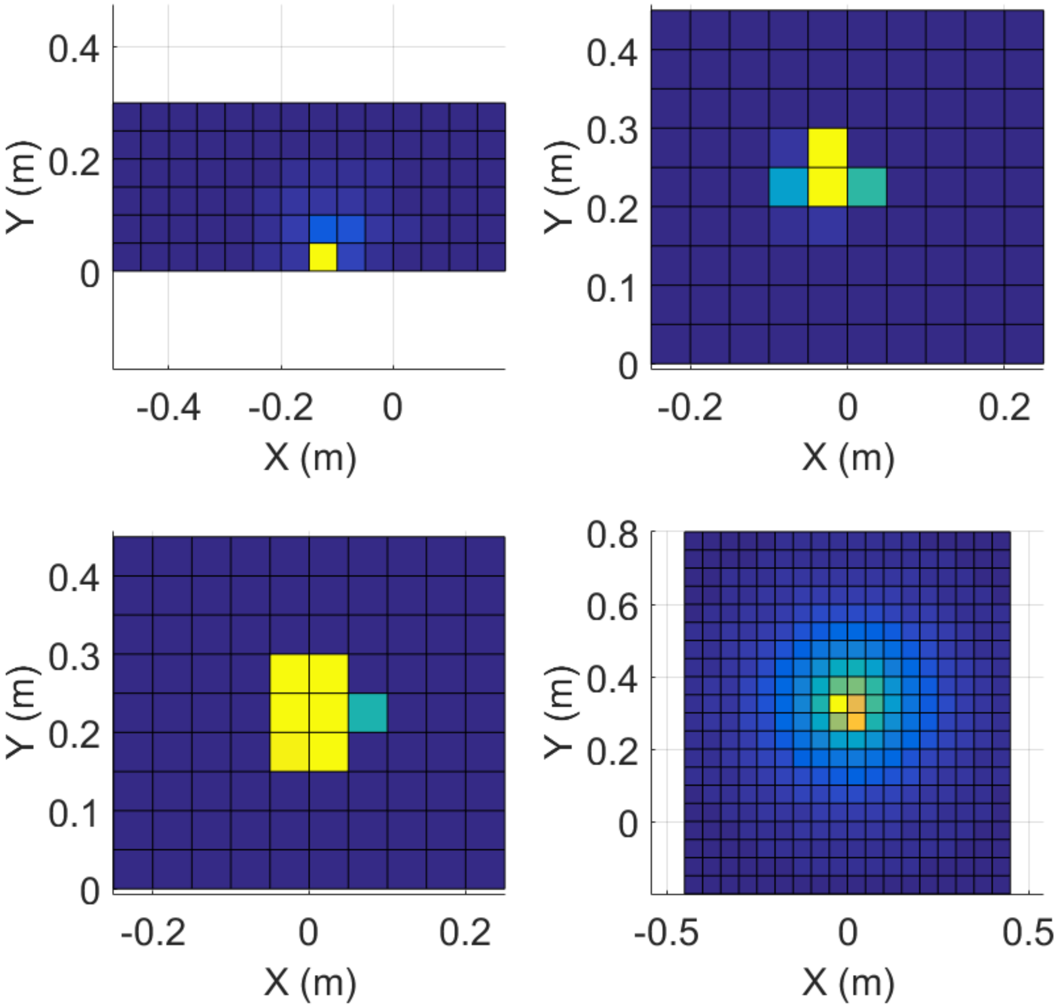

Figure 6.9: Recovered point mass grid for a representative subject. Heat map showing magnitude of masses at each point where blue to yellow shows increasing mass. Top left: Foot, top right: shank, bottom left: thigh, bottom right: torso.

Table 6.3: Comparison of recovered wrench, COP, and Torques using the different models on different recovery strategies.

Action	Cond	Model	Wrench Error		CoP Error	Torque Error		
			F_Y (N)	τ_Z (Nm)	(cm)	τ_1 (Nm)	τ_2 (Nm)	τ_3 (Nm)
Dynamic	83 ± 30	Winter	-13.4 ± 99.4	25.6 ± 21.5	3.8 ± 4.1	14.2 ± 4.3	16.4 ± 3.9	5.3 ± 3.6
		Dynamic	-16.4 ± 86.7	7.0 ± 19.5	1.2 ± 5.9	-	-	-
		Normal	-12.8 ± 91.5	32.4 ± 19.4	3.8 ± 2.7	3.0 ± 2.2	6.3 ± 2.2	1.3 ± 2.5
		Stable	-19.3 ± 99.1	33.4 ± 23.3	3.9 ± 4.2	6.7 ± 4.3	9.5 ± 4.6	4.9 ± 4.8
Normal	113 ± 57	Winter	-8.5 ± 48.2	19.9 ± 15.0	3.3 ± 1.8	11.3 ± 3.5	10.3 ± 2.7	4.4 ± 1.7
		Dynamic	-11.5 ± 42.1	-20.3 ± 15.5	-2.4 ± 2.0	-2.9 ± 1.6	-6.5 ± 1.8	-1.2 ± 1.6
		Normal	-6.9 ± 42.4	5.4 ± 13.8	0.9 ± 1.7	-	-	-
		Stable	-14.6 ± 49.7	5.8 ± 17.4	1.5 ± 2.2	3.9 ± 3.0	3.4 ± 2.9	3.8 ± 2.2
Stable	101 ± 44	Winter	8.2 ± 15.6	16.8 ± 9.2	2.4 ± 1.4	7.5 ± 2.0	7.4 ± 2.5	0.8 ± 1.8
		Dynamic	1.1 ± 15.3	-20.7 ± 9.5	-3.2 ± 1.6	-6.5 ± 2.9	-10.4 ± 4.5	-4.1 ± 3.2
		Normal	6.4 ± 15.3	5.0 ± 9.8	0.6 ± 3.6	-3.7 ± 2.6	-3.5 ± 3.5	-3.3 ± 2.2
		Stable	1.4 ± 14.7	5.5 ± 10.2	0.8 ± 2.6	-	-	-

and thigh being recovered as concentrated point masses. The torso in contrast has a wider distribution of mass points, suggesting that the inertial effects of the torso are significant. This agrees with the expected model where the inertial parameters of the torso are likely to be more significant, with the other limb segments acting closer to point masses.

Table 6.3 summarises the performance of the recovered dynamic models on the recovery of the contact wrench and CoP. The condition numbers for the three sit-to-stand strategies were found to be similar, with the dynamic standing having a slightly lower condition number. This is likely due to the larger variations in speed and acceleration during the dynamic standing action.

A threshold of -0.8 rad on the knee was used to signify the transition between sitting and standing for the analysed data. This apriori estimate was based on the prior methods of *seatoff*[35]. This threshold resulted in the wrench errors listed in Table 6.3.

The F_Y error in the dynamic case was substantial across all models, with a large standard deviation. This is likely due a combination of recoil on the force platform, and the threshold capturing part of the seated state. This results in the large errors in the F_Y state. The errors in the F_Y term seem consistent across all models, suggesting that the benefits of individualisation on the F_Y wrench estimation are negligible.

There are differences in the torque components, with the normal and stable models outperforming the dynamic and Winter models when cross-validated against stable and normal standing. The dynamic models were found to be good for the dynamic action specifically, with poor performance for the other standing strategies. The Winter model was found to give poor estimates of joint torque in all cases.

As the CoP is a combination of the vertical force and the torque, the decreased performance of the estimated torques of the Winter model led to less precise estimates of the CoP when compared to the normal and stable models. This suggests that individualisation is important for estimation of CoP. The poor performance of the dynamic model for the other CoP estimates may be due to the dynamic standing action causing excitation of a different subset of inertial parameters. While this leads to improved performance in dynamic actions, the model is not valid for less intense standing actions.

An interesting result of this analysis is the low variations in the estimated joint torques when using the proposed dynamic recovery framework. While the models have similar performance in recovering the hip torque τ_3, the performance on the ankle and knee torques are different. The cause for this dissimilarity is unclear. The proposed recovery method may be providing an improved torque estimate when compared to the Winter model. The improved contact torque adds credibility to this hypothesis as the torque transmitted to the base is a function of the other torques operating in the system, and the accuracy and precision of the torque recovery in the robot case.

The counterpoint to this would be the manner the recovered torques were generated. The torque recovery process required knowledge of the full dynamic parameter vector $\boldsymbol{\phi}_F$, while only the base parameters $\boldsymbol{\phi}_b$ have an effect on the regressor. While the physical consistency step provides an estimator of the full parameters $\boldsymbol{\phi}_F$, this method has not been validated separately. The similarity in the recovered joint torques could be the result of a null-space arising in the optimisation process. There also may be poor recovery of the thigh and shank parameters due to dynamic domination by the torso. Further investigation on these effects needs to be performed to determine this discrepancy in the recovered torques.

6.5 Conclusion

This chapter has demonstrated the application of the proposed individualised modelling framework to an individual performing a sit-to-stand action. The standard sit-to-stand action was performed under three different standing strategies, with each trial lasting on the order of 30 seconds.

An important issue is raised during the creation of these individualised models. The individualisation process directly models and assesses an individual's abilities without making any apriori assumptions based on age/race/sex. This is in contrast to current allometric techniques where these factors are used for cohort allocation. By allowing for non-prejudicial measurements of performance, the proposed framework allows for cohort allocation based on abilities. This also removes the current clinical problem of attempting to categorise individuals who do not fit into clear categories of race/sex.

From this data a representative kinematic skeleton was recovered with functional limb lengths that closely matched those recovered through direct measurement. The recovered skeletonisation was robust to marker error, variations in marker placement, and marker drop: automatically identifying the number of segments, the local coordinates of the markers and recovering a dynamically consistent joint state. This joint state was found to be consistent between trials, and did not suffer from the artefacts that were present in the commercial recovery process.

This kinematic model was then used to develop a individualised dynamic model. The dynamic model recovered through normal standing was found to a be an improvement over an allometrically scaled model at the estimation of the contact wrench and CoP under different standing strategies. The recovered dynamic model was then used to determine when the seat-off action occurred, signified by measured and expected wrench coinciding. This seat-off event matched the criterion proposed by Etnyre[35], giving a dynamic validation for this seat-off criterion.

Based on the recovered COP trajectories, an individualised model could be used to get an approximation of the COP during standing. However, given the variation in the measurements of a few centimetres, compared to the millimetre accuracy and precision from an affordable Wii Balance board[24][145], the proposed method is not recommended if the goal is exclusively COP estimation.

The recovery method does appear to provide consistent individualised models that produce better estimators of the contact forces than allometric models. The accuracy and repeatability of these joint torques needs to be further investigated to determine the cause of the discrepancies in the joint torques between the Winter and recovered models.

After performing this analysis on the sit-to-stand action, it was found that while it is possible to recover a dynamic model from the sit-to-stand action, this may not be sufficiently dynamically exciting for full individualisation of a model. This can be seen in the variation in the model parameters depending on standing strategy. While the *dynamic* standing strategy was more dynamically exciting (as seen by the lower condition number), the recovered dynamic model actually performed worse than the models obtained through *normal* and *stable* standing. The cause of this effect and the guidelines for sufficiently exciting actions therefore needs to be investigated.

Part II

Prescriptive Assistive Devices

Chapter 7

Prescriptive Robotics

Part I of this thesis outlined a method for creating a kinematic and dynamic model of an individual. This chapter will outline how these models can be used in the design and development of assistive devices.

Section 7.1 outlines a brief background on the use of assistive devices in rehabilitation, and the existing methods for customisation. This work extends the state of the art by posing the customisation as an optimisation problem (Section 7.3). This method is applied to determine the spring stiffness for a passive shoulder device in Section 7.4.

7.1 Motivation

Current robotic assistive devices are limited by affordability, accessibility and weight. There have been substantial advances in wearable robotics, resulting in a number of commercialised devices that offer the individuals the ability to move. Despite these advances, the majority of work has been performed on the lower limbs, in part due to the simplicity of the potential actions. Subjects are likely to want to stand, sit, or walk in a cyclic gait pattern. Given this finite set of actions, a user can select the desired state which can then be afforded by the device.

In contrast, the control and assistance of an upper limb device has a potentially infinite set of states. Individuals can pick, push and move freely within their range of motion. Estimating the intent of the user is an open research problem, one that has been attempted via eye tracking and brain-machine interfaces. The use of these devices is far from ideal, with high associated cost, and a potential requirement for brain surgery[**frisoli2012new**]. This restricts their use to individuals with profound disabilities.

The actuation strategies typically used are also sub optimal. Actively driven systems that use electric motors require an associated gear-train in order to provide the substantial torques required for daily function. The mass of the motor and gear-train lead to significant cost and weight for the device, especially if the assistance is non-targeted, with actuators placed at each joint regardless of patient functionality.

Instead of adopting this approach, a prescriptive based approach is adopted. Using the human model, it is possible to create a metric on the space an individual can reach. A method to obtain this metric is introduced in Section 7.2.

This metric can be used as the cost function in an optimisation process. By searching over the space of device parameters, it is possible to determing the actuator type and specification capable of best assisting that individual or patient cohort. An initial formulation of this problem is shown in Section 7.3, with an application to the specification of a passive shoulder orthosis in Section 7.4.

7.2 Metrics

Through the kinematic modelling methods shown in Section 3.2 it is possible to get an estimate of the kinematic structure of an individual, and estimates of the kinematic states for a given action. From these measurements, we develop a method for estimating the *workspace* of an individual. The workspace is a term used in robotics to describe the space an end-effector of a manipulator is able to operate in.

This problem looks at the mappings between two spaces. The *configuration* space is the space of all the feasible joint angles in the system. The *output* space is the space the serial chain moves in. This is likely to be either $SE(3)$ or $SE(2)$ for 3D and 2D applications.

Given constraints on the configuration space based on actuator limits, the aim is to find the corresponding limits in the output space. This subset of the output space is termed the *workspace* $\mathcal{W}$ of the manipulator[94]:

$$\mathcal{W} = \{\boldsymbol{g}_{W,T}(\boldsymbol{\theta}) : \boldsymbol{\theta} \in Q\} \subset SE(n) \tag{7.1}$$

7.2.1 Clinical Metrics and Challenges

As mentioned in Section 1.1 there are a lack of clinical metrics that are able to track functional changes of an individual's reach in a quantitative manner. One of the methods that has shown success is that of the *Reachable Workspace*[68]. This method tracks and projects the movements of the shoulder, onto a 3D spherical shell. By examining the sections of this shell that are within the user's reach, a quantitative measurement of the reachable surface area is returned. This metric has been shown to correlate with existing upper limb measures such as Brooke and Fugl-Meyer scales.

One of the limitations of this method is its projection onto a plane instead of a full 3D volume. This is due to the lack of a dense sampling of the workspace of the individual. Due to experimental limitations, it is impractical for individuals to sweep out every point they can reach. Therefore an alternative approach must be adopted.

7.2.2 Formulation

To overcome the challenge of obtaining a dense sampling of points, it is possible to exploit the results from Chapters 2 and 3. The kinematic model allows for the conversion of observed motions of the limb into joint trajectories. By determining the kinematic limits of these trajectories, the workspace that corresponds to the projections of these limits can be estimated.

Consider the two link planar system shown in Figure 7.1. The motions of two points on this system are known: the elbow in green and the wrist in red. During a simple trajectory the green and red motion capture points are observed. Using the kinematic recovery method from Chapter 3, it is possible to recover both the joint centres and the joint state $\boldsymbol{\theta}(t)$ for the observed trajectory.

The upper and lower bounds for this joint trajectory can be found, and are denoted $\bar{\boldsymbol{\theta}}$ and $\underline{\boldsymbol{\theta}}$.

Three assumptions will be made:

A1 The upper and lower bounds are representative of the kinematic limits of the individual.

A2 Joints act independently of each other.

A3 The kinematic limits of the individual are sufficient to describe an individual's weaknesses.

Under these three assumptions, it is possible to generate a dense sampling of the workspace.

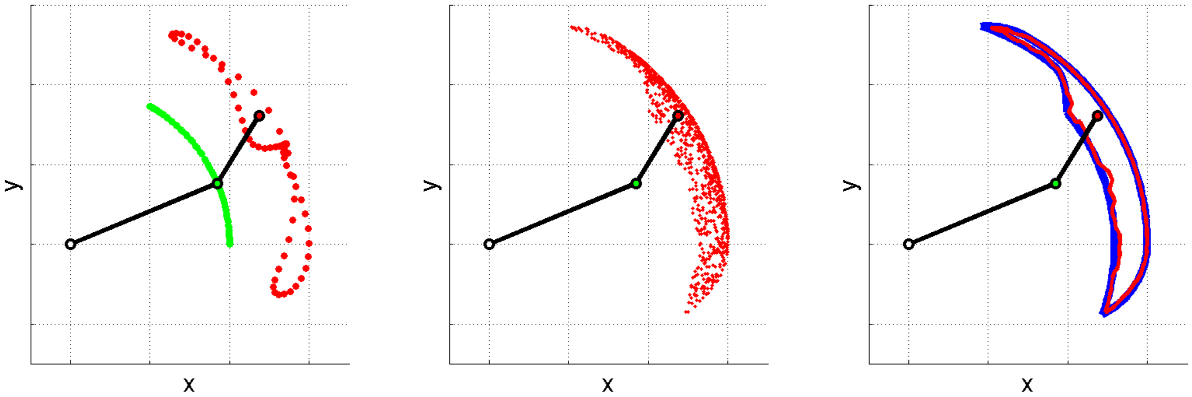

Figure 7.1: An overview of the reachable workspace volume method. Left: Motion capture of the two link system returns two trajectories of the system elbow and wrist (green and red). Middle: The upper and lower bounds of these trajectories are then used to create a random sampling of the joint space. These joint space points are then projected into the output-space using the kinematic map (red). Right: The best fit non-convex hull is then generated for these points. This gives an estimate of the workspace (red). The true workspace is shown in blue.

The joint limits $[\underline{\boldsymbol{\theta}}, \bar{\boldsymbol{\theta}}]$ define the configuration space of the manipulator. A matrix of S samples of feasible configurations of the manipulator can be generated. Given a configuration $\boldsymbol{\theta}(s)$, it is possible to find the corresponding point in the output space using the forward kinematic map. This gives a set of tool configurations $\boldsymbol{g}_{W,T}(s)$ for each sample. A collection of these tool positions are shown in Figure 7.1 Middle.

This sampling allows for a denser sampling of the workspace based on the single trajectory used for kinematic recovery. These points can be used to generate a non-convex hull corresponding to the system's workspace using alpha-shapes[32]. This gives an estimate of the workspace of the system.

7.2.3 Method

This method was tested on a number of healthy subjects, and patients with Facioscapulohumeral muscular dystrophy (FSHD). Subjects were recruited under IRB and informed consent. FSHD patients were diagnosed based on genetic analysis[49].

Subjects were asked to follow a video showing a set of upper limb tasks. This included touching the sides of their hips, shoulders, mouth and the top of their head. Their movements were captured using a Kinect skeleton. These actions were chosen as they covered key locations that are required for self care tasks. Each patient was also given a Brooke score by a clinical evaluator.

The Kinect data was converted into a rigidised skeleton using a Kinematic modelling method similar to that shown in Chapter 3. The angles at the shoulder were decomposed to match the joint convention recommended by the ISB[140]. This resulted in the upper limb model shown in Figure 7.2. The recovered kinematic model was then used to generate 10,000 sample points of the workspace. The alpha-shapes for these samples were then computed using the AlphaShapes library in MATLAB[76], returning the geometry and volume of the reachable workspace volume.

7.2.4 Results

The results of these tests are shown in Table 7.1 and the visualisations of the reachable workspace volume are shown in Figures 7.3 and 7.4.

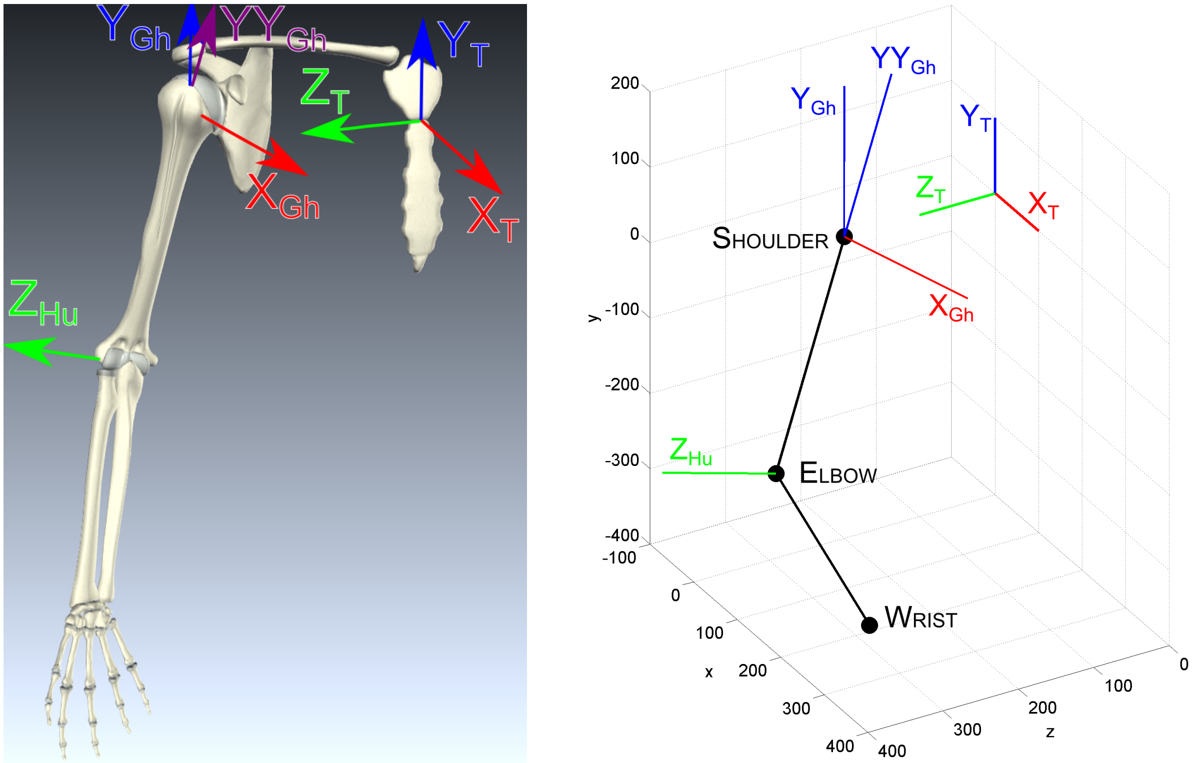
YGh
YYGh
YT
ZT
XGh
XT
ZHu
200
100
0
y -100
-200
-300
-400
-100
0
100
x 200
300
400
400
300
200
z
100
0
YYGh
YGh
YT
ZT
XT
SHOULDER
XGh
ZHu
ELBOW
WRIST

Figure 7.2: Left: International Society of Biomechanics (ISB) recommendations on definitions of joint coordinates and rotational axes[140]. Skeletal model generated using Biodigital Human[56]. Right: Kinematic model used for the upper limbs. Y_{Gh} is parallel to Y_T, while YY_{Gh} runs parallel to the humerus. Location of the rotational centre of the X_{Gh} joint is given in Thorax (T) coordinates. Rotational pose of the humerus is based on a Y-X-Y rotational sequence about Y_{GH}-X_{GH}-YY_{GH}. Rotation about the Hu joint is about the Hu_Z axis.

Table 7.1: Comparison of computed reachable volume and Brooke Score

Subject	Reachable Volume (m^3)	Brooke Score (unitless)
Healthy 1	3.74×10^{-1}	-
Healthy 2	3.28×10^{-1}	-
Healthy 3	2.34×10^{-1}	-
Patient 1	3.58×10^{-1}	1
Patient 2	2.70×10^{-1}	2
Patient 3	1.78×10^{-1}	3
Patient 4	1.48×10^{-3}	5

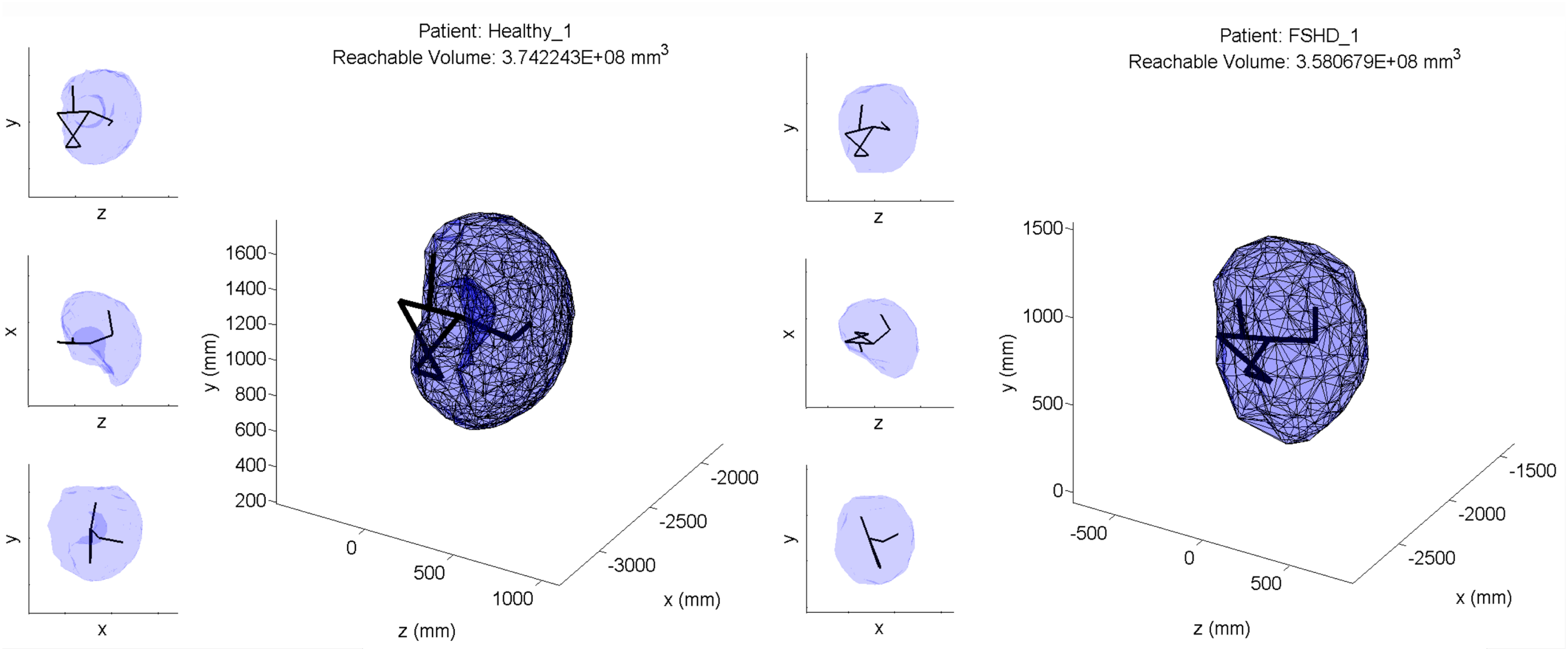

Figure 7.3: Left: Reachable workspace for a healthy subject. Upper extremities are shown in wire-frame with the reachable workspace shown in blue. Plane projected views are shown on the left. Right: Reachable workspace for Patient 1 with mild FSHD (Brooke 1).

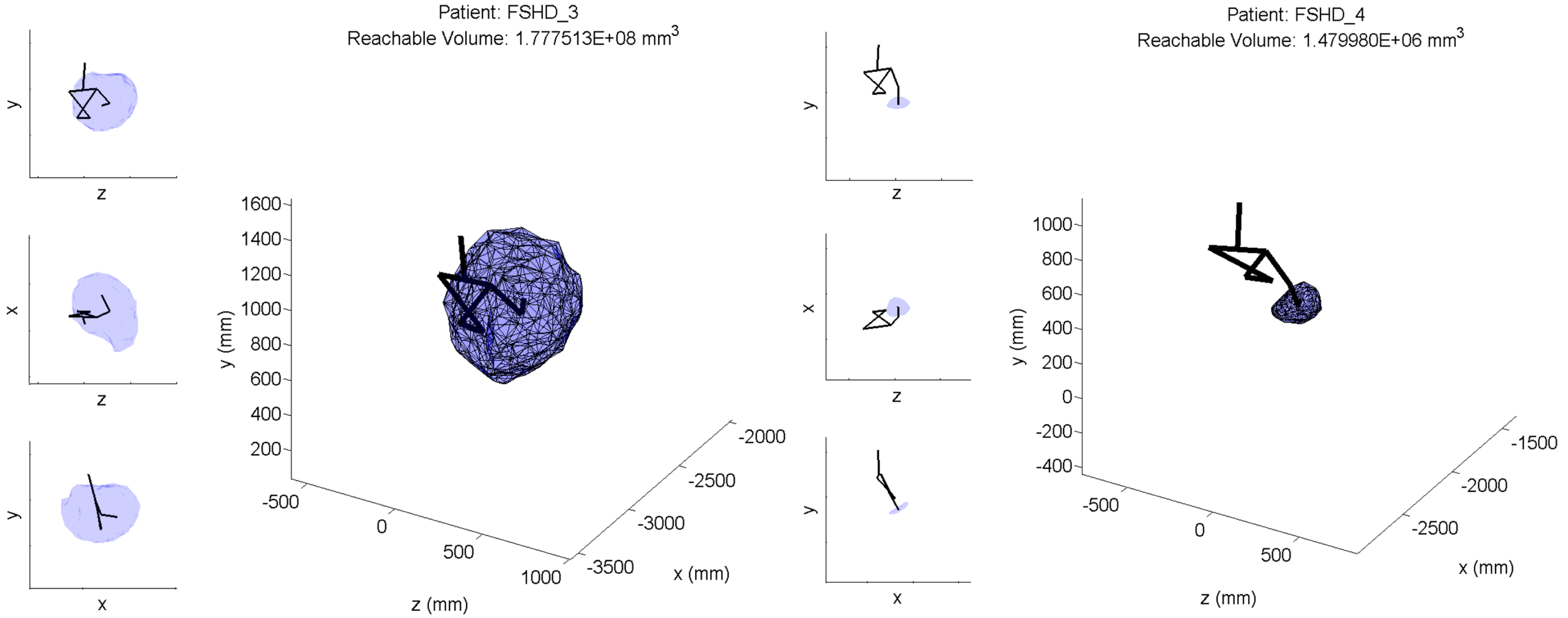

Figure 7.4: Left: Reachable workspace for Patient 3 with moderate FSHD (Brooke 3). Right: Reachable workspace for patient 4 with severe FSHD (Brooke 5).

7.2.5 Discussion

Table 7.1 shows a correlation between the Brooke score and the reachable volume. Patients with lower levels of disability were found to have similar reachable workspace volumes to healthy individuals.

The workspaces shown in Figures 7.3 and 7.4 show a number of interesting features. The shape and size of the workspace changes dramatically with the Brook score value. Changes were most clearly seen in the vertical direction, with patients with sevee disability losing the ability to reach above their shoulders. This could act as a predictor or measure of a patient's level of independence. While the population size used for these initial experiments is small, these initial results show the potential in extending the kinematic models to the development of human performance metrics.

7.3 Prescriptive Robotics

An important result from this reachable volume work is the use of the reachable workspace volume as an optimisation cost function. Using the workspace volume in this manner allows for an optimisation over the kinematic and dynamic model parameters. By creating a model of the human assisted system, the aim is to determine the optimal assistive parameters to assist the individual.

7.3.1 Formulation

To build this formulation, a model of the human assisted system is made. Using the form for the dynamics from Equation 4.1, the human dynamic model can be written as:

$$\boldsymbol{I}_H(\boldsymbol{\theta})\ddot{\boldsymbol{\theta}} + \boldsymbol{C}_H(\boldsymbol{\theta}, \dot{\boldsymbol{\theta}}) = \boldsymbol{\tau}_H \tag{7.2}$$

where $\boldsymbol{I}_H$ and $\boldsymbol{C}_H$ are the human inertial and bias matrix, and $\boldsymbol{\tau}_H$ is the human torque.

The human assistive system can therefore be written as:

$$\boldsymbol{I}_{H+A}(\boldsymbol{\theta})\ddot{\boldsymbol{\theta}} + \boldsymbol{C}_{H+A}(\boldsymbol{\theta}, \dot{\boldsymbol{\theta}}) = \boldsymbol{\tau}_H + \boldsymbol{\tau}_A \tag{7.3}$$

where $\boldsymbol{I}_{H+A}$ and $\boldsymbol{C}_{H+A}$ are the inertial and bias matrices for the human-assistive system, and $\boldsymbol{\tau}_A$ is the assistive torque.

A passive device can be written in the form:

$$\boldsymbol{\tau}_P = f_P(\boldsymbol{\psi}, \boldsymbol{\theta}, \dot{\boldsymbol{\theta}}) \tag{7.4}$$

where $\boldsymbol{\psi}$ are the parameters of the device (stiffnesses, damping factor etc.).

This results in the system dynamics:

$$\boldsymbol{I}_{H+A}(\boldsymbol{\theta})\ddot{\boldsymbol{\theta}} + \boldsymbol{C}_{H+A}(\boldsymbol{\theta}, \dot{\boldsymbol{\theta}}) = \boldsymbol{\tau}_H + f_P(\boldsymbol{\psi}, \boldsymbol{\theta}, \dot{\boldsymbol{\theta}}) + \boldsymbol{\tau}_A \tag{7.5}$$

The optimisation problem is therefore to maximise the *functional* workspace for the human-assistive system. The functional workspace is defined by the points that are achievable through a combination of human and active assistance, that obey the system dynamics and joint angles lie within their permissible limits. This leads to a definition of the *functional* workspace (FW) of the system:

$$\begin{array}{rc} & FW = \{\boldsymbol{p} | \boldsymbol{p} \in f_{FK}(\boldsymbol{\theta}(t))\} \\ s.t. & \boldsymbol{I}_{H+A}(\boldsymbol{\theta})\ddot{\boldsymbol{\theta}} + \boldsymbol{C}_{H+A}(\boldsymbol{\theta}, \dot{\boldsymbol{\theta}}) = \boldsymbol{\tau}_H + f_P(\boldsymbol{\psi}, \boldsymbol{\theta}, \dot{\boldsymbol{\theta}}) + \boldsymbol{\tau}_A \\ where & \theta \in [\underline{\boldsymbol{\theta}}, \bar{\boldsymbol{\theta}}], \tau_H \in [\underline{\boldsymbol{\tau}}_H, \bar{\boldsymbol{\tau}}_H], \tau_A \in [\underline{\boldsymbol{\tau}}_A, \bar{\boldsymbol{\tau}}_A] \end{array} \tag{7.6}$$

7.4 Passive Shoulder Orthosis

This definition of a functional workspace definition can be used to formulate an optimisation problem to determine the optimal assistance for an individual with shoulder weakness. The arm is modelled as a pendulum, with the weakness simulated as decreased maximum and minimum shoulder torque (Figure 7.5). This weakness will be compensated through the use of a single spring at the shoulder, an idea inspired by the WREX exoskeleton[107]. The WREX is a passive elastic exoskeleton that assists an individual using a passive spring. By manually tuning the sping characteristics, gravity compensation of the limb can be achieved.

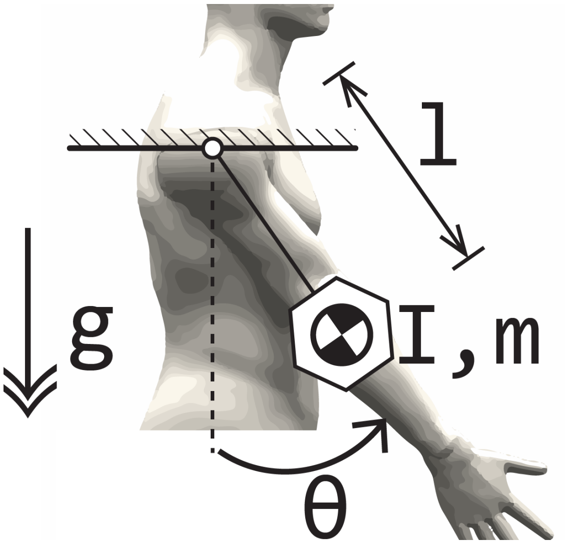

Figure 7.5: An illustration of the simplified arm model used in simulation. The arm is modelled as an inertial load I at a distance l from the origin.

The dynamics of this system can be written as:

$$(I + ml^2)\ddot{\theta} = -mgsin(\theta) - k_1(\theta - \theta_0) + \tau_H \tag{7.7}$$

where k and θ_0 are the stiffness and equilibrium point of the spring. Note that the additive torque is only that of the human τ_H as the assistive torque is purely that of the torsional spring.

7.4.1 Direct Optimization

The functional workspace of this system can be estimated by examining the points that the individual can remain in statically. This reduces the system into the equation:

$$mglsin(\theta) + k_1(\theta - \theta_0) = \tau_H \tag{7.8}$$

The dynamics in Equation 7.7 can then be simplified into the study of three key angles, the maximum and minimum of the spring extension (θ_u,θ_l) and the maximum torque static torque of the system (θ_m). This maximum static torque can be found by differentiating Equation 7.8.

$$\theta_m = acos\left(-\frac{mgl}{k_1}\right) \tag{7.9}$$

These three points define the torque curve for the spring. The optimisation problem then simplifies to:

$$\begin{array}{rc} & \max_{\theta_l,\theta_u,k_1,\theta_0}(\theta_u - \theta_l - \delta k_1) \\ st. & \underline{\tau}_H \leq mglsin(\theta_u) + k_1(\theta_u - \theta_0) \leq \bar{\tau}_H \\ & \underline{\tau}_H \leq mglsin(\theta_m) + k_1(\theta_m - \theta_0) \leq \bar{\tau}_H \\ & \underline{\tau}_H \leq mglsin(\theta_l) + k_1(\theta_l - \theta_0) \leq \bar{\tau}_H \\ & -2\pi \leq \theta_0 \leq 2\pi \\ & 0 \leq k \\ & \underline{\theta}_H \leq \theta_l, \theta_m, \theta_u \leq \bar{\theta}_H \end{array} \tag{7.10}$$

where the constraints ensure that the torques corresponding to the key points are within the feasible human torque and position range. The weighting term δ is used to minimise the stiffness of the spring (a value of 1×10^{-4} was used in these studies).

The optimisation problem shown in Equation 7.10 can be easily adapted to include certain points are in the workspace. If an angle θ_R is required to lie within the workspace, then the following constraints can be added:

$$\underline{\tau}_H \leq mglsin(\theta_R) + k_1(\theta_R - \theta_0) \leq \bar{\tau}_H \tag{7.11}$$

Pathologies were simulated as percentages of the minimum torque required to statically hold the arm parallel to the ground. The optimisation shown in Equation 7.10 was implemented using YALMIP library[74] and MATLAB for a number of simulated disabilities.

7.4.1.1 Results

The results of these simulations on a healthy individual is shown in Figure 7.6. Individuals with a simulated shoulder weaknesses are shown in Figures 7.7 and 7.8.

7.4.1.2 Discussion

From these initial experiments it appears that a single spring at the shoulder is capable of dramatically increasing an individual's ability to move. In the healthy example, the addition of a spring is determined to be pointless, and a spring stiffness of $0Nn/deg$ is returned. This shows that the recovery method is capable of actuator selection. Given an appropriate cost function, the actuators can be added to the system or removed based on negligible returns.

For subjects with symmetric weakness (Figure 7.7), the addition of a spring is capable of dramatically increasing the size of the workspace, and its location. The workspace now includes regions that are more useful for daily function, potentially improving independence. The torque response curves show the effect of the addition of the spring. Ordinarily a patient

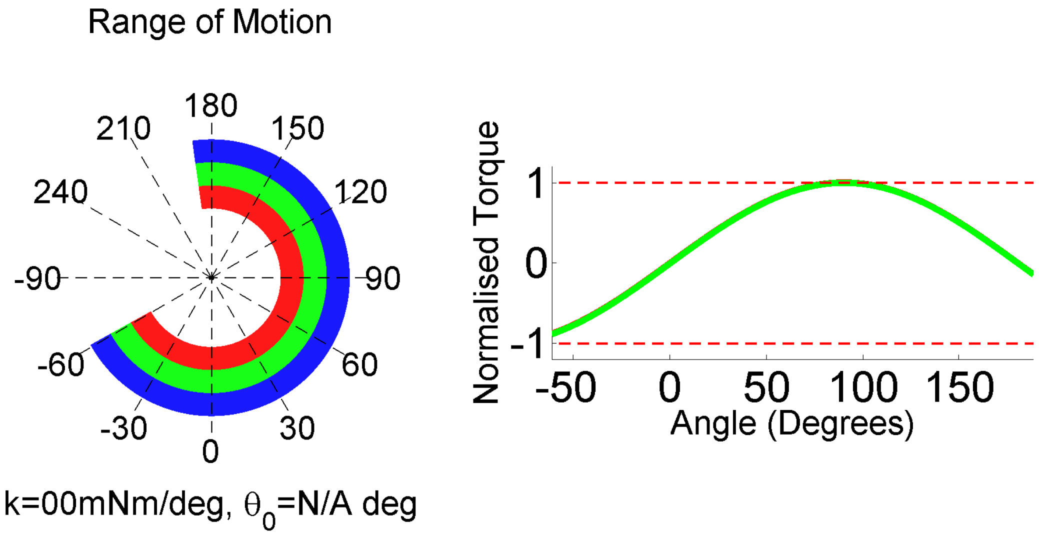

Figure 7.6: Optimisation for a healthy individual. Left: Saggital plane plot of range of motion. Blue: healthy, Red: subject pre-intervention, Green: subject post intervention. Spring stiffness and offset is shown underneath. Right: Torque response plot. Red dashed lines are the limits of the individual's ability. Curves indicate the torque response for each case.

with weakness is unable to overcome the highest torque point in their range of motion. This limits their abilities as they are unable to move past this point. By adding a spring, the arm is rebalanced so that this point lies within their abilities, allowing them to move past this limiting point, increasing their total range of motion.

The proposed optimisation method also shows potential benefits to individuals with asymmetric weakness as shown in Figure 7.8. From these figures, the change between flexion and extension strength simply shifts the set equilibrium point of the spring.

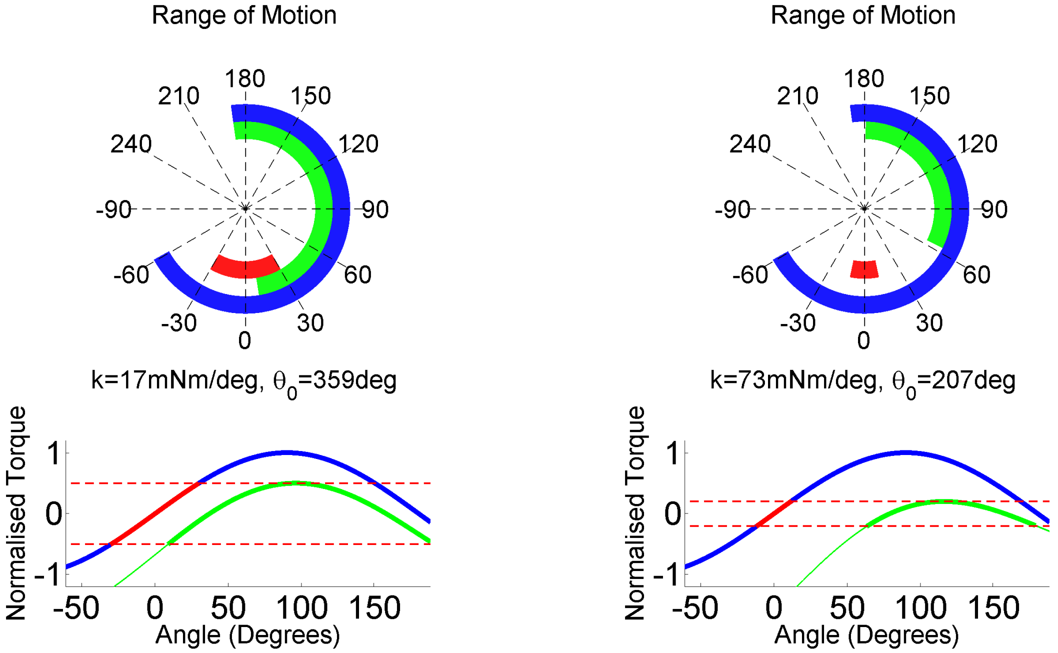

Figure 7.7: Left: An individual with symmetric 50% strength. Right: An individual with symmetric 20% strength.

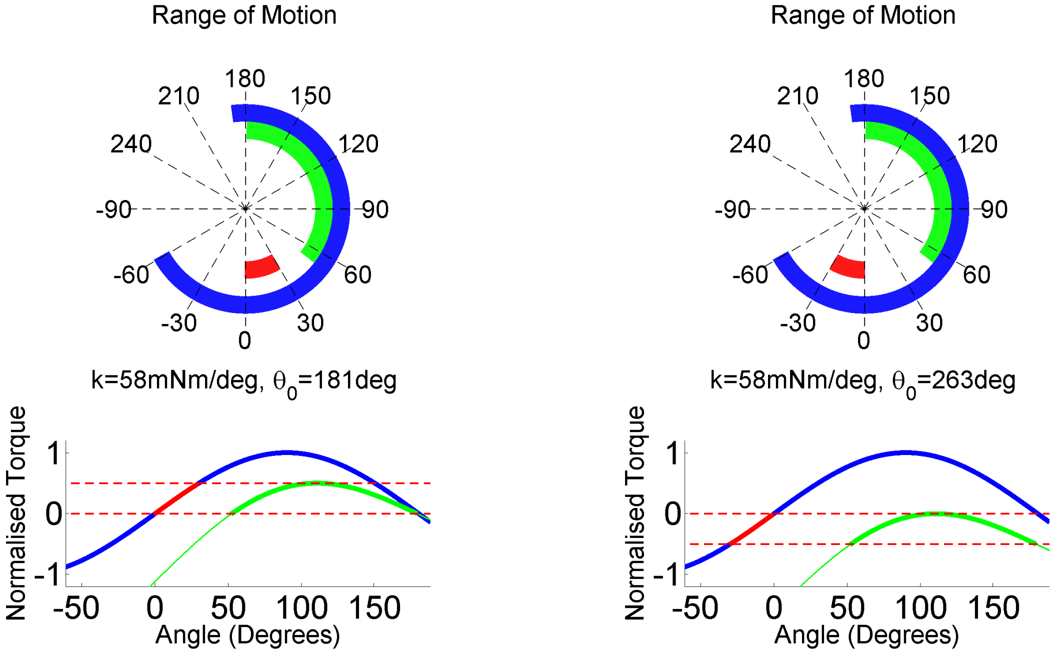

Figure 7.8: Left: An individual with 50% strength in flexion. Right: An individual with 50% strength in extension.

7.4.2 Level-Set Methods

An alternative approach to this problem is through the use of *level-set methods*[91]. These methods allow for simulation of the dynamics of a system to determine the set of potential states that are *reachable* over a time horizon. As the system dynamics evolve over time, this reachable boundary extends. Given a level set function $\chi(x)$, the corresponding reachable set has the form:

$$\{x \in \mathbb{R}^d | \chi(x) = 0\} \tag{7.12}$$

This problem can be solved by finding the solutions to an initial value partial differential equation:

$$D_t\chi(x,t) + \min[0, H(x, D_x\chi(x,t))] = 0 \tag{7.13}$$

where D_t and D_x are the partial derivatives of χ and the associated Hamiltonian H is written as:

$$H(x,p) = \max_{a \in \mathcal{A}, b \in \mathcal{B}} p^T f(x,a,b) \tag{7.14}$$

where f are the dynamics of the system and $p_i = \nabla\chi(x,t)$. This can be solved by numerically approximating the Hamiltonian using the *level-set toolbox*[90]:

$$\hat{H}(c, p^+, p^-) = H\left(x, \frac{p^+ + p^-}{2}\right) - \alpha^T(x)\left(x, \frac{p^+ + p^-}{2}\right) \tag{7.15}$$

where p^- and p^+ are the left and right numeric approximations of the gradient. The scaling $\alpha(x)$ term is dependent of the partial derivative of the Hamiltonian with respect to the gradient p:

$$\alpha_i(x) = \max_p \left| \frac{\partial}{\partial p_i} H(x,p) \right| \tag{7.16}$$

The dynamics of the system can be written with the state $\boldsymbol{X} = [\theta, \dot{\theta}]^T$:

$$\begin{bmatrix} 1 & 0 \\ 0 & I_T \end{bmatrix} \dot{\boldsymbol{X}} = \begin{bmatrix} \dot{\theta} \\ -mlgsin(\theta) - k_1(\theta + \theta_e - \theta_0) \end{bmatrix} + \begin{bmatrix} 0 \\ 1 \end{bmatrix} \tau \tag{7.17}$$

To write the Hamiltonian, an optimal controller is required that takes into account the limits of the individual's strength. Assuming a symmetric torque bound, the optimal controller to maximise the reachable space is:

$$\begin{aligned} \tau_H^* &= \begin{cases} \underline{\tau} & if p_2 \leq 0 \\ \bar{\tau} & otherwise \end{cases} \\ &= |\bar{\tau}_H| sgn(p_2) \end{aligned} \tag{7.18}$$

This optimal controller can be used to generate the Hamiltonian:

$$H(x,p) = x_2 p_1 + |\bar{\tau}_H| sgn(p_2) - I_T^{-1}\left(mlgsin(x_1 + \theta_e) + k_1(x_1 + \theta_e - \theta_0)\right) + |\bar{\tau}_H| \tag{7.19}$$

and bounds on the scaling terms:

$$\begin{gathered}\alpha_1 \leq |x_2| \\ \alpha_2 \leq |I_T^{-1} mlgsin(x_1 + \theta_e) + I_T^{-1} k_1(x_1 + \theta_e - \theta_0)| + |\bar{\tau}_H|\end{gathered} \tag{7.20}$$

The reachable set for this system was generated using the level-set toolbox for an individual with a symmetric weakness of 20%. A grid of $k \in [0.005 : 0.005 : 0.1]$ and $\theta_0 \in [180 : 10 : 360]$ and a time horizon of two seconds was used.

7.4.2.1 Results

The search space of spring parameters is shown in Figure 7.9 along with the level set for an optimal combination of parameters.

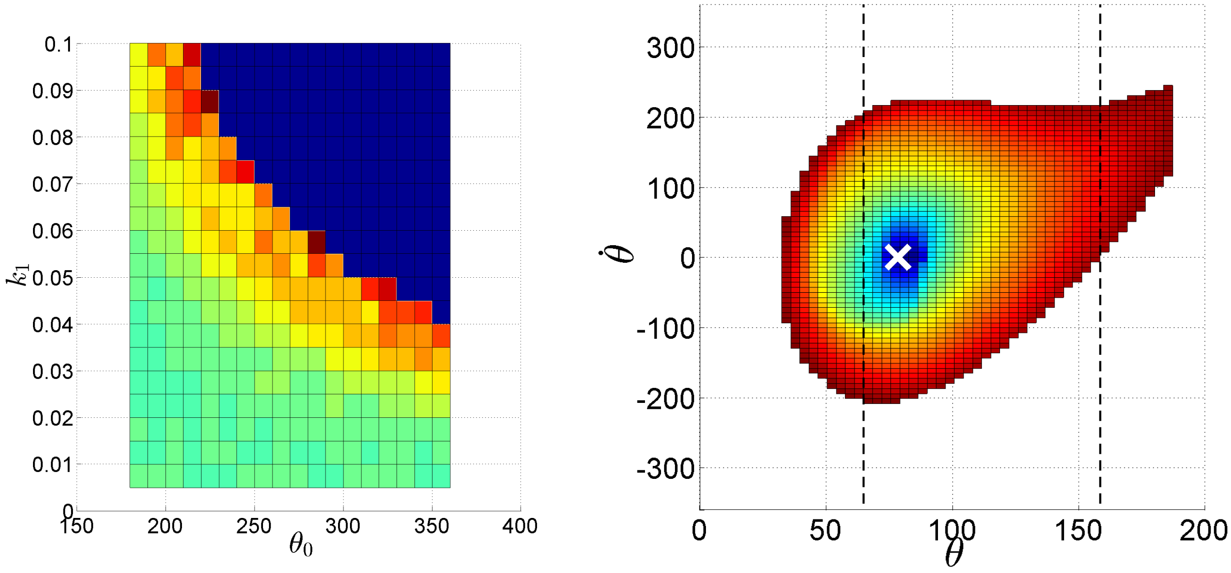

Figure 7.9: Left: Heatmap showing the change in workspace with spring parameters using the level-set method. The top right blue region shows infeasible points where the system equilibrium is outside of the individual's range of motion. Blue to red transition shows progressively larger workspaces. Right: Reachable set for a single simulation ($k_1 = 75mNm/deg$ and $\theta_0 = 210deg$). The static equilibrium point is located at the cross in the centre of the Figure. Blue to red colours show the increasing time taken to move from the equilibrium point to other points in the reachable set. The positions that the individual is able to reach and hold were computed and are indicated as vertical black lines.

7.4.2.2 Discussion

The utility of the level-set method can be seen in the difference between the full level set and the angles that were found to be statically achievable. The level-set contains the set of points that are achievable, even if the individual cannot remain there statically. This makes the level-set useful for determining transitions for hybrid controllers and safety analysis[124].

The *front* of potential candidate solutions (shown by the sudden curve from orange to blue) makes the design choice problematic, as there is no clear optimal spring to use. This could be improved by creating a finer resolution mesh in this region, or parametrising the front and performing an optimisation over this space.

7.4.3 Conclusion

Table 7.2 compares the direct and reachable set methods for determining actuator parameters. Both methods were implemented on a dual core computer with a 1.6GHz processor and 16Gb RAM.

Table 7.2: Comparison between the direct optimisation and the level-set method for different time horizons. Recovered upper and lower bounds for workspace are shown, along with the associated computation time.

	Direct	Level-set Timespan			
		1	2	3	4
Lowerbound θ_l (deg)	63	64.8	64.8	64.8	64.8
Upperbound θ_u (deg)	179	84.4	122.4	172.8	176.4
Computation Time (s)	0.75	18	37	55	81

The recovered range of motions and optimal values appear to align between the two methods, on the condition that the time horizon is adequately set. The location of the equilibrium point and the lower bound align for relatively low time horizons. However the upper bound requires a larger time horizon due to the upper bound only being reachable after more elapsed time.

The reachable set method is an under approximation of the workspace of the system. This can be seen in under estimation of the workspace bounds. The spring parameter estimation is also limited by the meshing of the search parameters. This can lead to significant burdens if the number of system parameters is larger than two.

The time for computation shows a significant difference between the two methods. It is important to note that the computation time for the level-set method is per dynamic parameter iteration. To obtain the optimal dynamic parameters the entire search process took 0.75 seconds using the direct approach, compared to 12 hours for the level-set method. Even for a simple system, the level-set method is computationally intensive. This leads to the *curse of dimensionality* where systems of 4 or more states are rendered intractable by these searches[2][92]. This is highly limiting in the application to human assistive systems as this limits the system to two degrees of freedom.

The direct optimisation method is a rapid method to perform this analysis. The extension of the reachable workspace volume methods to this optimisation scheme is a promising direction for prescriptive assistive devices.

Chapter 8

Active Passive Exoskeleton

Building on the concepts introduced in Chapter 7, this chapter introduces the *Active Passive EXoskeleton* (APEX). The APEX is an upper limb assistive device designed to assist individuals with elbow and shoulder weakness. This work was completed with the substantial effort of Eric J. Mica, Joel A. Loeza, Waiman Meinhold, and Elizabeth Barley.

8.1 APEX

The APEX is designed to utilise the results covered in this thesis. Instead of developing a single device for use in industry and healthcare, tasks and individuals can be scanned using the human modelling methodology (Chapters 3-6) to generate a prescription for the optimal assistive device (Chapter 7).

As patient abilities can be measured and tracked over time, it allows for the development of new types of human-centric control, and the use of exotic actuation methods. The APEX uses a novel pneumatic actuation framework to provide assistance to the user, which is lighter, more affordable, and uses less energy than conventional DC motor setups.

8.1.1 APEX Framework

The WREX exoskeleton shows that it is possible to enhance an individual's function by using a passive elastic system that compensates for the mass of a limb[107]. Using this idea as inspiration, APEX examines the use of *Variable Dynamic Actuators* (VDAs) to see how the changes to the perceived dynamic parameters can affect the abilities of the individual. An interpretation of this idea is attempting to perform hardware based impedance control, modifying the system's overall dynamic parameters to achieve the desired response.

One implementation of a variable dynamic actuator is a pneumatic cylinder (Figure 8.1). By varying the pressures on either side of a cylinder (P_{flex}, P_{extend}), it is possible to change both the stiffness and equilibrium point of the cylinder rod.

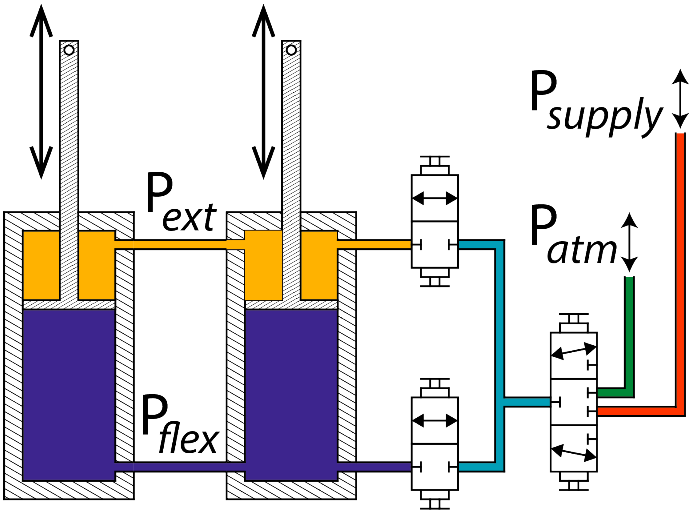

Figure 8.1: Schematic of the pneumatic spring used in the APEX. Three valves allow for the pressurisation and venting of the extension and flexion (P_{flex}, P_{extend}) sides of the pneumatic cylinders. The system is driven by a pressurised supply line, and vents directly to the atmosphere.

The proposed control is based on the workspaces that can be found from the prescriptive robotics approach. Instead of attempting to determine the desired Cartesian location of the individual's arm through eye-tracking/brain-machine-interfaces, APEX changes the workspace of the individual. By using the prescriptive methods introduces in Chapter 7, the workspace can be set to contain the points required to complete a set of actions (such as self feeding/self care tasks). In this manner, a finite set of discrete workspaces can be generated, each with a specific VDA parameter set. The control is therefore heavily simplified, only detecting a desire to change workspace, then changing the VDA parameters accordingly.

When providing these changes to the system dynamics, the individual is still required to actively move their limb to perform their desired activity allowing for an *assistance as needed* approach[34] to rehabilitation. By quantifying their abilities, this can be tuned to the individual and adapted over time to ensure that the patient is able to act independently, without overcompensating for their weaknesses.

This approach to assistance also uses significantly less energy than through an active drive. The pressures in the cylinders only need to be changed when a new workspace is required. This results in zero expended gas while an individual performs a subset of tasks, a stark contrast to electric motors which use energy even if the arm is held statically against gravity. As such, only a small reservoir of compressed gas is required to assist in daily function.

8.2 Design

A prototype device was developed to test the effect of the APEX framework on the elbow flexion/extension. The elbow was chosen due to the importance of elbow motion in daily living tasks, the simplicity of the joint, and the ample space in the upper and forearm for attachment braces. Figure 8.2 shows a CAD rendering of the baseplate containing the pneumatic cylinders and the elbow brace, with the completed prototype shown in Figure 8.3. By separating the device into two sections, the load on the elbow was substantially minimised, reducing the load on shoulder. The elbow brace was found to weigh 0.39kg, with a total system mass of 2.54kg (not including pneumatic supply).

8.3 Initial Trials

The prototype shown in Section 8.2 was tested on a cohort of six healthy individuals aged 23 ± 1.7 years old, mass 73.8 ± 4.4kg, and 1.77 ± 0.28m under UCB IRB: 2012-12-4872. Subjects were outfitted with active motion capture markers which were tracked at 480Hz[104]. Subjects performed three trials of hammer curls with their right arm at 0.5Hz while holding a dumbbell weighing 3.59kg and using a preacher curl bench (Figure 8.4). The pace was set by an audible metronome. The end of the trial was specified by either the subject stopping, a break in tempo, or when the subject's actions moved out of the sagittal plane. Each trial was separated by a 5 minute break allowing the subject to rest.

The motion capture data was used to recover the joint angles and their derivatives of the shoulder and elbow, using the joint notation recommended by the ISB[140]. The number of curls were counted by an investigator, and cross-checked against the motion capture, and recovered kinematic state trajectories.

These experiments were performed under six different conditions, separated by a two day rest period. The six conditions tested were:

C Control: The subject is wearing a motion capture suit but no exoskeleton.

AC APEX Control: The subject is wearing both the motion capture suit and the exoskeleton. The flexion and extension sides are open to the atmosphere.

2 As **AC**, but with the extension and flexion chambers initially pressurised to 50 psi and atmospheric pressure, then sealed.

3 As **AC**, but with both the extension and flexion chambers initially pressurised to atmospheric pressure, then sealed.

4 As **AC**, but with both the extension and flexion chambers initially pressurised to 50 psi, then sealed.

5 As **AC**, but with the extension and flexion chambers initially pressurised to atmospheric and 50 psi, then sealed.

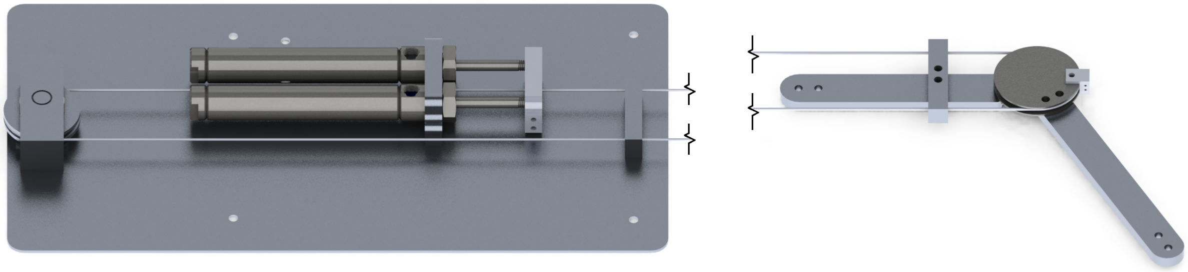

Figure 8.2: The two components of the APEX-β prototype. Left: Backplate showing two pneumatic cylinders and Bowden cable. The Bowden cables connect rigidly to the rod end of the cylinders. The cable wraps around a pulley on the left side of the plate and passes through a cable guide on the right. Right: The two ends of the Bowden pass through a cable guide and wrap around a pulley. Both sides of the pulley are attached to upper-arm and forearm cuffs[11].

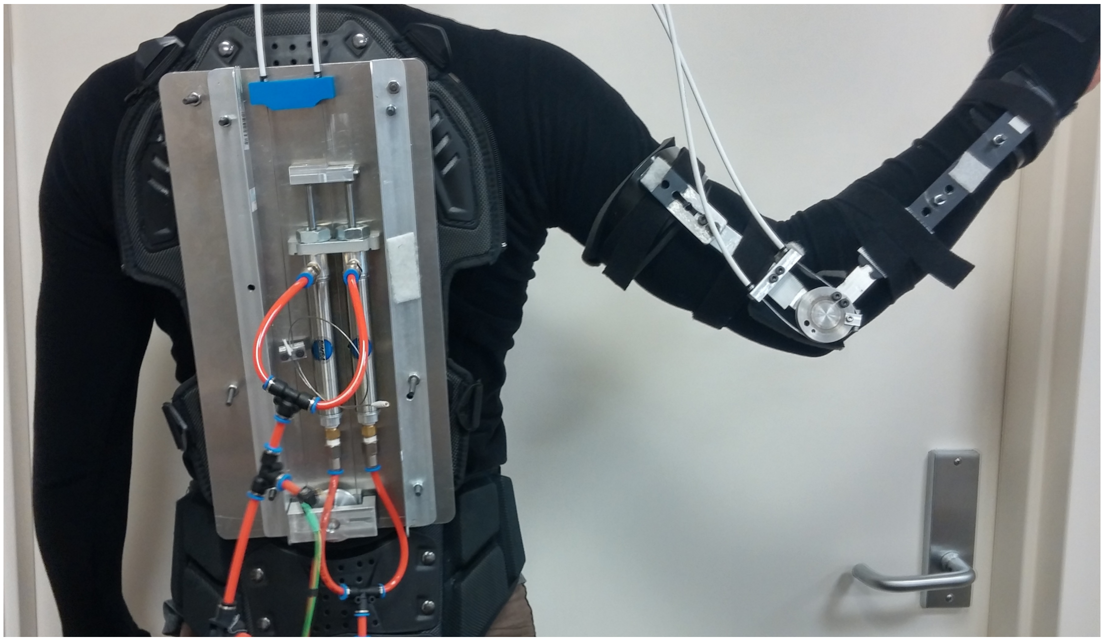

Figure 8.3: APEX prototype β shown mounted on an individual. Backplate and elbow mounts are shown. The two pneumatic cylinders on the backplate are visible with associated pneumatic lines. The blue cable guide at the top of the back plate routes the linear action of the cylinder along the white Bowden cables to the elbow.

The APEX device was configured for each test condition with the forearm in the fully flexed position. After the device was configured it was completely disconnected from the pneumatic supply to test the passive dynamic response. The results of these trials are shown in Section 8.3.1.

8.3.1 Results

Figure 8.5 shows the raw and normalised rep count for the six different modes. The normalised values were calculated for each subject and trial combination, using the respective results from their AC mode experiment.

Figures 8.6 to 8.9 show the reconstructed joint trajectories during the experiments for a representative subject. These joint states were recovered using an adapted kinematic recovery formulation, similar to that shown in Chapter 3.

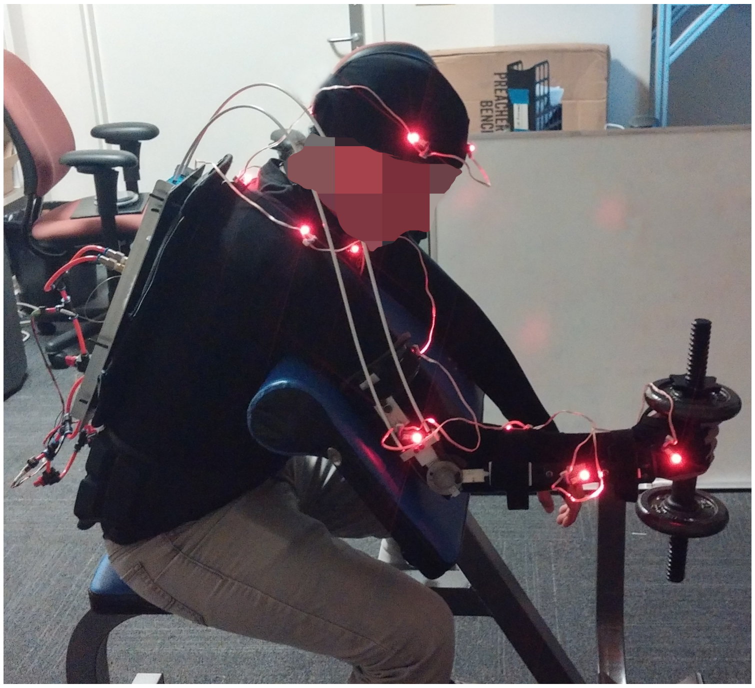

Figure 8.4: Experimental setup for the hammer curl experiments. Subject wearing motion capture suit with active motion capture markers (red lights). The backplate is mounted on the subject with Bowden cables connecting to the elbow mount. The 3.59 kg barbell is shown.

8.3.2 Discussion

Figure 8.5 summarises the effect of the APEX prototype. The normalised count was used to compare the effect each mode had between subjects.

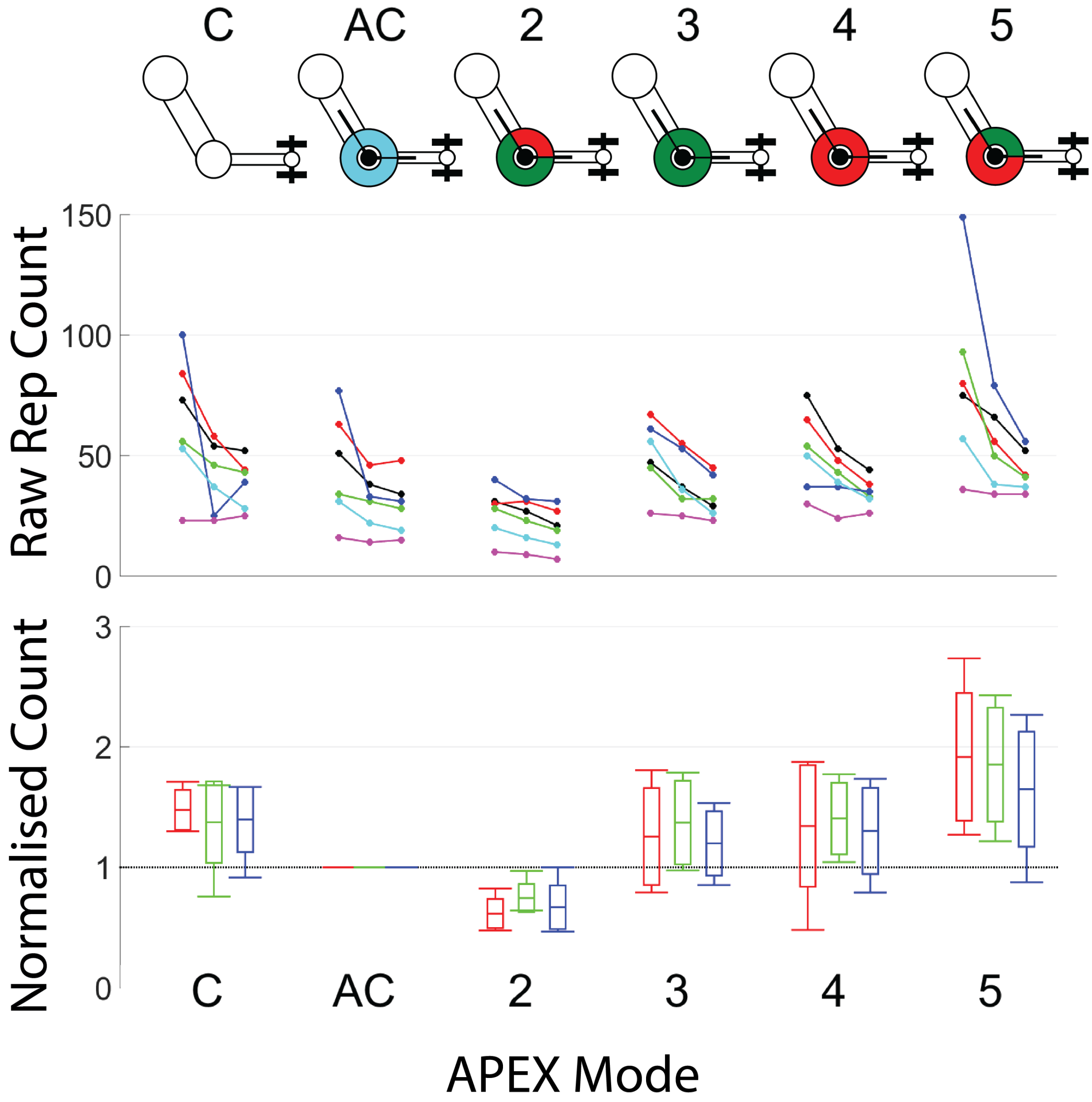

Figure 8.5: Summary of APEX results. Top: Raw rep count for the six subjects, for the three trials, across all six APEX modes. Each individual is represented by a a different colour line. First trial in a series is shown on the left, with the third on the right. Middle: Normalised reps. Each individual was normalised by their AC trial for the first, second, and third reps separately. The means and standard deviations are shown on box and whisker plot, with the extrema shown as the whiskers. Bottom: Cartoon of the APEX modes. Forearm shown in the sagittal plane holding a weight. Exoskeleton is shown as a disk on the elbow. The extension side of the cylinder is shown on top, with the flexion side underneath. A sealed chamber at 50 psi is shown in red, while a chamber sealed at atmospheric pressure initially is shown in green. A chamber that is open to the atmosphere is shown in light blue.

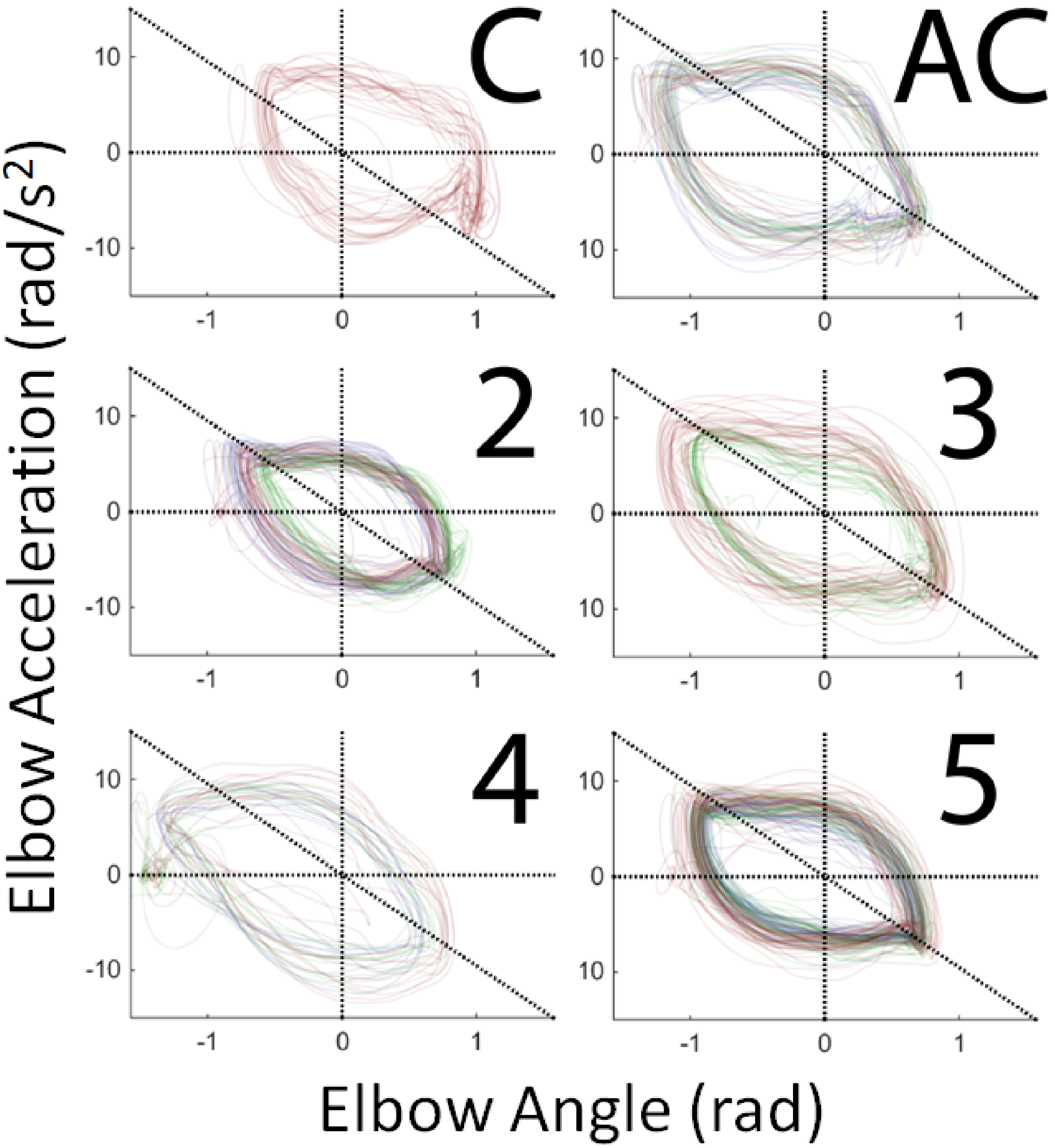

Figure 8.6: Phase portraits of angular acceleration (rad/s^2) against elbow angle (rad) for Elbow flexion/extension in a representative subject. All three trials are shown, with red, green, and blue representing first, second, and third trials. Dotted lines are used for reference.

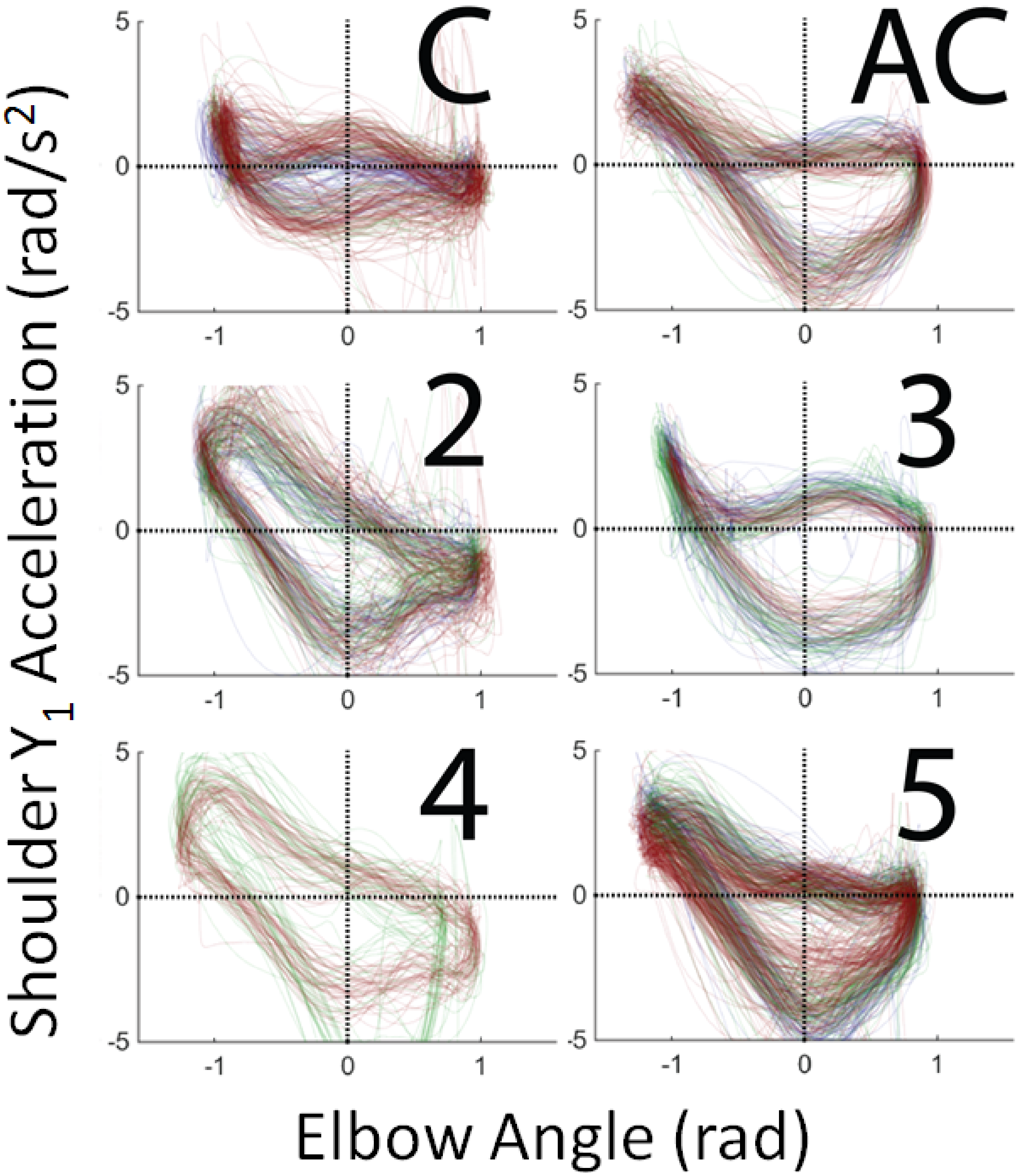

Figure 8.7: Phase portraits of angular acceleration (rad/s^2) against elbow angle (rad) for GH elevation/depression (Y_1) in a representative subject. All three trials are shown, with red, green, and blue representing first, second, and third trials. Dotted lines are used for reference.

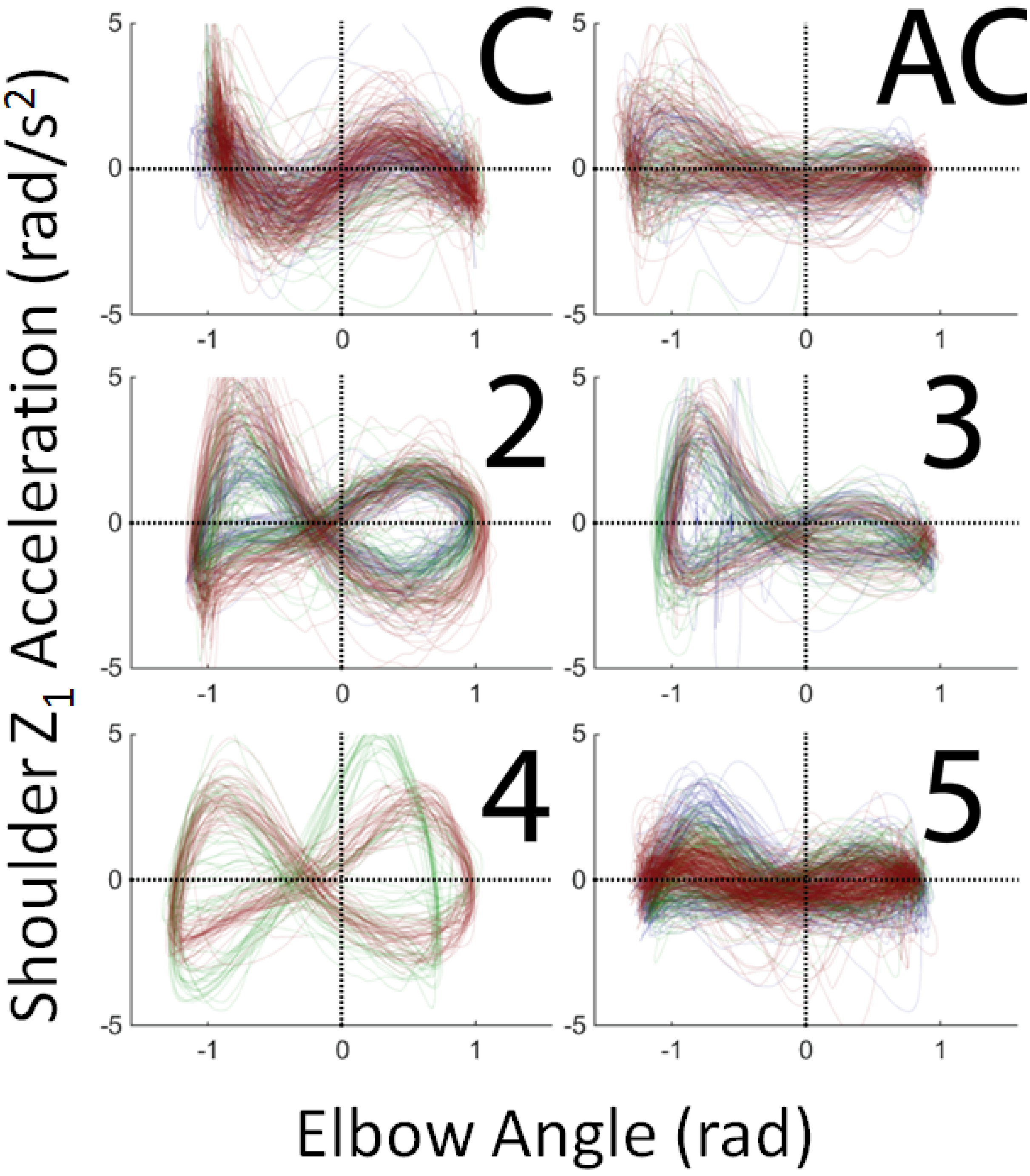

Figure 8.8: Phase portraits of angular acceleration (rad/s^2) against elbow angle (rad) for GH plane rotation (Z_1) in a representative subject. All three trials are shown, with red, green, and blue representing first, second, and third trials. Dotted lines are used for reference.

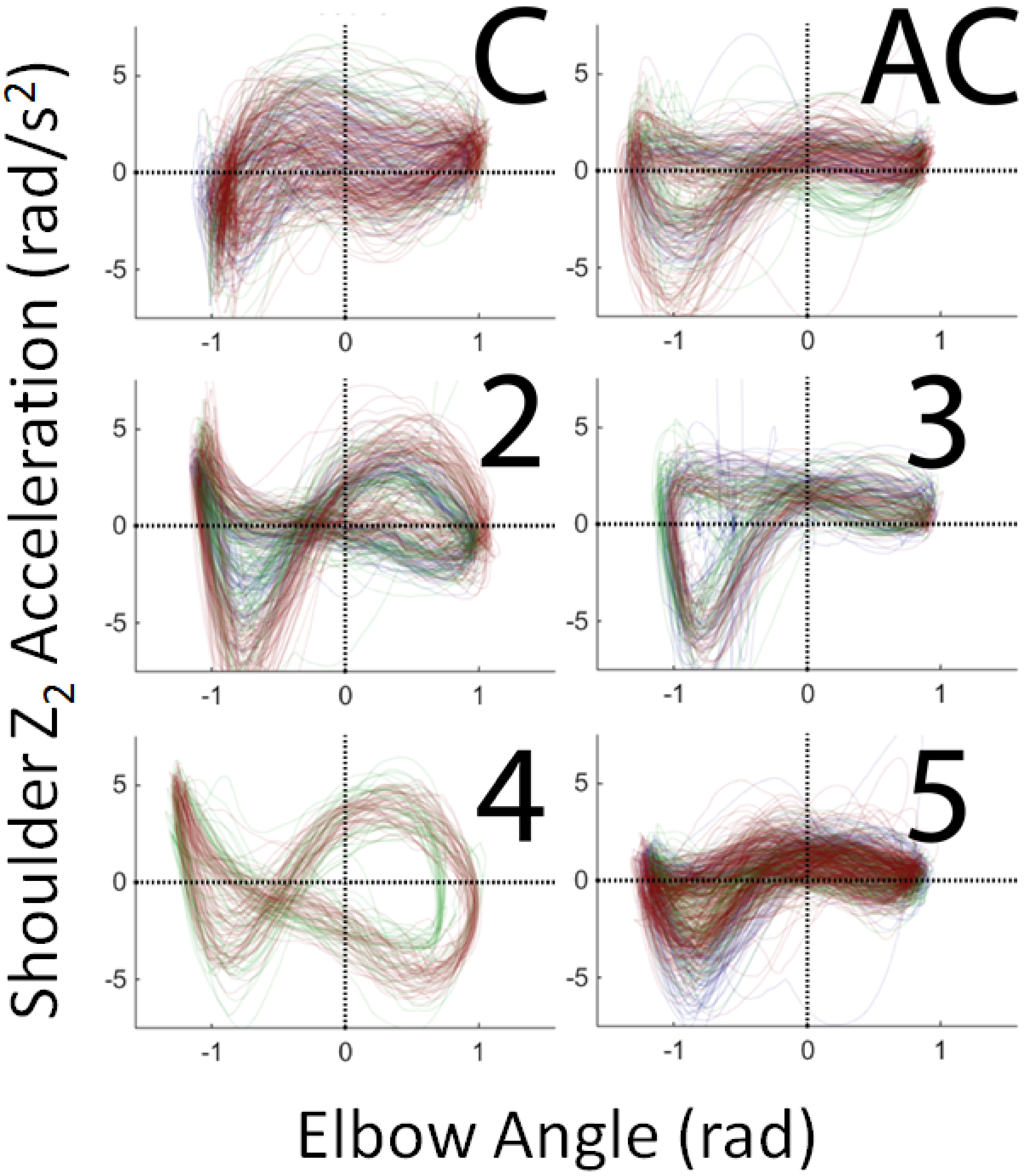

Figure 8.9: Phase portraits of angular acceleration (rad/s^2) against elbow angle (rad) for GH axial rotation (Z_2) in a representative subject. All three trials are shown, with red, green, and blue representing first, second, and third trials. Dotted lines are used for reference.

A mean increase in the normalised rep count of 82% was found in mode 5 compared to the AC mode. This suggests that mode 5 is able to provide significant augmentation to an individual's ability to perform hammer curls. The pressure differential in mode 5 appears to be acting as an assistive spring, compensating for the mass of the barbell, allowing the subject to perform significantly more repetitions. The converse of this can be seen in mode 2. Subjects were impeded by this mode, with a mean reduction in repetitions of 23%.

Modes 3, 4 were designed to examine the effect of a pure stiffness change instead of a stiffness and offset change (modes 2, 5). A subject's performance in these modes was found to be similar to when they did not wear the device for both the atmospheric and 50 psi settings. This could be due to assistance in the flexion phase being counteracted by difficulty during the extension mode.

The decrease in ability when wearing APEX (AC) when compared to the person not wearing the device (C) indicates the strong effect of the form and fit of the device. Though the device was designed to minimise any impediments to a user's range of motion, the attachment cuffs were found to limit an individual's ability to move. These reductions were compensated by the assistance provided in modes 3, 4, 5, but show the importance of fit and ergonomic design.

Figures 8.6 to 8.7 show the phase plots for these modes. By examining these plots, changes in compensatory actions can be seen.

In the elbow plots, a diagonal line is used to separate the flexion and extension movements, with flexion below and extension above the line. From these plots, hyper-extension can be seen in modes **AC**, **3**, and **4** compared to the control **C**. This could be due to the individual having to compensate for the resistances in the device due to friction and the effect of the pneumatic cylinder. Mode **5** appears to have a symmetric appearance between the flexion and extension motions. This suggests that the motions are more even in Mode **5**, even when compared to the control mode **C**.

The X_{Gh} shoulder rotations highlight the differences in compensation strategy between the different action. In control case **C**, there is negligible movement in the X_{Gh} direction suggesting that the action is not being compensated by the muscles acting about the X_{Gh} axis. This is contrasted with modes **AC**, **3**, and **5** which appear to show compensation in the $\theta >= 0$ part of the curl action. Modes **2** and **4** show significant X_{Gh} compensation for the full curl action. This suggests that both the flexion and extension actions are challenging in these two modes.

The shoulder Y_{Gh} and YY_{Gh} actions show compensations subjects could perform to move out of the plane to use alternative muscle groups. From these plots, modes **C**, **AC**, and **5** all appear to have minimal compensatory rotations.

8.4 Conclusion

These initial trials show the potential in the proposed APEX framework for actuation and control. An 82% increase in barbell curls can be provided across all subjects, for a single change of the system pressures. Observing the phase trajectories of the shoulder complex, the assistance provided appears to be natural, reducing the need for compensatory actions.

It was found that ergonomic fit was a substantial factor in the experimental procedure, significantly reducing an individual's abilities to perform hammer curls. While the assistance provided was able to overcome these restrictions, improving the fit of the device is expected to improve comfort and effectiveness.

Despite the reduction in performance due to ergonomic fit, the proposed APEX assistance framework was found to be capable of delivering substantial assistance to the wearer. This assistance is provided though a few grams of compressed gas foe each stiffness change. The success of these tests gives credibility to an active/passive framework for control.

Based on these experiments, a new prototype was developed (Figure 8.10). APEX-γ has improved ergonomics and offers assistance at the shoulder. This device is scheduled for healthy and clinical subject testing by the end of 2016.

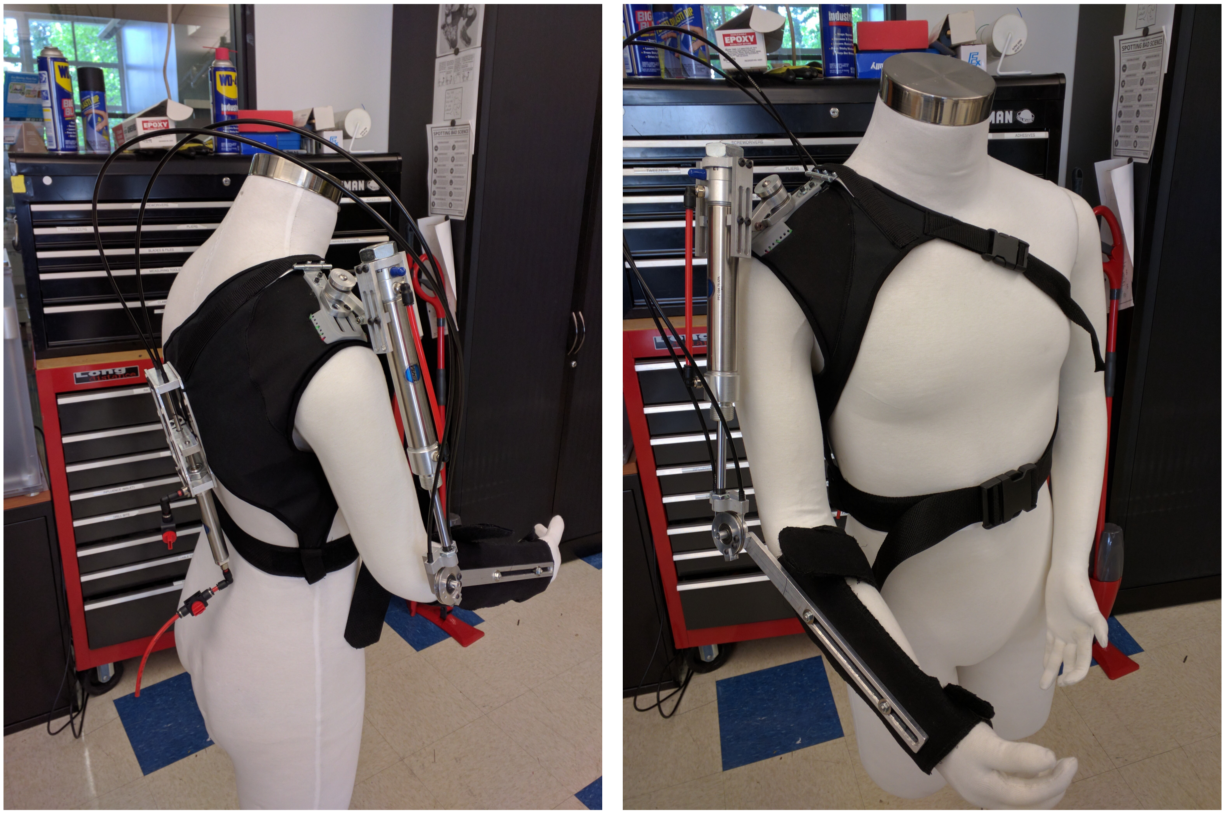

Figure 8.10: APEX-γ. Left: Side view showing the refined backplate, and shoulder harness. Right: Front view showing the elbow mechanism and arm brace.

Chapter 9

Future Work

This thesis has outlined a number of preliminary ideas in human modelling and assistive device design. While a number of initial results have been developed, there are a number of immediate tasks that need to be completed in the near future. These tasks have been organised in the same order as the thesis with the extension to a high-level multi state hybrid controller being proposed for the next APEX controller.

9.1 Modelling Framework

The presented modelling framework shows promise but is lacking in a number of key areas. There is a decrease in accuracy of the joint recovery process for small deflections (Section 6.3). As the arc of the motion about the ankle was small, it was difficult to recover the exact location of the joint. A standard method to artificially increase the arc travelled is to put the marker on a beam that is rigidly attached to the joint[136]. While this is likely to improve the accuracy of the ankle recovery without the requirement of ankle placement, it does require the addition of a specialist device which could prove problematic in clinical implementation. As an alternative, patients could be asked to sit with their ankles raised above the ground, then perform a plantar flexion/dorsiflexion about the ankle while extending their leg. This action would simultaneously locate the ankle and the knee, potentially improving the kinematic recovery process.

As noted in the robotic and human experiments, the estimation of the full kinematic state is hampered by only having observations of the motion capture markers (Sections 5.3.2 and 6.3.2). The addition of Inertial Measurement Units (IMUs) on the limb segments allows for a direct measurement of the body accelerations. These sensors can be added directly to the UKF, allowing for an improved estimate of the state derivatives. The effect of these additions have on the kinematic and dynamic recovery process needs to be evaluated.

The analysis presented in this thesis was simplified to a plane. While the kinematic and dynamic recovery methods presented are suitable for 3D recovery, their efficacy needs to be determined. This can be performed by studying the compound actions of the UR5 and human shoulder joints. Through the analysis of these systems, factors that may not arise in 2D systems can be found.

As this work concentrated on the feasibility of these methods for use in clinics, gold standard sensors were used in the analysis. The deployment of these sensors is unlikely due to the inherent cost and expertise. Therefore the application of these methods to affordable sensing modalities such as the Kinect and Wii Balance board needs to be performed.

9.2 Robotic Validation

A robotic system was used to evaluate the efficacy of the proposed modelling framework. As the joint states and representative model were known apriori, it was possible to directly compare the recovered model and states with a ground truth value.

The robotic validation explored in this thesis focused on the recovery from the motions about a single joint. This allowed for guidelines to be established on the recovery process. The extension to multiple joints, both moving in the plane as well as in full 3D will allow for a deeper understanding on the precision, accuracy and failure modes of this recovery process.

There was a mismatch between the robotic and human systems used in this thesis. While the sit-to-stand action has substantial size, mass and inertia at the distal link, this was not true of the UR5 manipulator, resulting in poor recovery of kinematic and dynamic parameters in the robotic experiments. The addition of an inertial body to the UR5 end effector would result in a better representation of the sit-to-stand case.

9.3 Human Modelling

While an individualised human model is recovered in this work, the validation to a ground truth value for that subject was not performed. The use of MRI, DEXA, and fluoroscopy to estimate the anatomical masses, inertias and joint locations would allow for a gold-standard of that subject's model.

The augmentation of other clinical tests needs to be determined. While the five-times sit-to-stand test was easy to investigate, the application of these methods to more elaborate tests such as the Fugl-Meyer would allow for richer modelling.

The sit-to-stand action was chosen due to the substantial mass and inertia at the distal link allowing for a tractable test of the modelling process. In the analysis of the limbs, the mass of the limbs decreases for each successively distal link. As seen in the UR5 experiments, this limits the precision and accuracy of the proposed model recovery method. The poor performance due to small motions may be reducible by placing markers on lightweight rigid rods, artificially increasing the arc of action. Poor performance due to insufficient mass at the extremity may be compensated through the addition of a second force sensor at the hand. As the contact forces at the proximal and distal ends are known, this may improve the signal-to-noise ratio seen in the UR5 experiments.

9.4 Prescriptive Robotics

The experimental validation of the prescriptive framework introduced in Chapter 7 was not performed due to the lack of stiffness control in the existing iteration of the APEX. Comparing the optimal assistive parameters found experimentally and using the prescriptive framework will allow for validation of these methods. This experimentation could be performed using physically distinct hardware (e.g. swapping springs), through impedance control, or through variable dynamic actuators. Each of these options have their own strengths and weaknesses, with the ease of implementation, granularity in the change in joint dynamics, and potential for feedback varying with each method.

To facilitate rapid testing of different controllers and devices, an active exoskeleton test-bed similar to the one used by Caputo and Collins[20] would allow for the emulation of different devices. By cable driving the exoskeleton from a bench, there is a physical separation between the worn device and the actuation system. This allows for rapid changes in control strategies without requiring the redevelopment of hardware which can take substantial time. The use of these test-bed systems allows for the effect of different control strategies to be explored without changing additional parameters.

9.5 APEX

Chapter 8 introduced the current iteration of the APEX and the feasibility of active/passive pneumatic assistance. While these experiments showed the potential in these methods, the low level control was extremely crude consisting of binary pressure control. The low-level control of the pressures in the system would allow for improved granularity in the potential dynamic responses.

Direct stiffness control needs to be performed. As the joint stiffness and equilibrium point will vary with the pressures on the flexion and extension sides of the cylinder, it should be possible to create a low-level stiffness controller. This allows for direct implementation of the spring characteristics found from the prescriptive framework.

Variation of the dynamics at a joint could be attained though the use of magneto-rheostatic materials or through a throttled hydraulic system. The viscosity of a fluidic cylinder can be modulated by throttling either a varying magnetic field or the aperture size. This variation can be used to *bleed* the energy in a system, reducing the effect of sudden shock loads, or fully locking the limb allowing for passive holding.

An interesting control problem is the addition of an active element to a variable dynamic actuator. Active power assistance can be delivered by connecting a conventional electric actuator to the backplate pulley shown in Figure 8.2. The system can therefore be balanced between the bulk assistance being provided by the active/passive system, while the active motor provides precision assistance. As the majority of the assistance is afforded by the active/passive system the specifications on the active motor are far lower than for an actively driven system. The active motor can also deliver faster feedback, potentially compensating for tremor.

9.6 High-level APEX control

It is possible to separate a known set of tasks into groups based on the sub-sections of the individual's workspace. These sub-workspaces can be joined to form a connected graph, with each node representing a particular sub-workspace, and edges representing overlapping connected areas between two sub-workspace. Commonly coupled actions (such as self feeding and drinking) can be grouped together to reduce the number of changes between sub-workspaces during the activities being analysed.

A user's ability to move within each sub-workspace can be assessed though either experiment or though the proposed modelling framework. When a user is found to be unable to move fully within the sub-workspace, the minimal assistance required to restore function can be found. This assigns a set of passive dynamic parameters for each node on the graph.

When a user moves their arms, their actions will lie within a node on the graph. If the state of a user is found to lie near the boundary between two sub-workspaces, the dynamic parameters can be adjusted at this boundary allowing the user to perform the next task. In this manner a hybrid controller can be constructed, allowing for the analysis of stability of switching between sub-workspaces.

ALL THAT STUFF I SAID WAS A LIE GROUP

Figure 9.1: Summary of results in this thesis[133].

Bibliography

[1] AMTI. *OPT464508-1000*. Retrieved 2016/Feb/29. URL: `http://www.amti.biz/`.

[2] Alessandro Abate et al. "An approximate dynamic programming approach to probabilistic reachability for stochastic hybrid systems". In: *Decision and Control, 2008. CDC 2008. 47th IEEE Conference on*. IEEE. 2008, pp. 4018–4023.

[3] R Aissaoui and J Dansereau. "Biomechanical analysis and modelling of sit to stand task: a literature review". In: *Systems, Man, and Cybernetics, 1999. IEEE SMC'99 Conference Proceedings. 1999 IEEE International Conference on*. Vol. 1. IEEE. 1999, pp. 141–146.

[4] Åsa Andersson et al. "How to identify potential fallers in a stroke unit: validity indexes of 4 test methods". In: *Journal of rehabilitation medicine* 38.3 (2006), pp. 186–191.

[5] Ko Ayusawa, Yoshihiko Nakamura, and Gentiane Venture. "Optimal estimation of human body segments dynamics using realtime visual feedback". In: *Intelligent Robots and Systems, 2009. IROS 2009. IEEE/RSJ International Conference on*. IEEE. 2009, pp. 1627–1632.

[6] Ko Ayusawa, Gentiane Venture, and Yoshihiko Nakamura. "Identifiability and identification of inertial parameters using the underactuated base-link dynamics for legged multibody systems". In: *The International Journal of Robotics Research* 33.3 (2014), pp. 446–468.

[7] Ko Ayusawa, Gentiane Venture, and Yoshihiko Nakamura. "Identification of humanoid robots dynamics using floating-base motion dynamics". In: *2008 IEEE/RSJ International Conference on Intelligent Robots and Systems*. IEEE. 2008, pp. 2854–2859.

[8] Ko Ayusawa, Gentiane Venture, and Yoshihiko Nakamura. "Real-time implementation of physically consistent identification of human body segments". In: *Robotics and Automation (ICRA), 2011 IEEE International Conference on*. IEEE. 2011, pp. 6282–6287.

[9] Fariba Bahrami et al. "Biomechanical analysis of sit-to-stand transfer in healthy and paraplegic subjects". In: *Clinical Biomechanics* 15.2 (2000), pp. 123–133.

[10] Alexander L Bell, Douglas R Pedersen, and Richard A Brand. "A comparison of the accuracy of several hip center location prediction methods". In: *Journal of biomechanics* 23.6 (1990), pp. 617–621.

[11] Bledsoe. *Extender Arm.* URL: `bledsoebrace.com`.

[12] Lisa Blum and Nicol Korner-Bitensky. "Usefulness of the Berg Balance Scale in stroke rehabilitation: a systematic review". In: *Physical therapy* 88.5 (2008), pp. 559–566.

[13] Vincent Bonnet and Gentiane Venture. "Fast Determination of the Planar Body Segment Inertial Parameters Using Affordable Sensors". In: *IEEE Transactions on Neural Systems and Rehabilitation Engineering* 23.4 (2015), pp. 628–635.

[14] Alphons MPM Bovens et al. "Variability and reliability of joint measurements". In: *The American Journal of Sports Medicine* 18.1 (1990), pp. 58–63.

[15] Bambi R Brewer, Sharon K McDowell, and Lise C Worthen-Chaudhari. "Poststroke upper extremity rehabilitation: a review of robotic systems and clinical results". In: *Topics in stroke rehabilitation* (2014).

[16] Carmen MN Brigante et al. "Towards miniaturization of a MEMS-based wearable motion capture system". In: *IEEE Transactions on Industrial Electronics* 58.8 (2011), pp. 3234–3241.

[17] Roger W Brockett. "Robotic manipulators and the product of exponentials formula". In: *Mathematical theory of networks and systems*. Springer. 1984, pp. 120–129.

[18] Michael H Brooke et al. "Clinical trial in Duchenne dystrophy. I. The design of the protocol". In: *Muscle & nerve* 4.3 (1981), pp. 186–197.

[19] Aurelio Cappozzo. "Gait analysis methodology". In: *Human Movement Science* 3.1 (1984), pp. 27–50.

[20] Joshua M Caputo and Steven H Collins. "An experimental robotic testbed for accelerated development of ankle prostheses". In: *Robotics and automation (ICRA), 2013 IEEE international conference on*. IEEE. 2013, pp. 2645–2650.

[21] Centers for Disease Control and Prevention. *Important Facts about Falls.* Retrieved 2017/July/28. 2016. URL: `www.cdc.gov`.

[22] Don B Chaffin, Gunnar Andersson, Bernard J Martin, et al. *Occupational biomechanics*. Wiley New York, 1999.

[23] Hui-Mei Chen et al. "Test-retest reproducibility and smallest real difference of 5 hand function tests in patients with stroke". In: *Neurorehabilitation and neural repair* (2009).

[24] Ross A Clark et al. "Validity and reliability of the Nintendo Wii Balance Board for assessment of standing balance". In: *Gait & posture* 31.3 (2010), pp. 307–310.

[25] Ross A Clark et al. "Validity of the Microsoft Kinect for assessment of postural control". In: *Gait & posture* 36.3 (2012), pp. 372–377.

[26] Roy B Davis et al. "A gait analysis data collection and reduction technique". In: *Human movement science* 10.5 (1991), pp. 575–587.

[27] Paolo De Leva. “Adjustments to Zatsiorsky-Seluyanov’s segment inertia parameters”. In: *Journal of biomechanics* 29.9 (1996), pp. 1223–1230.

[28] P Delogne. “Computer optimization of Deschamps’ method and error cancellation in reflectometry”. In: *Proc. IMEKO-Symp. Microwave Measurements*. 1972, pp. 117–123.

[29] Wilfred Taylor Dempster, Lawrence A Sherr, and Judith G Priest. “Conversion scales for estimating humeral and femoral lengths and the lengths of functional segments in the limbs of American Caucasoid males”. In: *Human Biology* 36.3 (1964), pp. 246–262.

[30] Douglas A Dennis et al. “Range of motion after total knee arthroplasty The effect of implant design and weight-bearing conditions”. In: *The Journal of arthroplasty* 13.7 (1998), pp. 748–752.

[31] Jennifer L Durkin and James J Dowling. “Analysis of body segment parameter differences between four human populations and the estimation errors of four popular mathematical models”. In: *Journal of biomechanical engineering* 125.4 (2003), pp. 515–522.

[32] Herbert Edelsbrunner and Ernst P Mücke. “Three-dimensional alpha shapes”. In: *ACM Transactions on Graphics (TOG)* 13.1 (1994), pp. 43–72.

[33] Rainald M Ehrig et al. “A survey of formal methods for determining the centre of rotation of ball joints”. In: *Journal of biomechanics* 39.15 (2006), pp. 2798–2809.

[34] Jeremy L Emken, Raul Benitez, and David J Reinkensmeyer. “Human-robot cooperative movement training: learning a novel sensory motor transformation during walking with robotic assistance-as-needed”. In: *Journal of NeuroEngineering and Rehabilitation* 4.1 (2007), p. 1.

[35] Bruce Etnyre and David Q Thomas. “Event standardization of sit-to-stand movements”. In: *Physical therapy* 87.12 (2007), pp. 1651–1666.

[36] Roy Featherstone. *Rigid body dynamics algorithms*. Springer, 2014.

[37] Peter Andreas Federolf. “A novel approach to solve the "missing marker problem" in marker-based motion analysis that exploits the segment coordination patterns in multi-limb motion data”. In: *PloS one* 8.10 (2013), e78689.

[38] C Frigo and M Rabuffetti. “Multifactorial estimation of hip and knee joint centres for clinical application of gait analysis”. In: *Gait & posture* 8.2 (1998), pp. 91–102.

[39] Axel R Fugl-Meyer et al. “The post-stroke hemiplegic patient. 1. a method for evaluation of physical performance.” In: *Scandinavian journal of rehabilitation medicine* 7.1 (1974), pp. 13–31.

[40] Masahiro Fujimoto and Li-Shan Chou. “Dynamic balance control during sit-to-stand movement: an examination with the center of mass acceleration”. In: *Journal of biomechanics* 45.3 (2012), pp. 543–548.

[41] Sahan S Hiniduma Udugama Gamage and Joan Lasenby. “New least squares solutions for estimating the average centre of rotation and the axis of rotation”. In: *Journal of biomechanics* 35.1 (2002), pp. 87–93.

[42] Walter Gander, Gene H Golub, and Rolf Strebel. “Least-squares fitting of circles and ellipses”. In: *BIT Numerical Mathematics* 34.4 (1994), pp. 558–578.

[43] David J Gladstone, Cynthia J Danells, and Sandra E Black. “The Fugl-Meyer assessment of motor recovery after stroke: a critical review of its measurement properties”. In: *Neurorehabilitation and neural repair* 16.3 (2002), pp. 232–240.

[44] Alejandro González et al. “Whole body center of mass estimation with portable sensors: Using the statically equivalent serial chain and a kinect”. In: *Sensors* 14.9 (2014), pp. 16955–16971.

[45] J Goodwin et al. “Clinical methods of goniometry: a comparative study”. In: *Disability and rehabilitation* 14.1 (1992), pp. 10–15.

[46] Ted Greenwald. *Ekso’s Exoskeletons Let Paraplegics Walk, Will Anyone Actually Wear One?* Online. Retrieved 2016/July/25. Mar. 2012. URL: `fastcompany.com//1822791`.

[47] Qi Guo, Wilfrid Perruquetti, and Maxime Gautier. “On-line robot dynamic identification based on power model, modulating functions and causal Jacobi estimator”. In: *2014 IEEE/ASME International Conference on Advanced Intelligent Mechatronics*. IEEE. 2014, pp. 494–499.

[48] K Halvorsen, M Lesser, and A Lundberg. “A new method for estimating the axis of rotation and the center of rotation”. In: *Journal of biomechanics* 32.11 (1999), pp. 1221–1227.

[49] Jay J Han et al. “Reachable workspace in facioscapulohumeral muscular dystrophy (FSHD) by Kinect”. In: *Muscle & nerve* 51.2 (2015), pp. 168–175.

[50] Kimberley Hayes et al. “Reliability of five methods for assessing shoulder range of motion”. In: *Australian Journal of Physiotherapy* 47.4 (2001), pp. 289–294.

[51] Neville Hogan. “Impedance control: An approach to manipulation: Part II—Implementation”. In: *Journal of dynamic systems, measurement, and control* 107.1 (1985), pp. 8–16.

[52] Neville Hogan. “Impedance control: An approach to manipulation”. In: *American Control Conference, 1984*. IEEE. 1984, pp. 304–313.

[53] ST Holzreiter. “Calculation of the instantaneous centre of rotation for a rigid body.” In: *Journal of biomechanics* 24.7 (1990), pp. 643–647.

[54] Junhui Hou et al. “Restoring corrupted motion capture data via jointly low-rank matrix completion”. In: *2014 IEEE International Conference on Multimedia and Expo (ICME)*. IEEE. 2014, pp. 1–6.

[55] MA Hughes et al. “Chair rise strategies in the elderly”. In: *Clinical Biomechanics* 9.3 (1994), pp. 187–192.

[56] Biodigital Human. *Skeletal Model.* June 2014. URL: `www.biodigital.com`.

[57] Alexandre Janot et al. "Comparison between the CLOE Method and the DIDIM Method for Robots Identification". In: *IEEE Transactions on Control Systems Technology* 22.5 (2014), pp. 1935–1941.

[58] Nathanaël Jarrassé et al. "Robotic exoskeletons: a perspective for the rehabilitation of arm coordination in stroke patients". In: *Frontiers in human neuroscience* 8 (2014), p. 947.

[59] Jovana Jovic et al. "Humanoid and Human Inertia Parameter Identification Using Hierarchical Optimization". In: *IEEE Transactions on Robotics* 32.3 (2016), pp. 726–735.

[60] Anthony Jubien, Maxime Gautier, and Alexandre Janot. "Dynamic identification of the Kuka LightWeight robot: Comparison between actual and confidential Kuka's parameters". In: *2014 IEEE/ASME International Conference on Advanced Intelligent Mechatronics.* IEEE. 2014, pp. 483–488.

[61] Anthony Jubien, Maxime Gautier, and Alexandre Janot. "Effectiveness of the DIDIM method with respect to the usual CLOE method. Application to the dynamic parameters identification of an industrial robot". In: *Control Conference (ASCC), 2013 9th Asian.* IEEE. 2013, pp. 1–6.

[62] Simon J Julier and Jeffrey K Uhlmann. "New extension of the Kalman filter to nonlinear systems". In: *AeroSense'97.* International Society for Optics and Photonics. 1997, pp. 182–193.

[63] Mrn P Kadaba, HK Ramakrishnan, and ME Wootten. "Measurement of lower extremity kinematics during level walking". In: *Journal of orthopaedic research* 8.3 (1990), pp. 383–392.

[64] Waleed Khalil et al. "OpenSyMoRo: An open-source software package for Symbolic Modelling of Robots". In: *Advanced Intelligent Mechatronics (AIM), 2014 IEEE/ASME International Conference on.* IEEE. 2014, pp. 1206–1211.

[65] Wisama Khalil and Etienne Dombre. *Modeling, identification and control of robots.* Butterworth-Heinemann, 2004.

[66] Renata Noce Kirkwood, Elsie G Culham, and Patrick Costigan. "Radiographic and non-invasive determination of the hip joint center location: effect on hip joint moments". In: *Clinical Biomechanics* 14.4 (1999), pp. 227–235.

[67] Katharina Kufieta and Jan Tommy Gravdahl. "Force Estimation in Robotic Manipulators: Modeling, Simulation and Experiments". MA thesis. Norwegian University of Science and Technology, 2014.

[68] Gregorij Kurillo et al. "Development and application of stereo camera-based upper extremity workspace evaluation in patients with neuromuscular diseases". In: *PloS one* 7.9 (2012), e45341.

[69] Gregorij Kurillo et al. "Evaluation of upper extremity reachable workspace using Kinect camera". In: *Technology and Health Care* 21.6 (2013), pp. 641–656.

[70] Gert Kwakkel, Boudewijn J Kollen, and Hermano I Krebs. "Effects of robot-assisted therapy on upper limb recovery after stroke: a systematic review". In: *Neurorehabilitation and neural repair* (2007).

[71] Peter Langhorne, Fiona Coupar, and Alex Pollock. "Motor recovery after stroke: a systematic review". In: *The Lancet Neurology* 8.8 (2009), pp. 741–754.

[72] Alberto Leardini et al. "Human movement analysis using stereophotogrammetry: Part 3. Soft tissue artifact assessment and compensation". In: *Gait & posture* 21.2 (2005), pp. 212–225.

[73] Alberto Leardini et al. "Validation of a functional method for the estimation of hip joint centre location". In: *Journal of biomechanics* 32.1 (1999), pp. 99–103.

[74] Johan Lofberg. "YALMIP: A toolbox for modeling and optimization in MATLAB". In: *Computer Aided Control Systems Design, 2004 IEEE International Symposium on*. IEEE. 2004, pp. 284–289.

[75] T-W Lu and JJ O'connor. "Bone position estimation from skin marker co-ordinates using global optimisation with joint constraints". In: *Journal of biomechanics* 32.2 (1999), pp. 129–134.

[76] Jonas Lundgren. *Alpha Shapes*. Retrieved 2016/July/21. Sept. 2010. URL: `www.mathworks.com/matlabcentral/fileexchange/28851-alpha-shapes`.

[77] Sebastian OH Madgwick, Andrew JL Harrison, and Ravi Vaidyanathan. "Estimation of IMU and MARG orientation using a gradient descent algorithm". In: *2011 IEEE International Conference on Rehabilitation Robotics*. IEEE. 2011, pp. 1–7.

[78] Daichi Maita and Gentiane Venture. "Influence of the model's degree of freedom on human body dynamics identification". In: *2013 35th Annual International Conference of the IEEE Engineering in Medicine and Biology Society (EMBC)*. IEEE. 2013, pp. 4609–4612.

[79] Laura Marchal-Crespo and David J Reinkensmeyer. "Review of control strategies for robotic movement training after neurologic injury". In: *Journal of neuroengineering and rehabilitation* 6.1 (2009), p. 1.

[80] Donald W Marquardt. "An algorithm for least-squares estimation of nonlinear parameters". In: *Journal of the society for Industrial and Applied Mathematics* 11.2 (1963), pp. 431–441.

[81] Vicente Mata et al. "Dynamic parameter identification in industrial robots considering physical feasibility". In: *Advanced Robotics* 19.1 (2005), pp. 101–119.

[82] Robert Peter Matthew et al. "Calculating reachable workspace volume for use in quantitative medicine". In: *Computer Vision-ECCV 2014 Workshops*. Springer International Publishing, 2014, pp. 570–583.

[83] Robert Peter Matthew et al. “Initial investigation into the effect of an Active/Passive exoskeleton on hammer curl performance in healthy subjects”. In: *2015 37th Annual International Conference of the IEEE Engineering in Medicine and Biology Society (EMBC)*. IEEE. 2015, pp. 3607–3610.

[84] Robert Peter Matthew et al. “Introduction and initial exploration of an Active/Passive Exoskeleton framework for portable assistance”. In: *Intelligent Robots and Systems (IROS), 2015 IEEE/RSJ International Conference on*. IEEE. 2015, pp. 5351–5356.

[85] Robert Peter Matthew et al. “Optimal design for individualised passive assistance”. In: *Proceedings of the 6th Augmented Human International Conference*. ACM. 2015, pp. 69–76.

[86] Brona C McDowell et al. “The variability of goniometric measurements in ambulatory children with spastic cerebral palsy”. In: *Gait & posture* 12.2 (2000), pp. 114–121.

[87] Meinburg. *Meingburg NTP*. Retrieved 2016/July/19. URL: `www.meinbergglobal.com`.

[88] Felix Messmer. *ur5.urdf.xacro*. Retrieved 2016/Feb/29. Fraunhofer IPA. URL: `https://github.com/ros-industrial/universal\_robot`.

[89] Nathan Miller et al. “Motion capture from inertial sensing for untethered humanoid teleoperation”. In: *Humanoid Robots, 2004 4th IEEE/RAS International Conference on*. Vol. 2. IEEE. 2004, pp. 547–565.

[90] Ian M Mitchell. “The flexible, extensible and efficient toolbox of level set methods”. In: *Journal of Scientific Computing* 35.2-3 (2008), pp. 300–329.

[91] Ian M Mitchell, Alexandre M Bayen, and Claire J Tomlin. “A time-dependent Hamilton-Jacobi formulation of reachable sets for continuous dynamic games”. In: *IEEE Transactions on automatic control* 50.7 (2005), pp. 947–957.

[92] Ian M Mitchell and Claire J Tomlin. “Overapproximating reachable sets by Hamilton-Jacobi projections”. In: *journal of Scientific Computing* 19.1-3 (2003), pp. 323–346.

[93] Thomas B Moeslund, Adrian Hilton, and Volker Krüger. “A survey of advances in vision-based human motion capture and analysis”. In: *Computer vision and image understanding* 104.2 (2006), pp. 90–126.

[94] Richard M Murray, Zexiang Li, and S Shankar Sastry. *A mathematical introduction to robotic manipulation*. CRC press, 1994.

[95] Spencer Murray and Michael Goldfarb. “Towards the use of a lower limb exoskeleton for locomotion assistance in individuals with neuromuscular locomotor deficits”. In: *2012 Annual International Conference of the IEEE Engineering in Medicine and Biology Society*. IEEE. 2012, pp. 1912–1915.

[96] RR Neptune and ML Hull. “Accuracy assessment of methods for determining hip movement in seated cycling”. In: *Journal of biomechanics* 28.4 (1995), pp. 423–437.

[97] Newsome and Melton. *Spinal Cord Injury Statistics.* Retrieved 2016/July/27. URL: `www.brainandspinalcord.org`.

[98] Yves Nievergelt. "Perturbation analysis for circles, spheres, and generalized hyperspheres fitted to data by geometric total least-squares". In: *Mathematics of computation* 73.245 (2004), pp. 169–180.

[99] Optitrack. *Optitrack Motion Capture.* Retrieved: 2016/Jul/07. URL: `https://www.optitrack.com/`.

[100] Yi-Chung Pai and James Patton. "Center of mass velocity-position predictions for balance control". In: *Journal of biomechanics* 30.4 (1997), pp. 347–354.

[101] Elisabetta Papa and Aurelio Cappozzo. "A telescopic inverted-pendulum model of the musculo-skeletal system and its use for the analysis of the sit-to-stand motor task". In: *Journal of Biomechanics* 32.11 (1999), pp. 1205–1212.

[102] Frank C. Park, James E Bobrow, and Scott R Ploen. "A Lie group formulation of robot dynamics". In: *The International Journal of Robotics Research* 14.6 (1995), pp. 609–618.

[103] JC Pezzack, RW Norman, and DA Winter. "An assessment of derivative determining techniques used for motion analysis". In: *Journal of biomechanics* 10.5-6 (1977), pp. 377–382.

[104] Phasespace. *Impulse X2.* Retrieved 2016/Feb/29. URL: `http://www.phasespace.com/impulse-motion-capture.html`.

[105] Stephen J Piazza, Noriaki Okita, and Peter R Cavanagh. "Accuracy of the functional method of hip joint center location: effects of limited motion and varied implementation". In: *Journal of biomechanics* 34.7 (2001), pp. 967–973.

[106] Morgan Quigley et al. "ROS: an open-source Robot Operating System". In: *ICRA Workshop on Open Source Software.* 2009.

[107] Tariq Rahman et al. "Passive exoskeletons for assisting limb movement". In: *Journal of rehabilitation research and development* 43.5 (2006), p. 583.

[108] Jeffrey A Reinbolt et al. "Are patient-specific joint and inertial parameters necessary for accurate inverse dynamics analyses of gait?" In: *IEEE Transactions on Biomedical Engineering* 54.5 (2007), pp. 782–793.

[109] Emmanuel Roux et al. "Evaluation of the global optimisation method within the upper limb kinematics analysis". In: *Journal of biomechanics* 35.9 (2002), pp. 1279–1283.

[110] Yoshiyuki Sankai. *HAL: Hybrid Assistive Limb Based on Cybernics.* Retrieved 2017/July/25. Feb. 2011. URL: `sanlab.kz.tsukuba.ac.jp//sonota//ISSR_Sankai.pdf`.

[111] Michael H Schwartz and Adam Rozumalski. "A new method for estimating joint parameters from motion data". In: *Journal of biomechanics* 38.1 (2005), pp. 107–116.

[112] Jon M Selig. *Geometric fundamentals of robotics*. Springer Science & Business Media, 2004.

[113] Anne Shumway-Cook, Sandy Brauer, and Marjorie Woollacott. "Predicting the probability for falls in community-dwelling older adults using the Timed Up & Go Test". In: *Physical therapy* 80.9 (2000), pp. 896–903.

[114] Marius-CĂlin Silaghi et al. "Local and global skeleton fitting techniques for optical motion capture". In: *Modelling and Motion Capture Techniques for Virtual Environments*. Springer, 1998, pp. 26–40.

[115] Jonathan Sinclair, Paul John Taylor, and Sarah Jane Hobbs. "Digital filtering of three-dimensional lower extremity kinematics: An assessment". In: *Journal of human kinetics* 39.1 (2013), pp. 25–36.

[116] Robert A Siston and Scott L Delp. "Evaluation of a new algorithm to determine the hip joint center". In: *Journal of biomechanics* 39.1 (2006), pp. 125–130.

[117] Cristóvão D Sousa and Rui Cortesão. "Physical feasibility of robot base inertial parameter identification: A linear matrix inequality approach". In: *The International Journal of Robotics Research* 33.6 (2014), pp. 931–944.

[118] Adario Strange. *FDA Approves First Robotic Exoskeleton for Paralyzed Users*. Retrieved 2016/July/25. June 2014. URL: `mashable.com/2014/06/30/fda-approves-robotic-exoskeleton-paralyzed-rewalk`.

[119] Stroke.org. *Stroke Facts*. Retrieved 2016/July/27. URL: `www.stroke.org`.

[120] Guanhong Tao et al. "Biomechanical model-based multi-sensor motion estimation". In: *Sensors Applications Symposium (SAS), 2013 IEEE*. IEEE. 2013, pp. 156–161.

[121] Tammy O Tengs, Michelle Yu, and Elvina Luistro. "Health-related quality of life after stroke a comprehensive review". In: *Stroke* 32.4 (2001), pp. 964–972.

[122] Linda D Bogle Thorbahn and Roberta A Newton. "Use of the Berg Balance Test to predict falls in elderly persons". In: *Physical therapy* 76.6 (1996), pp. 576–583.

[123] Thomas Timm. *ur_modern_driver*. Retrieved 2016/Feb/29. URL: `https://github.com/ThomasTimm/ur\_modern\_driver`.

[124] Claire Tomlin, George J Pappas, and Shankar Sastry. "Conflict resolution for air traffic management: A study in multiagent hybrid systems". In: *IEEE Transactions on automatic control* 43.4 (1998), pp. 509–521.

[125] Universal Robots. *UR5*. Retrieved 2016/Feb/29. URL: `http://www.universal-robots.com/`.

[126] Christopher L Vaughan, Brian L Davis, CO Jeremy, et al. "Dynamics of human gait". In: (1999).

[127] Gentiane Venture, Ko Ayusawa, and Yoshihiko Nakamura. “Motion capture based identification of the human body inertial parameters”. In: *Engineering in Medicine and Biology Society, 2008. EMBS 2008. 30th Annual International Conference of the IEEE*. IEEE. 2008, pp. 4575–4578.

[128] Gentiane Venture, Ko Ayusawa, and Yoshihiko Nakamura. “Real-time identification and visualization of human segment parameters”. In: *2009 Annual International Conference of the IEEE Engineering in Medicine and Biology Society*. IEEE. 2009, pp. 3983–3986.

[129] Henri A Vrooman et al. “Fast and accurate automated measurements in digitized stereophotogrammetric radiographs”. In: *Journal of Biomechanics* 31.5 (1998), pp. 491–498.

[130] Todd H Wagner et al. “An economic analysis of robot-assisted therapy for long-term upper-limb impairment after stroke”. In: *Stroke* 42.9 (2011), pp. 2630–2632.

[131] Eric A Wan and Ronell Van Der Merwe. “The unscented Kalman filter for nonlinear estimation”. In: *Adaptive Systems for Signal Processing, Communications, and Control Symposium 2000. AS-SPCC. The IEEE 2000*. Ieee. 2000, pp. 153–158.

[132] Qifei Wang et al. “Evaluation of pose tracking accuracy in the first and second generations of microsoft kinect”. In: *Healthcare Informatics (ICHI), 2015 International Conference on*. IEEE. 2015, pp. 380–389.

[133] Zach Weinersmith. *Saturday Morning Breakfast Cereal*. Online. Used with permission. URL: `www.smbc-comics.com`.

[134] Susan L Whitney et al. “Clinical measurement of sit-to-stand performance in people with balance disorders: validity of data for the Five-Times-Sit-to-Stand Test”. In: *Physical therapy* 85.10 (2005), pp. 1034–1045.

[135] Ellen M Whyte and Benoit H Mulsant. “Post stroke depression: epidemiology, pathophysiology, and biological treatment”. In: *Biological psychiatry* 52.3 (2002), pp. 253–264.

[136] David A Winter. *Biomechanics and motor control of human movement*. John Wiley & Sons, 2009.

[137] Steven L Wolf et al. “Assessing Wolf motor function test as outcome measure for research in patients after stroke”. In: *Stroke* 32.7 (2001), pp. 1635–1639.

[138] HJ Woltring et al. “Finite centroid and helical axis estimation from noisy landmark measurements in the study of human joint kinematics”. In: *Journal of biomechanics* 18.5 (1985), pp. 379–389.

[139] Ge Wu et al. “ISB recommendation on definitions of joint coordinate system of various joints for the reporting of human joint motion—part I: ankle, hip, and spine”. In: *Journal of biomechanics* 35.4 (2002), pp. 543–548.

[140] Ge Wu et al. “ISB recommendation on definitions of joint coordinate systems of various joints for the reporting of human joint motion—Part II: shoulder, elbow, wrist and hand”. In: *Journal of biomechanics* 38.5 (2005), pp. 981–992.

[141] Qiong Wu and Pierre Boulanger. “Real-time estimation of missing markers for reconstruction of human motion”. In: *Virtual Reality (SVR), 2011 XIII Symposium on.* IEEE. 2011, pp. 161–168.

[142] Shane Xie. *Advanced Robotics for Medical Rehabilitation.* Springer, 2016.

[143] LF Yeung et al. “Evaluation of the Microsoft Kinect as a clinical assessment tool of body sway”. In: *Gait & posture* 40.4 (2014), pp. 532–538.

[144] Koji Yoshida and Wisama Khalil. “Verification of the positive definiteness of the inertial matrix of manipulators using base inertial parameters”. In: *The International Journal of Robotics Research* 19.5 (2000), pp. 498–510.

[145] William Young et al. “Assessing and training standing balance in older adults: a novel approach using the ‘Nintendo Wii’Balance Board”. In: *Gait & posture* 33.2 (2011), pp. 303–305.

[146] Huiyu Zhou and Huosheng Hu. “Human motion tracking for rehabilitation—A survey”. In: *Biomedical Signal Processing and Control* 3.1 (2008), pp. 1–18.

[147] eZono. *eZono 4000.* Retrieved 2016/March/27. URL: `www.ezono.com`.